Ion Transport and Structure of Layer-by-Layer Assemblies

By

Jodie Lee Lutkenhaus

B.S. Chemical Engineering
University of Texas at Austin, 2002

SUBMITTED TO THE DEPARTMENT OF CHEMICAL ENGINEERING IN PARTIAL FULFILLMENT OF THE REQUIREMENTS FOR THE DEGREE OF

DOCTORATE OF PHILOSOPHY IN CHEMICAL ENGINEERING
AT THE
MASSACHUSETTS INSTITUTE OF TECHNOLOGY

JUNE 2007

Signature of Author: _____
Department of Chemical Engineering
May 8th, 2007

Certified by: _____
Paula T. Hammond
Bayer Chair Professor of Chemical Engineering
Thesis Supervisor

Accepted by: _____
William M. Deen
Professor of Chemical Engineering
Chairman, Committee for Graduate Students

Ion Transport and Structure of Layer-by-Layer Assemblies

by

Jodie Lee Lutkenhaus

Submitted to the Department of Chemical Engineering
On May 8, 2007 in Partial Fulfillment of the Requirements for the Degree of
Doctor of Philosophy in Chemical Engineering
At Massachusetts Institute of Technology

Abstract

Layer-by-layer (LbL) films of various architectures were examined as potential solid state electrolytes for electrochemical systems (e.g. batteries and fuel cells). The relationship between materials properties and ion transport within LbL films was investigated in three systems, described below. The observed structure and properties aid in the design of tunable ultra thin electrolytes.

The thermal and mechanical properties of PEO/PAA films were evaluated, aided by a new peel-away technique. Results indicated that the glass transition temperature (T_g) of PEO/PAA films decreases with increasing assembly pH, but when assembled in the presence of salt, the T_g remains constant. Results indicate that the degree of *inter-* and *intra*molecular PAA hydrogen bonding, evidenced by FTIR spectroscopy, controls the observed T_g. The ionic conductivity was found to increase with increasing charge carrier concentration (doping during assembly) and with humidity. Maximum room temperature dry conductivity was ~10^{-8} S cm^{-1}.

Polymer-clay nanocomposites were investigated for structural and transport anisotropy. LPEI/Laponite/PEO films demonstrated an oriented structure where clay nanoplatelets lay parallel to the substrate and assembly in sheets with polymer in-between. In-plane conductivity was 100 (or 7) times higher than cross-plane conductivity in the dry (or 53 % humidity) state.

Porous coatings of LPEI and PAA were investigated as potential ultra thin porous supports for non-aqueous liquid electrolyte. The effect of assembly pH and post-assembly treatment ph upon the pore size, porosity, surface roughness and structure was study. Films assembled at ph 5 and treated at pH 2.25 demonstrated the highest porosity (77 %) and two room temperature, dry conductivities of 10^{-6} and 10^{-9} S cm^{-1}. The two observed conductivities, or time constants, was attributed to ion transport through liquid-filled pores and the matrix itself.

Thesis Supervisor: Paula T. Hammond
Title: Bayer Chair Professor of Chemical Engineering

Table of Contents

List of Figures

List of Tables

Acknowledgements

This work is dedicated to my husband, Benjamin A. Wilhite, who has encouraged and supported me through it all.

I thank my advisor, Paula T. Hammond, for giving me the opportunity to grow as a scientist in her laboratory. Also, I thank members of the Hammond group including Eric Verploegen, Nathan Ashcraft, Ryan Waltezko, Pil Yoo, Geoff Lowman, Dean DeLongchamp, Avni Argun, Kris Stokes, Juhyun Park and Kris Wood. My two closest friends and labmates at MIT, Marriane Terrot and Nicole Zacharia were the highlights of life in the Hammond lab. This work would not have been possible without the diligent work of my undergraduate students Kathleen McEnnis, Kristin Hrabak and Amit Desai.

I thank Professor Donald Sadoway , Professor Anne Mayes and Professor Yang Shao-Horn for teaching me electrochemistry and letting me explore their laboratories. Elsa Olivetti has also been instrumental in aiding with electrochemical expertise and general spunkiness. I also thank Karen Gleason and John Lock for letting me explore the electrochemistry of thin films and conductive polymers for fun. I thank Professor Rubner and Professor Cohen for helpful discussion. Also, I thank Jenny Lichter.

Outside MIT, I thank Professor Kookheon Char of Seoul National University for his thoughtful discussions during his time on sabbatical. I also thank his masters student, JinHwa Seo.

For personal support, I thank Bryan Cord, Kathleen Navarro, Miranda Newbery, Lily Tong, Malancha Gupta, Holly Stanton and Cara Rhea.

My sister, Jessica Winter, was first and foremost my inspiration for choosing chemical engineering and for choosing graduate school. I deeply thank her for mentoring me as a young and budding scientist.

Chapter 1 : Introduction and Background

Portions of this chapter are reproduced from Lutkenhaus, J. L. and Hammond, P. T. *Soft Matter* with permission of RSC Publishing.

1.1 Introductory Remarks and Technical Summary

Every electrochemical system requires an electrolyte to separate the electrodes and to maintain electrical communication via ion diffusion and migration. The ideal electrolyte would be mechanically robust, ionically conductive, electronically insulating and stable. In general, the ionic conductivity of a solid is orders of magnitude lower than a liquid, which is a significant barrier to designing solid state electrochemical systems. However, the conductance of a solid polymer electrolyte can compete with that of a liquid, if the solid is made sufficiently thin.

The layer-by-layer (LbL) technique, employing the alternate adsorption of oppositely charged moieties (hydrogen bond donor and acceptor), is a potential tool for fabricating ultra thin (10 μm) solid-state electrolytes of tunable materials properties (composition, T_g, thickness, cross-link density). Each cycle, or layer pair, deposits Å to nm of material, and conformal coatings of challenging geometries are possible. The architecture and structure of a material created using the layer-by-layer assembly technique can have a significant impact on the way ions move. This work examines a broad scope of architectures: free-standing hydrogen bonded blends, layered polymer-clay nanocomposites, and micron- to nano-scale porous thin films – all of which conduct protons and lithium ions in their own unique manner.

Amorphous polyethylene oxide (PEO) is a key material in solid polymer electrolytes, but neat PEO is mostly crystalline. Through the use of hydrogen bonding interactions with polyacrylic acid (PAA), layer-by-layer assembly allows for the incorporation of PEO in a thin film; However, little is known of the bulk properties of PEO/PAA LbL assemblies or the state of PEO within the film owing to difficulty in isolating the assembly. Here, a new method of LbL film isolation is introduced that uses low-energy

surfaces, facilitating the removal of substantial mass and area of the film. For the first time, the thermal and mechanical properties, as well as the state of PEO within the LbL film is studied. PEO/PAA films are investigated using differential scanning calorimetry (DSC), dynamic mechanical analysis (DMA) and tensile testing. A single glass transition temperature is observed, and the melting peak of PEO is absent. Films behaved as miscible blends with elastomeric qualities when plasticized with H_2O at ambient conditions. The pH-controlled deconstruction of hydrogen-bonded LbL films is also presented.

With this new methodology available, the affect of pH and ionic strength is rigorously characterized. By adding lithium salt to each assembly bath, the LbL film may be doped with lithium as a strategy to improve the dry state ionic conductivity. The degree of inter- and intra- molecular hydrogen bonding is estimated from Fourier-transform infrared (FTIR) spectroscopy, the glass transition temperature is measured using DSC and ionic conductivity is studied using electrochemical impedance spectroscopy (EIS). Results indicate that (PEO/PAA) LbL multilayers assembled without added salt are highly sensitive to pH where T_g decreases (59 to 26 °C) and intermolecular hydrogen bonding increases (27 to 51 % free COOH in PAA) with increasing assembly pH (2 to 3). Films assembled in the presence of 0.1 M lithium triflate exhibit properties that are independent of assembly pH (T_g = 48 °C and 12 % free COOH in PAA). This lack of pH-dependency is thought to arise from the competitive hydrogen bonding of PAA with itself and with PEO. Ionic conductivity at 0 % humidity is found to range from 10^{-7} S cm^{-1} to 10^{-10} S cm^{-1}, depending on humidity and salt content. Results presented here are compared to other hydrogen-bonded LbL systems as well as solution-cast complexes.

The structure of polymer-clay composites created from layer-by-layer (LbL) assembly can dramatically influence the observed materials properties with respect to orientation. Stratification may prove advantageous for blocking fuel cross-over in a fuel cell, but its affect upon ionic conductivity is unknown. Here, ultra thin LbL assemblies of negatively charged Laponite, positively charged poly(ethylene imine) and neutral poly(ethylene oxide) demonstrated significant orientation over large areas (> 4 cm^2), in which clay platelets assemble parallel to the substrate surface. X-ray photon spectroscopy (XPS), wide-angle x-ray scattering (WAXD), grazing incidence X-ray scattering (GI-SAXS),

atomic force microscopy (AFM), and scanning electron microscopy (SEM) is used to elucidate the structure of the inorganic-organic composite. As a result of two-dimensional self-assembly, observed ionic conductivities were highly anisotropic, with in-plane conductivity 100 times higher than cross-plane conductivity. Understanding the influence of layered structure from the LbL technique can aid in the design of single-ion conductors, gas and liquid permeation barriers, and discrete blocking layers.

Microporous LbL assemblies are a potential route to creating ultra thin porous supports for non-aqueous liquid electrolyte. Ultimately, the ionic conductivity of a liquid and the mechanical properties of a solid are desired in this composite electrolyte. The structure and formation of nano- and microporous LbL assemblies consisting of LPEI and PAA was investigated. Pore size and porosity was found to be highly dependent on processing parameters such as assembly pH and post-assembly treatment pH. Porosity reaching 80 % was possible at optimum conditions of assembly pH 5 and treatment pH 2.25. Porous films exhibited multiple structures ranging from asymmetric membranes to isolated crater-like pores. From capillary forces, liquid electrolyte was wicked into the porous films and the ionic conductivity was measured. Two conductivities, or two time constants, were observed (10^{-6} and 10^{-9} S cm^{-1}), and these were attributed to the presence of two phases (liquid and solid, respectively).

Together, these three architectures highlight how the materials properties of LbL films may be understood and controlled in order to design the ideal solid state electrolyte. The LbL technique provides a promising means of creating functional, ionically conductive membranes and coatings.

1.2 Electrochemical Cells: General Considerations

With an increasing need for energy-dense portable power, the role of the materials and interfaces within an electrochemical cell (i.e. fuel cells or batteries) become significant. Electrochemical energy is derived from the direct transfer of chemical energy to electricity. This transfer is facilitated by an **electrochemical cell** consisting of three components: **cathode**, **anode**, and **electrolyte**. Oxidation occurs at the anode; reduction, at the cathode. The electrolyte serves to physically separate the anode and the cathode, as well as to maintain electrical conductivity via ion migration and diffusion. Because

electrons are not "soluble" in the electrolyte, they are forced to move through an external circuit to complete the reduction and oxidation reactions, generating an electrical current. Examples of two electrochemical energy cells are described in Figure 1-1 and Figure 1-2.

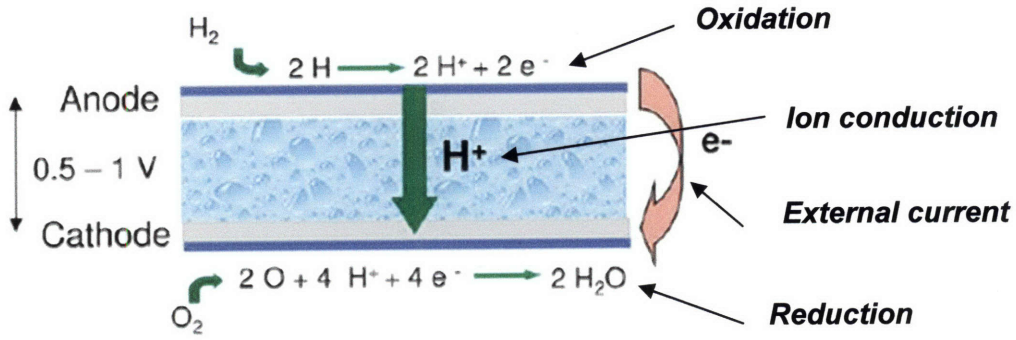

Figure 1-1. An open electrochemical system: example proton-exchange membrane fuel cell.[1] The anode and cathode are made of carbon-supported platinum. Hydrogen is oxidized at the anode, and oxygen is reduced at the cathode. The proton-conducting electrolyte is usually hydrated Nafion® membrane. Reproduced with permission from RSC Publishing.

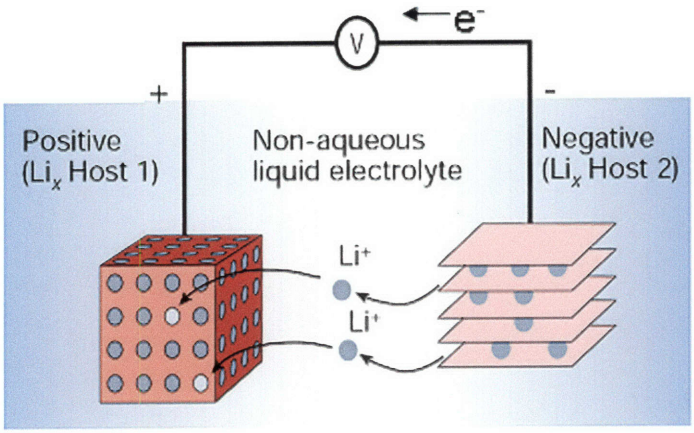

Figure 1-2. A closed electrochemical system: example Li-ion battery based upon intercalation electrodes.[2] The positive electrode, the cathode, is commonly $LiCoO_2$; the anode, the negative electrode, is usually carbon black or graphite. The non-aqueous liquid electrolyte is a cocktail of cyclic carbonates and lithium salt such as lithium hexaflurophosphate. Reproduced with permission from Nature Publishing.

A **fuel cell** is an open electrochemical system capable of employing a variety of fuels to generate electrical power. The two most common fuel cells today are the proton-exchange membrane fuel cell (PEMFC) and the direct-methanol fuel cell (DMFC). A PEMFC reacts hydrogen fuel with oxygen (typically from air), while the DMFC reacts methanol fuel with oxygen / air. In both cases, oxygen is reduced at the cathode and fuel (hydrogen or methanol) is oxidized at the anode. The electrolyte is a proton-conducting sulfonated fluoropolymer, most commonly Nafion®. Fuel combustion by-products (water from hydrogen, water and carbon dioxide from methanol) are released from the fuel cell. Numerous texts explain fuel cells in greater detail.[1, 3-5] Because of multiple limitations (fuel storage, durability, energy density), fuel cells have not been broadly implemented in current electronics.

On the other hand, Li-ion batteries are widely used in a variety of applications such as notebook computers and cell phones. A battery is considered a closed system, where no by-products exist, assuming the system is rechargeable. In a Li-ion battery the cathode is usually $LiCoO_2$ and the anode is carbon or graphite. Both are intercalation electrodes where lithium cations will insert and de-insert during charge and discharge. In the case of the cathode, cobalt is reduced (not lithium) upon lithium insertion (Li^+ + $Co(IV)O_2 \rightarrow LiCo(III)O_2$). The electrolyte in conventional Li-ion batteries is a non-aqueous mixture of lithium salt and high-dielectric constant solvent. The system must be kept water-free to prevent the formation of lithium hydroxide and hydrogen gas, which is a potential safety concern ($Li^+ + H_2O \rightarrow LiOH + 1/2H_2$). In efforts to create a solid-state battery, the non-aqueous electrolyte is often replaced with a polymer such as polyethylene oxide doped with lithium salt. The operation of Li-ion batteries is described in detail by multiple sources.[2, 6-8]

Regardless of the application, both types of electrochemical cells (open and closed) are governed by the same electrochemical principles. The "rest" potential of the cell, or the **open circuit voltage**, is dictated by thermodynamics as follows:

$$\Delta G = -nFE_{ocv} \qquad \text{Equation 1}$$

Where ΔG is the Gibbs free energy of the overall reaction, n is the number of electrons transferred per mole of reaction, F is Faraday's constant and E_{ocv} is open circuit voltage or potential. As current is drawn from the cell, the real potential declines from parasitic

losses such as activation overpotential (kinetic limitations), concentration polarization (mass transfer limitations), and ohmic loss (electronic and ionic conductivity limitations). Each loss represents lost useful energy and decreases overall efficiency. *The focus of this thesis is to address the role of the solid layer-by-layer electrolyte and its relation to ohmic loss and ionic conductivity. Fundamental understanding of materials properties and ion transport processes in relation to layer-by-layer structure can be used in the design of tunable electrochemical energy systems.*

1.3 Electrolytes for Electrochemical Energy

As mentioned above, the purpose of the electrolyte is to conduct ions and to mechanically separate the anode and cathode. Should the electrodes touch each other, a short circuit would develop that would render the cell useless, and should the electrolyte be a poor ion conductor, neither electrode would communicate with the other. Thus, the electrolyte should be ionically conductive and electronically insulating. The **ionic conductivity** of the electrolyte (σ) is related to **ohmic loss** (η_Ω) as follows:

$$\eta_\Omega = iR = iL/\sigma A \qquad \text{Equation 2a}$$

$$R = L/\sigma A \qquad \text{Equation 2b}$$

where R is the resistance of the electrolyte, i is the current drawn from the cell, L is the thickness between electrodes and A is the area of the electrodes. Ohmic loss is also related to the potential of the cell as follows:

$$E = E_{ocv} - \eta_\Omega. \qquad \text{Equation 2c}$$

Combining the three gives a general relationship for the conductivity and the real potential of the cell:

$$E = E_{ocv} - \frac{iL}{\sigma A} \qquad \text{Equation 2}$$

The implications of this relationship are that (i) thinner electrolytes (decreasing L), (ii) more conductive electrolytes (increasing σ), and (iii) conformal coverage (increasing A) decrease ohmic loss. The layer-by-layer technique is a potential means to address these three issues, discussed later.

The nature and theory of ion transport within electrolytes is described elsewhere.[9-12] Briefly, the **ionic conductivity** of an electrolyte is related to the conductivity of each mobile species, i.e.,

$$\sigma = \sum n_i q \mu_i \qquad \text{Equation 3}$$

where n is the number of charge carriers of species i, q is electrical charge and μ is the mobility species i. Because an electrolyte might have multiple charge carriers, as in the case of a dissolved salt (anions and cations), the observed conductivity is the total conductivity, hence the summation term in Equation 3. Two possible routes to increasing conductivity are increasing the concentration of charge carriers (i.e. doping) and increasing the mobility of those charge carriers. The mobility of species i is dictated by the Nernst-Einstein equation:

$$\mu_i = \frac{qD_i}{kT} \qquad \text{Equation 4}$$

where D_i is the diffusion coefficient of species i, k is Boltzmann's constant and T is temperature. In order to increase the mobility of species i (or increase conductivity) the diffusion of i must be enhanced.

A significant consequence of the relationship between diffusion, mobility and conductivity is that the phase of the electrolyte can play an important role. For example, a liquid electrolyte might exhibit a diffusion constant that is orders magnitude higher than a solid polymer electrolyte. Inherently, to replace a liquid with a solid electrolyte results in lower conductivity and higher ohmic loss. This challenge is further described for battery and fuel cell electrolytes.

Besides conducting ions, an electrolyte must also operate reliably and safely. Given the extreme conditions of both fuel cells (acidic environment, peroxide formation) and batteries (reaction with lithium, water-sensitivity), the electrochemical, thermal and mechanical stability of the electrolyte are of utmost importance.

To summarize, the main requirements of an electrolyte are listed below:

- Ultra thin (< 10 μm)
- Conformal coverage
- High ionic conductivity
    - High charge carrier concentration
    - High carrier mobility
- Stability

1.3.1 "Dry" Electrolytes

Dry electrolytes are key components of Li-ion batteries, which are highly water-sensitive. Current state-of-the-art devices includes a non-aqueous liquid electrolyte supported by a porous separator ~25 μM in thickness.[13-16] For applications requiring increased durability, mechanical flexibility and safety, a solid electrolyte medium is desired. By far, the most widely explored solid polymer electrolyte for Li-ion battery applications is polyethylene oxide (PEO).[2, 10, 17, 18] This polar polymer (Figure 1-3) is capable of solvating lithium salt via the favorable ether-alkali interaction of PEO and Li^+, and provides sufficient local relaxation and segmental motion so as to yield a respectable room temperature conductivity, ~10^{-7} S cm^{-1}, when lithium triflate is the salt. This highly flexible polymer electrolyte encourages ion conduction by its increased ability to cradle and swing an ion along its path. Conductivity is attributed to the amorphous phase, which is further facilitated by PEO's low glass transition temperature (T_g) of -56 °C. However, PEO-salt mixtures are partially crystalline at room temperature, essentially diluting the amorphous conductive medium. In contrast, the conductivity of the conventional non-aqueous liquid electrolyte is greater than 10^{-3} S cm^{-1}, and for PEO to compete, a significant improvement is required. Common strategies for improving the lithium conductivity of PEO include adding a plasticizer, disrupting the crystalline phase of PEO or choosing a salt with a less mobile anion.[17]

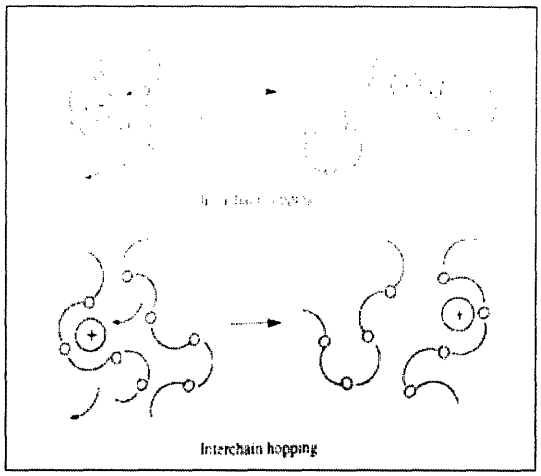

Figure 1-3. Polyethylene oxide as a solid polymer electrolyte.[10] Lithium cations, solvated by the ether-alkali interactions, are transported through segmental motion of the polymer. Cations may be transported from one chain to the next.

As illustrated in Figure 1-3, the flexibility and segmental motion of a polymer chain is key to ion transport in the dry state.[10, 17] At a temperature above its T_g, bulk polymer is "rubbery" and capable of segmental motion, whereas below the T_g, the matrix behaves as a stiff glass. Stiff chains may still solvate lithium cations, but without segmental motion, ions stagnate in the glassy matrix. Polymers with hetero-atomic backbones such as PEO or polyethylene imine (PEI) exhibit increased flexibility and reduced glass transition temperatures, making them good solid state electrolyte candidates. In general three characteristics are desired for the conductivity of solid polymer electrolytes:

- Low barriers to bond rotation
- Electron-donor power (or polarity) to form co-ordinate bonds with the cation
- Sufficient distance between co-ordinating sites to encourage ion transport

1.3.2 "Wet" Electrolytes

Though this thesis primarily focuses on ion transport in the dry state, the characteristics of humid or dry membranes is an essential concern for open electrochemical systems. For example in a fuel cell, the hydration of a proton-exchange membrane can dramatically affect conductivity[19] and is a critical component of system design. When humidity is greater than 80 %, Nafion® will rearrange to form sulfonate-lined water-filled nanopores,

as illustrated in Figure 1-4. Protons "hop" along water molecules within the pores via the Grotthus mechanism,[20] meaning the conductivity is "liquid-like." Removing water from the Nafion® membrane eliminates the nanoporous structure and conductivity falls. Typical Nafion® membranes (> 100 μm thick) exhibit conductivities greater than 0.01 S cm^{-1} at 80 °C and 100 % humidity. As mentioned earlier thinner membranes are desirable; in the case of fuel cells, thin membranes introduce pronounced fuel crossover, which limits efficiency. The permeation of hydrogen or oxygen across the membrane decreases the magnitude of the Gibbs free energy of the reaction, and lowers the open circuit potential. Even before current is drawn, a cell with significant fuel crossover will exhibit parasitic loss from the mixing of fuels. An ultra thin membrane (< 10 μm) capable of conducting protons without fuel crossover would provide a critical breakthrough in fuel cell design.

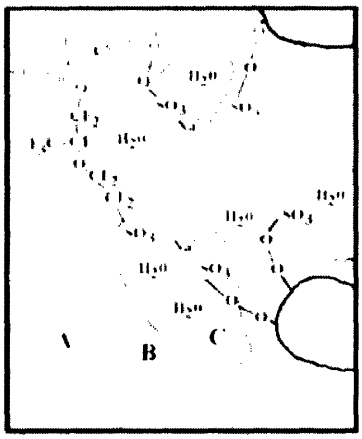

Figure 1-4. Nafion® as a proton-exchange membrane.[21] Hydrated Nafion® phase separates into water-filled nanopores and Teflon®-like solid matrix. Protons travel along water molecules via the Grotthus mechanism. Image reprinted with permission from Prof. Kenneth Mauritz.

1.4 Layer-by-Layer Assembly Technique

Functional thin films created using chemical vapor deposition, atomic layer deposition, Langmuir-Blodgett deposition, colloidal assembly and molecular beam epitaxy have been explored for decades as alternative materials for electrochemical systems, but few of

these have been commercially realized – perhaps because the requirements of an electrochemically active material are many. Of many nano-fabrication methods, the aqueous layer-by-layer (LbL) assembly technique offers the finest control and tunability of materials properties and architecture at the nanometer scale, and is the simplest and most cost-effective method to implement. The LbL technique, which is based upon the alternate adsorption of oppositely charged species from aqueous solution, possesses unprecedented control of materials selection (*e.g.* polyelectrolytes, clays, nanoparticles, proteins), materials properties (*e.g.* conductivity, glass transition temperature) and architecture (*e.g.* blends, stratified-layers, pores). These advantages make LbL assemblies promising candidates for use in fuel cells, batteries, electrochromic devices, solar cells, and sensors.

1.4.1 Methodology

The LbL technique is based upon the alternate adsorption of cationic and anionic species,[22-25] or hydrogen bond donor and acceptor,[26, 27] (Figure 1-5). This assembly procedure may be repeated for *n* cycles to give molecularly thin (Å to nm per cycle) multilayers adsorbed upon the substrate, whether that be glass, silicon, ITO, colloids[28] or Teflon®.[29, 30] Usually constructed by dipping a substrate in aqueous solutions, the LbL technique has also been extended to alternate misting,[31, 32] spin-assisted assembly[33] and electrophoretic deposition.[34] These alternative methods may increase processing speed by 100 times. What makes this method of self-assembly particularly versatile is that any multiply charged (or hydrogen-bonding) species can be incorporated, including sensitive materials such as proteins and DNA, as well as functional or structural materials such as clays, polyoxometalates, nanoparticles, dendrimers and quantum dots. In this manner, a multitude of electrochemically active materials can be placed within pre-selected layers to create ultra thin electrodes, electrolytes and complete devices – all at the nano- to micrometer scale.

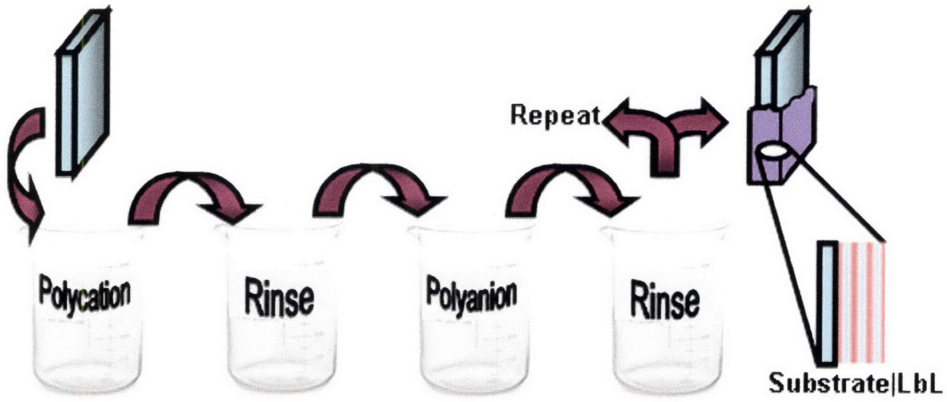

Figure 1-5. The layer-by-layer technique is the solution-based alternate adsorption of positively and negatively charged species (or hydrogen bond donors and acceptors). Rinses between adsorptions steps wash away excess material. The resulting film may be either interdigitated or stratified in structure.

Recent discoveries regarding the connection between internal architecture and function in LbL assemblies show great promise, particularly in the areas of electrochemical energy. Because the method involves solution adsorption of charged (or hydrogen-bonding) species to a surface, *multilayers conformally coat any substrate surface regardless of geometry or feature size*; in other words, a rough surface such as a cathode may be fully coated by an LbL assembly in order to maximize the active interfacial area. Conversely, surfaces may be templated with polymer-on-polymer stamping to pattern multilayer adsorption,[35, 36] yielding features and potentially devices at the sub-micron scale. Also, the control of film architecture throughout its thickness leads to the ability to vary materials content in a continuous fashion or to generate discrete layers, allowing the construction of a range of devices. Hybrid composites of varying complexity can be fabricated using both inorganic and organic materials. Another advantage is that material adsorption and device performance are highly tunable with parameters such as pH, ionic strength and thickness (number of layers).[37] Furthermore, mass transport and electrical conductivity within an LbL assembly can be selectively tuned through the creation of a homogeneous, blended matrix or a microporous network. These discoveries provide the basis for creating exciting new materials and interfaces for electrochemical systems.

With the advantages listed above and the flexibility of the technique, many technologies have been recently explored,[38-42] (Figure 1-6. The LbL assembly technique is a powerful tool for creating functional materials for a variety of applications. A multitude of materials and control parameters are capable of creating made-to-order coatings and films.). Great advances have been made in the fields of drug delivery,[43, 44] antimicrobial coatings,[45] anticorrosion coatings,[46] super-hydrophobic coatings,[47] light-emitting diodes,[48-59] electronically conductive polymers,[26, 60-72] electrolytes, fuel cells, batteries, electrochromics, photovoltaics and biosensors.

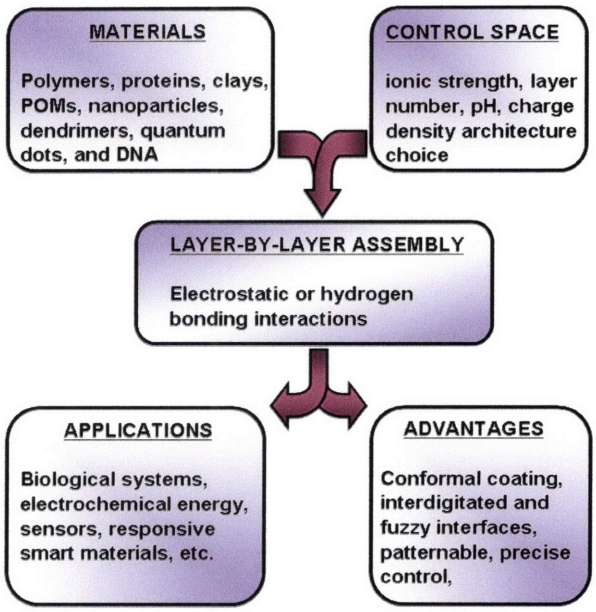

Figure 1-6. The LbL assembly technique is a powerful tool for creating functional materials for a variety of applications. A multitude of materials and control parameters are capable of creating made-to-order coatings and films.

1.4.2 Layer-by-Layer Assemblies as Solid Polymer Electrolytes

Every electrochemical system requires an electrolyte to transport ions from electrode to electrode. The first fundamental explorations[73, 74] of ion transport within multilayer thin films indicated that film structure and materials choice greatly impacts ionic conductivity; these early studies formed the basis for thinking of LbL thin films as solid

state electrolytes. Durstock and Rubner[73] first investigated the dielectric properties of multilayers to understand the performance of their electroluminescent devices. Multilayers of positively charged poly(allylamine hydrochloride) (PAH) and negatively charged poly(acrylic acid) (PAA) exhibited a dry and hydrated (85 to 90% relative humidity) conductivity of $3 \cdot 10^{-12}$ S cm^{-1} and $2 \cdot 10^{-7}$ S cm^{-1} at 23 °C, respectively. The dramatic increase of conductivity with humidity was attributed to the absorption of water, which acts as a plasticizer. Still, these reported values were too low for use as a practical device electrolyte. Later, Farhat and Schlenoff[74, 75] studied ion transport in multilayers of negatively charged poly(styrene sulfonate) (PSS) and positively charged poly(diallyldimethylammonium chloride) (PDAC). The resulting film was highly cross-linked and behaved as a so-called reluctant ion-exchanger owing to the hydrophobic nature of the bulk composite. These early studies highlight how the hydrophilicity of an LbL thin film affects ion mobility: hydrophilic materials are desired to provide a favorable environment for ion solvation and transport.

The role of water in an LbL assembly is an important one; hydrophilic films absorb water and in turn, ionic conductivity increases. Such attributes are essential for creating proton exchange membranes (PEMs) for hydrogen and direct methanol fuel cells, which operate in a humid environment. In LbL films saturated with water, proton conduction occurs *via* the Grotthus mechanism,[20] where protons "hop" along water molecules. An LbL assembly with hydrophilic components absorbs more water, and ions travel more easily through the water clusters absorbed in the polymer matrix. By using hydrophilic weak polyelectrolytes assembled at, or near, their pKa's, DeLongchamp and Hammond[76] were able to improve ion transport in LbL thin films by decreasing the ionic cross-link density and increasing the thickness per layer pair to give a loose and loopy architecture. Fast ion conduction was achieved with linear polyethylene imine (LPEI)/PAA and LPEI/poly(2-acrylamido-2-methyl-1-propanesulfonic acid) (PAMPS) multilayer thin films, $\sigma = 1.0 \cdot 10^{-5}$ S cm^{-1} and $\sigma = 1.5 \cdot 10^{-5}$ S cm^{-1} at 100% relative humidity (RH) and 25 °C, respectively. These materials readily absorb water and produce robust, stable LbL films at high humidity. In contrast, the hydrated conductivity of Durstock and Rubner's[73] PAH/PAA assemblies was 100 times lower than the LPEI/PAA system because of the character of PAH, which creates a hydrophobic multilayer interior that is inhospitable to

ion transport. Of existing LbL systems, the current leader in proton conduction is the hydrogen-bonded assembly of polyethylene oxide (PEO) and PAA, where PAA is a hydrogen bond donor and PEO is an acceptor. DeLongchamp et al.[77] measured an ionic conductivity of $5.5 \cdot 10^{-5}$ S cm^{-1} at 100% RH and room temperature. The high conductivity is attributed to the hydrophilic nature of PEO and PAA, and the inhibition of PEO crystallinity.

In comparison, solid-state *dry* polymer electrolytes conduct ions very differently. Without absorbed water, ion transport in the dry state depends more upon the segmental motion of the polymer electrolyte chain. For example in PEO, the cation of interest such as Li^+ for a Li-ion battery, is solvated by polar moieties along the polymer chain, and the cation moves from the segmental motion of the polymer host. In this case, ion transport in a dry environment depends upon the polarity of the polymer, glass transition temperature of the matrix and cross-link density. The ideal LbL solid-state electrolyte would have a low glass transition temperature (T_g) to enhance segmental motion, a loopy lightly cross-linked architecture to allow ion and polymer motion, and polar functionality to solvate ions while avoiding excessive ion trapping. First measurements by Durstock and Rubner, mentioned above, indicated a low dry ionic conductivity in PAH/PAA multilayers (10^{-12} S cm^{-1}), which was attributed to the high electrostatic cross-link density between PAH and PAA and the low segmental motion of individual polymer chains, typical of a material below its glass transition temperature. However, with proper materials selection, the ionic conductivity can be significantly improved, as shown with dry PEO/PAA thin films.

Hydrogen bonded LbL assemblies of PEO and PAA are among the strongest candidates for dry LbL polymer electrolytes, because amorphous PEO can transport ions through segmental motion (T_g = ⁻56 °C) and the polar ether group readily solvates lithium cations. Under dry conditions, DeLongchamp and Hammond[77] demonstrated an ionic conductivity of 10^{-10} S cm^{-1} at 25 °C in PEO/PAA films assembled at pH 2.5 and exposed to lithium triflate during assembly, which is 100 times higher than the PAH/PAA system. DeLongchamp suggested that conductivity of the PEO/PAA thin film was impeded because of hydrogen-bond cross-links, ion traps from the carboxylic acid group in PAA, and poor segmental motion (or high T_g). Unfortunately at that time, the glass transition

temperature of the PEO/PAA film could not be measured because a method of isolating substantial mass and area of the hydrogen-bonded film was unavailable. *In this thesis, a new methodology is developed to isolate LbL film to measure its materials properties.*

Altering the morphology of an LbL thin film to produce a porous matrix can further enhance ion transport. Empty pores can act as reservoirs for liquid or gel electrolytes capable of fast ion conduction; this porous structure yields the transport properties of a liquid and the mechanical properties of a solid. Porous phase transitions have recently been observed by Rubner and coworkers,[78, 79] created by briefly immersing multilayers of PAH/PAA[78] or LPEI/PAA[79] in a transition bath of acidic pH. The change in pH protonates (or deprotonates) polyelectrolytes within the LbL film and induces morphological rearrangement realized by a porous structure. It has been recently shown that fast ion conduction in porous LPEI/PAA assemblies can be achieved when polyethylene glycol (PEG) oligomers and LiI fill the pores.[79] While the ionic conductivity of the neat liquid-like PEG mixture was 10^{-3} S cm^{-1}, porous LPEI/PAA assembly conductivity reached 10^{-4} S cm^{-1} at room temperature and 22% RH as ions migrated through the PEG-filled pores. Even then, little was known about the structure of these porous LPEI/PAA materials. *The ability to control and tune the pore size, structure and conductivity of porous LPEI/PAA LbL films is presented in this thesis.*

These studies laid the ground work for tuning LbL film structure and properties for applications requiring fast ion conduction. Here, the architecture of an LbL film and its ability to conduct ions is rigorously examined.

1.5 LbL Thesis Overview

In this thesis, the connection between transport properties (i.e. conductivity) and fundamental materials properties (e.g. cross-link density, ionization, structure, polyion content) in LbL thin films is investigated. Three LbL architectures are examined as solid polymer electrolytes: (i) free-standing hydrogen bonded blends, (ii) layered polymer-clay nanocomposites, and (iii) micro- to nano-scale porous thin films – all of which conduct ions in their own unique manner.

Hydrogen-bonded LbL systems of polyethylene oxide and polyacrylic acid were studied using differential scanning calorimetry (DSC), thermal gravimetric analysis

(TGA), dynamic mechanical analysis (DMA) and impedance spectroscopy. PAA was selected as a candidate hydrogen bond donor in a strategy to disrupt the crystallization of PEO. From DSC, crystallization of PEO within an LbL film is completely suppressed, and for the first time, the glass transition temperature of an LbL film is detected. The determination of the thermal and mechanical properties was facilitated by the development of a new methodology to isolate substantial mass and area of LbL film, described in **Chapter 2**. The effect of assembly parameters such as pH and ionic strength upon the thermal properties and ionic conductivity are extensively described in **Chapter 3**.

Also, ion transport in layered polymer-clay nanocomposites is addressed. It is believed that nano-objects of high aspect ratio such as layered silicates may be capable of blocking fuel crossover in a fuel cell, but ion transport may be blocked. **Chapter 4** examines anisotropic transport resulting from layered structure created during LbL assembly of polyethylene imine, Laponite clay and polyethylene oxide. X-ray diffraction (XRD), grazing-incidence small angle X-ray scattering (GI-SAXS), scanning electron microscopy (SEM), atomic force microscopy (AFM) and impedance spectroscopy were performed on polymer-clay LbL assemblies; observed data indicate that these polymer-clay films are highly anisotropic where transport in one direction is highly favored over another.

Finally, the structure, formation and transport properties of nano- and micro-porous LbL assemblies consisting of polyethylene imine and polyacrylic acid are studied using AFM, SEM, optical microscopy and impedance spectroscopy. By filling the pores with a liquid electrolyte, the solid-liquid composite may transport ions like a liquid while acting as a solid support. **Chapter 5** details the effect of assembly pH and post-processing conditions that yield a variety of structure ranging from isolated pores to asymmetric membranes.

Future recommendations and the general outlook for LbL solid polymer electrolytes are detailed in **Chapter 6**. The **Appendix** describes the instrumentation and theory used.

1.6 References

1. de Bruijn, F. *Green Chemistry* **2005,** 7, 132-150.
2. Tarascon, J.; Armand, M. *Nature* **2001,** 414, 359-367.
3. Handbook of fuel cells : fundamentals, technology, and applications. In *Fundamentals and survey of systems*, Vielstich, W.; Lamm, A.; Gasteiger, H. A., Eds. Wiley: 2003; Vol. 1.
4. Larminie, J.; Dicks, A., *Fuel cell systems explained.* Wiley: Chichester, 2003.
5. Xianguo, L., *Principles of fuel cells.* Taylor and Francis: New York, 2006.
6. Dell, R. M., *Understanding batteries.* Royal Society of Chemistry: Cambridge, 2001.
7. Vincent, C. A.; Scrosati, B., *Modern batteries: an introduction to electrochemical power sources.* John Wiley and Sons: New York, 1997.
8. Linden, D.; Reddy, T. B., *Handbook of batteries.* McGraw-Hill: New York, 2001.
9. Bard, A.; Faulkner, L., *Electrochemical Methods: Fundamentals and Applications.* Second ed.; John Wiley and Sons, Inc.: Hoboken, 2001.
10. Gray, F. M.; Royal Society of Chemistry (Great Britain), *Polymer Electrolytes.* Royal Society of Chemistry: Cambridge, 1997; p 175.
11. Bruce, P. G., *Solid State Electrochemistry.* Cambridge Univeristy Press: New York, 1995.
12. Newman, J.; Thomas-Alyea, K. E., *Electrochemical systems.* Wiley: Hoboken, 2004.
13. Stephan, A. M. *European Polymer Journal* **2006,** 42, 21-42.
14. Zhang, S. S. *Journal of Power Sources* **2007,** 164, (1), 351-364.
15. Chagnes, A.; Carre, B.; Willmann, P.; Dedryvere, R.; Gonbeau, D.; Lemordant, D. *Journal of the Electrochemical Society* **2003,** 150, (9), A1255-A1261.
16. Abraham, K. M.; Alamgir, M. *Journal of the Electrochemical Society* **1995,** 142, (3), 683-687.
17. MacCallum, J. R.; Vincent, C. A., *Polymer Electrolyte Reviews.* Elsevier Applied Science: New York, 1987; Vol. 1.
18. Armand, M. B.; Chabagno, J. M.; Duclot, M. In Second International Meeting on Solid Electrolytes, St. Andrews, Scotland, 1978; St. Andrews, Scotland, 1978.
19. Sone, Y.; Ekdunge, P.; Simonsson, D. *Journal of Electrochemical Society* **1996,** 143, (4), 1254-1259.
20. Hertz, H. G.; Braun, B. M.; Muller, K. J.; Maurer, R. *Journal of Chemical Education* **1987,** 64, (9), 777-784.
21. Maurtiz, K. A. Nafion-Perflurosulfonate Ionomer. 2007.
22. Iler, R. K. *Journal of Colloid and Interface Science* **1966,** 21, (6), 569-594.
23. Decher, G.; Hong, J. D.; Schmitt, J. *Thin Solid Films* **1992,** 210-211, (2), 831-835.
24. Decher, G. *Science* **1997,** 277, (5330), 1232-1237.
25. Decher, G.; Eckle, M.; Schmitt, J.; Struth, B. *Current Opinion in Colloid and Interface Science* **1998,** 3, (1), 32-39.
26. Stockton, W. B.; Rubner, M. F. *Macromolecules* **1997,** 30, (9), 2717-2725.
27. Sukhishvili, S.; Granick, S. *Journal of American Chemical Society* **2000,** 122, (39), 9550-1.
28. Caruso, F. *Australian Journal of Chemistry* **2001,** 54, (6), 349-353.

29. Lutkenhaus, J. L.; Hrabak, K. D.; McEnnis, K.; Hammond, P. T. *Journal of the American Chemical Society* **2005,** 127, (49), 17228-17234.
30. Jaber, J.; Schlenoff, J. B. *Journal of American Chemical Society* **2006,** 128, (9), 2940-2947.
31. Schlenoff, J. B.; Dubas, S. T.; Farhat, T. R. *Langmuir* **2000,** 16, (26), 9968-9969.
32. Krogman, K. C.; Zacharia, N. S.; Hammond, P. T. *Langmuir* **2007,** In press.
33. Cho, J.; Char, K.; Hong, J.-D.; Lee, K.-B. *Advanced Materials* **2001,** 13, (14), 1076.
34. Ngankam, A. P.; Van Tassel, P. R. *Langmuir* **2005,** 21, (13), 5865-5871.
35. Clark, S. L.; Hammond, P. T. *Advanced Materials* **1998,** 10, (18), 1515-1519.
36. Jiang, X.; Hammond, P. T. *Langmuir* **2000,** 16, (22), 8501-8509.
37. Shiratori, S.; Rubner, M. F. *Macromolecules* **2000,** 33, (11), 4213.
38. Kotov, N. A.; Liz-Marzan, L. M., Organization of layer-by-layer assembled nanocomposites: Functional effects in photonics and biomaterials. In *Nanoscale Materials*, Liz-Marzan, L. M.; Kamat, P. V., Eds. Kluwer Academic Publishers: Norwell, Mass, 2003; pp 273-301.
39. Hammond, P. T. *Advanced Materials* **2004,** 16, (15), 1271-1293.
40. Campas, M.; O'Sullivan, C. *Analytical Letters* **2003,** 36, (12), 2551-2569.
41. Decher, G.; Schlenoff, J. B., *Multilayer Thin Films*. Wiley: Weinheim, Germany, 2003.
42. Hammond, P. T. *Current Opinion in Colloid and Interface Science* **2000,** 4, (6), 430-442.
43. Wood, K.; Boedicker, J.; Lynn, D. M.; Hammond, P. T. *Langmuir* **2005,** 21, (4), 1603-1609.
44. Shenoy, D.; Antipov, A.; Sukhorukov, G. B. In *Layer-by-layer nanoengineering with polyelectrolytes for delivery of bioactive materials*, Polymeric Gene Delivery, 2005; Amiji, M. M., Ed. CRC Press LLC: 2005; pp 399-416.
45. Podsiadlo, P.; Paternel, S.; Rouillard, J.-M.; Zhang, Z.; Lee, J.; Lee, J.-W.; Gulari, E.; Kotov, N. A. *Langmuir* **2005,** 21, (25), 11915-11921.
46. Kachurina, O.; Knobbe, E.; Metroke, T. L.; Ostrander, J. W.; Kotov, N. A. *International Journal of Nanotechnology* **2004,** 1, (3), 347-365.
47. Zhai, L.; Cebeci, F.; Cohen, R.; Rubner, M. F. *Nano Letters* **2004,** 4, (7), 1349-1353.
48. Fou, A. C.; Onitsuka, O.; Ferreira, M.; Rubner, M. F.; Hsieh, B. R. *Journal of Applied Physics* **1996,** 79, (10), 7501-7509.
49. Hong, H.; Davidov, D.; Avany, Y.; Chayet, H.; Farggi, E. Z.; Neumann, R. *Advanced Materials* **1995,** 7, (10), 846-849.
50. Kim, J.; Wang, H.-C.; Kumar, J.; Tripathy, S. K. *Chemistry of Materials* **1999,** 11, (8), 2250-2256.
51. Kim, D. W.; Blumstein, A.; Kumar, J.; Tripathy, S. K. *Chemistry of Materials* **2001,** 13, (2), 243-246.
52. Pinto, M. R.; Kristal, B. M.; Schanze, K. S. *Langmuir* **2003,** 19, (16), 6523-6533.
53. Kato, S.; Pac, C. *Journal of Physical Chemistry B* **2004,** 108, (52), 19932-19939.
54. Kato, S. *Journal of the American Chemical Society* **2005,** 127, (33), 11538-11539.
55. Khillan, R. K.; Su, Y.; Lvov, Y. M.; Varahramyan, K. *IEEE Transaction on Components and Packaging Technologies* **2005,** 28, (4), 748-753.

56. Kim, S.; Jackiw, J.; Robinson, E.; Schanze, K. S.; Reynolds, J. R. *Macromolecules* **1998,** 31, (4), 964-974.
57. Ho, P. K. H.; Granstrom, M.; Friend, R. H.; Greenham, N. C. *Advanced Materials* **1998,** 10, (10), 769-774.
58. Ho, P. K. H.; Kim, J.-S.; Burroughes, J. H.; Becker, H.; Li, S. F. Y.; Brown, T. M.; Cacialli, F.; Friend, R. H. *Nature* **2000,** 404, (6777), 481-484.
59. Ramey, M. B.; Hiller, J. A.; Rubner, M. F.; Tan, C.; Schanze, K. S.; Reynolds, J. R. *Macromolecules* **2005,** 38, (2), 234-243.
60. Cheung, J. H.; Fou, A. C.; Rubner, M. F. *Thin Solid Films* **1993,** 244, (1-2), 985-999.
61. Ferreira, M.; Cheung, J. H.; Rubner, M. F. *Thin Solid Films* **1994,** 244, (806-809).
62. Ferreira, M.; Rubner, M. F. *Macromolecules* **1995,** 28, (21), 7107-7114.
63. Fou, A. C.; Rubner, M. F. *Macromolecules* **1995,** 28, (21), 7115-7120.
64. Cheung, J. H.; Stockton, W. B.; Rubner, M. F. *Macromolecules* **1997,** 30, (9), 2712-2716.
65. Ram, M. K.; Salerno, M.; Adami, M.; Faraci, P.; Nicolini, C. *Langmuir* **1999,** 15, (4), 1252-1259.
66. Lukkari, J.; Salomaki, M.; Viinikanoja, A.; Aaritalo, T.; Paukkunen, J.; Kocharova, N.; Kankare, J. *Journal of the American Chemical Society* **2001,** 123, (25), 6083-6091.
67. Zotti, G.; Schiavon, G.; Zecchin, S.; Berlin, A.; Giro, G. *Synthetic Metals* **2001,** 121, (1-3), 1381-1382.
68. Kim, H. S.; Sohn, B. H.; Lee, W.; Lee, J.-K.; Choi, S. J.; Kwon, S. J. *Thin Solid Films* **2002,** 419, (1-2), 173-177.
69. Park, M.-K.; Onishi, K.; Locklin, J.; Caruso, F.; Advincula, R. C. *Langmuir* **2003,** 19, (20), 8550-9554.
70. Trivinho-Strixino, F.; Pereira, E. C.; Mello, S. V.; Oliveria, O. N. *Langmuir* **2004,** 20, (9), 3740-3745.
71. Liang, Z.; Cabarcos, O. M.; Allaara, D. L.; Wang, Q. *Advanced Materials* **2004,** 16, (9-10), 823-827.
72. Trivinho-Strixino, F.; Pereira, E. C.; Mello, S. V.; Oliveria, O. N. *Synthetic Metals* **2005,** 155, (3), 648-651.
73. Durstock, M. F.; Rubner, M. F. *Langmuir* **2001,** 17, (25), 7865-7872.
74. Farhat, T. R.; Schlenoff, J. B. *Langmuir* **2001,** 17, (4), 1184-1192.
75. Farhat, T. R.; Schlenoff, J. B. *Journal of the American Chemical Society* **2003,** 125, (15), 4627-4636.
76. DeLongchamp, D. M.; Hammond, P. T. *Chemistry of Materials* **2003,** 15, (5), 1165-1173.
77. DeLongchamp, D. M.; Hammond, P. T. *Langmuir* **2004,** 20, (13), 5403-5411.
78. Mendelsohn, J. D.; Barret, C. J.; Chan, A. J. P.; Mayes, A. M.; Rubner, M. F. *Langmuir* **2000,** 16, 5017-5023.
79. Lowman, G. M.; Tokuhisa, H.; Lutkenhaus, J. L.; Hammond, P. T. *Langmuir* **2004,** 20, (22), 9791-9795.
80. Young, R. J.; Lovell, P., *Introduction to polymers*. Chapman and Hall: New York, 1991.

81. Painter, P. C.; Coleman, M. M., *Fundamentals of Polymer Science: An Introductory Text*. CRC: New York, 1998.

Chapter 2 : Thermal and Mechanical Properties of Free-Standing Hydrogen Bonded PEO/PAA LbL Films

2.1 Introduction

Polyethylene oxide (PEO) is one of the most versatile synthetic polymers available owing to its promise for drug delivery,[1] biomaterial applications, pH sensitive sensors, and solid polymer electrolytes.[2] Unfortunately, the common form of PEO is a semicrystalline solid which is water soluble; for this reason, PEO is often more useful in its cross-linked, hydrated form as a gel. This can present limitations for the creation of thin film systems requiring reasonable mechanical integrity, including certain functional biomaterials and solid electrolytes. Stable complexes can readily form between PEO and polyacids such as polyacrylic acid (PAA) or polymethacrylic acid (PMAA),[3-6] and these complexes have been studied for decades owing to the interest in their use for a number of the above named applications. Unfortunately, the precipitation of these hydrogen bonded complexes from solution results in films with poorly controlled geometries and morphologies. Attempts to process the complexes into usable forms generally results in either dissolution or degradation; for these reasons, these interesting complex structures have remained elusive in terms of real applications.

The layer-by-layer (LbL) assembly technique takes advantage of the same attractive forces that form complexes, but in a controlled manner that produces thin, conformal, films that can coat a variety of surfaces, Figure 2-1. Since their demonstration by Decher et al.[7, 8] in the early 1990s using oppositely charged polyions, layer-by-layer thin films have been investigated for biomaterials, drug delivery, photovoltaics, electrochromics, fuel cell membranes, and dry battery electrolytes.[9-18] These assemblies are formed by alternately exposing a substrate to positively and negatively charged polymers, or polymers with complementary hydrogen bond donors and acceptors. The wide range of applications and the large parameter space available to multilayer fabrication, including

polymer composition, pH and ionic strength, results in a broad variety of polymer nanocomposites.[16, 19, 20] Additionally, this process is not exclusive to polyelectrolytes, but may include any multiply charged species. Clay particles,[21] DNA, proteins, gold nanoparticles,[22] and carbon nanotubes[23] have all been incorporated in thin films using the LbL method.

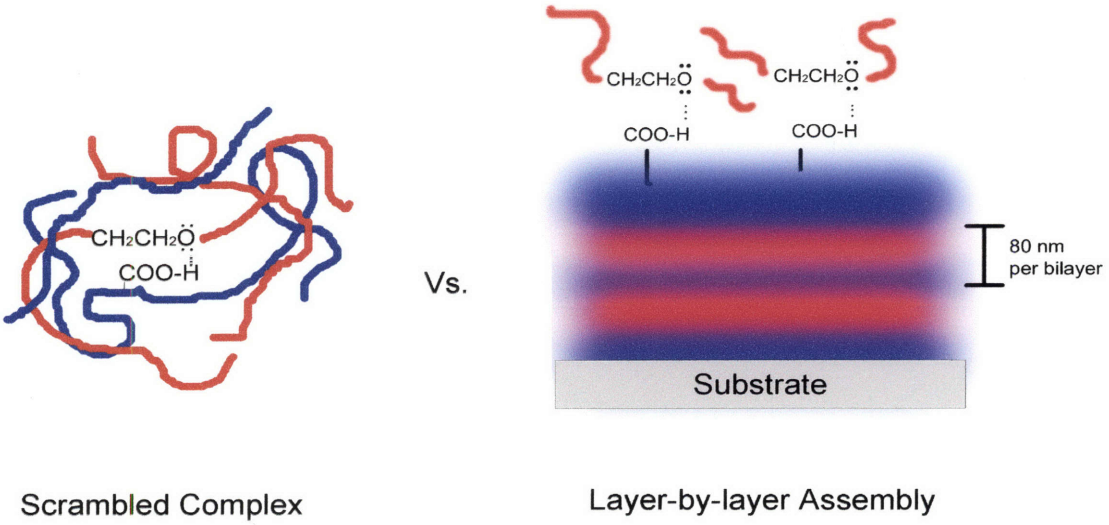

Figure 2-1. Scrambled complexes and layer-by-layer assemblies. Although both solution based polymer complexes (left) and LbL films (right) may be held together with hydrogen bonds (or electrostatic bonds), the LbL film exhibits nano-scale control while conformally coating the assembly substrate. The fuzzy layers illustrate the interdigitated nature of the two polymers, which can be extensive enough to create miscible blends.

The LbL film is usually tightly bound to its substrate (glass, ITO, or silicon), so that the substrate either plays an active role, or remains as a passive support in the end application. Previous methods to isolate the multilayer composite from the substrate have involved dissolving substrates,[27] sacrificial layers,[28] and even HF;[21] however, all these techniques expose the film to further treatment post-assembly that could potentially alter the original, pristine state of the assembly. Furthermore, the resulting area and mass of film is often too small to perform bulk-scale characterization. Without fully understanding the thermal and mechanical properties of an LbL film, it is not possible to establish fundamental concepts around their materials design, and the assembly cannot be fine tuned for real-world applications.

Whereas coulombic forces drive electrostatic LbL formation, hydrogen bonding can foster multilayer formation when a hydrogen bond donor and acceptor are used. Here, the characteristics and morphology of polyethylene oxide (PEO) and polyacrylic acid (PAA) LbL assemblies are examined. Hydrogen bonded LbL films were first demonstrated by Rubner et al.[24, 25] and later investigated by Sukhishvili et al.,[9, 26] who showed that hydrogen bonded assemblies can undergo a pH-induced deconstruction. DeLongchamp also investigated the PEO/PAA multilayer couple as a solid polymer electrolyte.[16]

Here, a novel approach to the solid state isolation of multilayered polymer nanocomposites containing PEO and PAA as elastomeric thin films is demonstrated. The ability to isolate large, uniform sheets of this material while maintaining mechanical integrity enables the use of characterization tools previously inaccessible to thin films confined to their substrate, including the direct measurement of bulk properties using Fourier transform infrared (FTIR) spectroscopy, mechanical tensile testing, differential scanning calorimetry (DSC), dynamic mechanical analysis (DMA), thermal gravimetric analysis (TGA), and impedance spectroscopy. We demonstrate the first direct measurement of a glass transition by DSC and DMA for these unique assemblies, as well as the first direct tensile test of a hydrogen bonded multilayer assembly. The non-aqueous removal and isolation of multilayer films allows for their direct incorporation in electrochemical devices, free-standing thin film drug delivery systems, and even electrochemical sensors. Remarkably, these H-bonded films act as physically cross-linked, fully miscible amorphous polymer blends with suppressed PEO crystallization and substantive mechanical cohesion in the solid state without the need for a chemical cross-link step.

2.2 Materials and Methods

Materials. Polyacrylic acid (M_w = 90,000, Polysciences, Inc.) and polyethylene oxide (M_w = 4,000,000, Polysciences, Inc.) were used as received. Solutions of 0.02 M concentration were made by dissolving the polymer in 18 MΩ Milli-Q water, and then pH-adjusted with HCl and NaOH. Hydrophobic substrates (either polypropylene from VWR or PTFE from McMaster Carr Co.) were sonicated in Milli-Q water for 30 minutes prior to film deposition.

Film Assembly and Isolation. Films were fabricated using a modified Carl Zeiss DS50 programmable slide stainer. Substrates were first exposed to PEO for 10 minutes, then three baths of Milli-Q 18 MΩ water for 4 minutes total. Next, the substrates were exposed to PAA for 10 minutes, then three baths of Milli-Q 18 MΩ water for 4 minutes total. The cycle was repeated for 100 bilayers, unless otherwise noted, to yield a film eight microns thick. All baths were kept at pH 2.25, 2.5, 2.75, or 3.0 to prevent ionization of PAA. Following assembly, the films were dried in a vacuum chamber for one hour, peeled away from the substrate with tweezers, and then stored in an MBraun glove box containing argon at < 1 ppm water.

Film Characterization. Samples were characterized using tensile testing on a Zwick/Roell Z010 with a 10 N load cell in ambient conditions. DSC was performed in a Q1000 instrument by TA Instruments scanning from -90 to 130 °C at 10 °C/min in a nitrogen purge, with the second scan retained. With a nitrogen purge in TGA, samples were heated from room temperature to 700 °C in a TA Instruments Q50 at a rate of 10 °C/min. A Tencor P-10 surface profilometer was used for thickness measurements. DMA using a thin film clamp was performed at 10 Hz ramping from -100 to 100 °C at a rate of 3 °C/ minute on a TA Instruments Q800 in a nitrogen purge.

AC Impedance. Thirty bilayers of PEO and PAA were constructed on ITO patterned slides as described elsewhere.[16] AC impedance was conducted from 1E7 to 10 Hz with 10 and 100 mV amplitude on a Solartron 1260 Impedance Analyzer. Analysis was conducted as described elsewhere.[15, 16]

pH-Induced Deconstruction. Film deconstruction was observed using profilometry of PEO/PAA films assembled on silicon substrates cleaned with piranha for one minute prior to construction. CAUTION! Piranha is very corrosive and proper safety should be practiced. Thirty bilayers of PEO/PAA LbL films were constructed at pH 2.5 on silicon as indicated above. To induce cross-linkage, a fraction of samples were heated at 105 °C overnight. FTIR after heat treatment confirmed the formation of anhydride cross-links. Initial film thickness was measured, and then the films were exposed to pH 7.4 phosphate buffer solution (OmniPur). After a period of time, the samples were removed and exposed to pH 2.5 Milli-Q water to halt deconstruction. After drying with high velocity

air and then vacuum treatment over night, the sample thickness was measured. The ratio of the sample thickness after PBS exposure to thickness before PBS exposure was taken as a measure of deconstruction.

Water Contact Angle Measurement. A lift-off film of PEO/PAA at pH 2.5 was isolated and used for measurement. The film was constructed such that the top-most layer (or last layer) was polyacrylic acid and the bottom-most layer (or first layer) was polyethylene oxide. The advancing and receding contact angle were measured on the top and bottom of the film in different areas. Because the film absorbs the microliter drop of water in about 30 seconds, all measurements were performed in a quick and timely manner.

2.3 Surface Interactions and Free-Standing Films

The key difference in obtaining free-standing films in the dry solid state as opposed to film removal with an aqueous method lies in the choice of substrate. Whereas previously mentioned methods use glass or silicon platforms, we employ neutral, hydrophobic surfaces such as Teflon® and polypropylene with water contact angles of 108 ° and 94 °, respectively. First, aqueous polyethylene oxide (MW = 4,000,000 g/mol) is uniformly adsorbed onto the Teflon® surface by Van der Waals interactions. Subsequent exposure to polyacrylic acid (MW = 90,000 g/mol), a hydrogen bond donor, results in a layer of PAA hydrogen bonded to the PEO. As these steps are repeated, the two polymers are deposited as highly interdigitated layers joined by hydrogen bonds. The growth of the polymer layers was shown to be exponential, and the averaged thickness per polymer bilayer was found to be 80 nm for a 100 layer pair film. A 100 bilayer film can be peeled away from the substrate with tweezers, resulting in a pin-hole free, continuous film of approximately 8 microns thickness and an RMS roughness of 0.4 microns as determined by profilometry. Electrostatically assembled layers of the weak polyelectrolytes, polyethylene imine and polyacrylic acid, were also isolated in this manner; structure and properties of these electrostatic films will be reported in a future work.

Because Van der Waals forces were the only interactions between the film and the neutral substrate, isolation of the free standing film was easily and quickly performed without the aid of water, salt, or acids. The isolated hydrogen bonded layers were transparent, smooth to the touch, and exhibited elastomeric properties during handling,

Figure 2-2. At this time, the thinnest continuous cohesive structure obtained by this method is a 20 bilayer assembly of PEO and PAA approximately 2 microns thick with a surface area of 4 cm^2, the total area of the substrate on which it was assembled. Thinner films can be lifted off, but tear into smaller fragments during isolation.

Figure 2-2: Isolated layer-by-layer PEO/PAA assembled at pH 2.5. Following assembly, films were gently dried and peeled away. Both films shown, isolated from a Teflon substrate, were clear and flexible. These films are 100 layer pairs and 8 micrometers in thickness.

FTIR of the free-standing film indicated the presence of both polyethylene oxide[29] and polyacrylic acid,[26] not shown. The carboxylic acid was in its protonated state (1708 cm^{-1}) and the acid ionization peak (1570 cm^{-1}) was absent. Exposure to the dry nitrogen purge in the FTIR dehydrated a small fraction of the PAA to form anhydride linkages (1804 cm^{-1})[25].

2.4 DSC

Differential scanning calorimetry of a PEO/PAA multilayer assembly in nitrogen shown in Figure 2-3a and Figure 2-3b illustrates that the melting peak of PEO at 65° C is completely suppressed. The lack of a melting peak in both the multilayer film and its analogous complex indicates that when hydrogen bonding is introduced using PAA, *crystallization of PEO can be fully prevented,* even when the polymer has a high

molecular weight. Additionally, a single glass transition (52° C) was detected between those of pure PEO (-56° C) and PAA (99° C). The thermal properties and the transparency of the multilayer assemblies indicate that the hydrogen bonded multilayer films are a true, fully miscible nano-assembled polymer blend. The Fox equation,[30] a mixing rule for polymer blends, was used to estimate film composition. This equation is most accurate for LbL films that are fully dried, because trace water lowers the observed glass transition. The DSC conditions were maintained under constant nitrogen flow, and the first and second cycles were measured. A glass transition temperature of 52° C gave a composition of 20 wt% PEO and 80 wt% PAA. Complexes of PEO and PAA formed directly from solution via precipitation were used as a control for the determination of thermal properties. Properties were similar to multilayer assemblies made under analogous experimental conditions, further evidence of the ability of layer-by-layer to create nanoscale blends of two polymers. First scans of both complexes and LbL assemblies exhibited an endothermic peak related to the release of bound water, suggesting the PEO/PAA film's hygroscopic nature; this peak was not present in additional cycles. This DSC study demonstrates, to the best of the authors' knowledge, the first thermal analysis evaluation of an LbL film; ultimately, estimating the glass transition and composition by DSC of an LbL film is a new, but familiar, method now available to the LbL community with the introduction of a simple lift-off approach to isolating free-standing films.

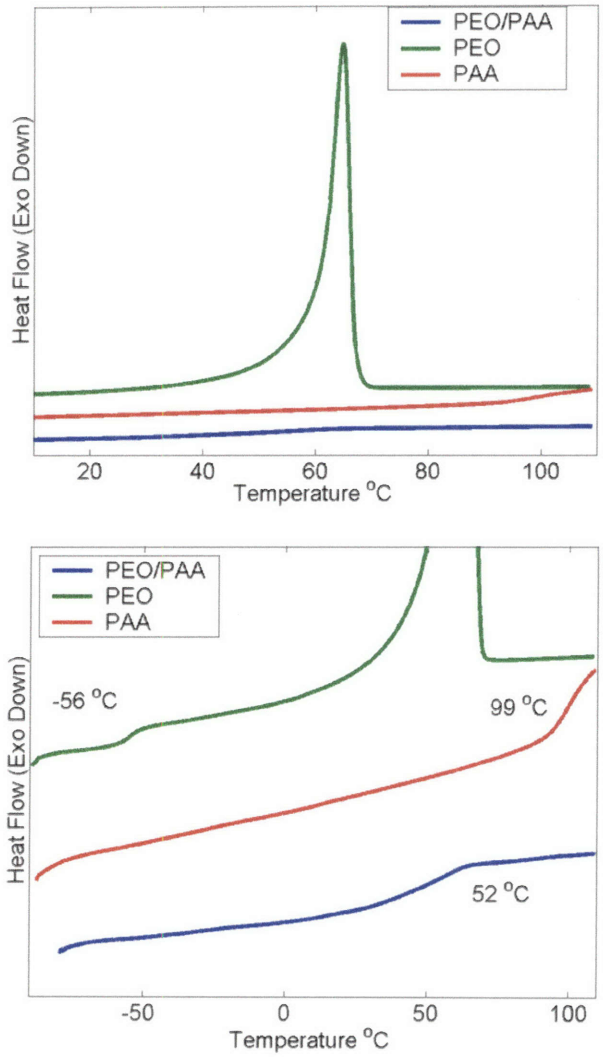

Figure 2-3. (a) Differential scanning calorimetry of PEO/PAA assemblies compared to pure PEO and PAA, second scan shown. (b) A close up of the glass transition regions. The LbL film, assembled at pH 2.25, exhibits a single T_g between that of its pure components. Also, the melting peak of pure PEO (65 °C) is not present in the LbL film. LbL films were 100 layer pairs, 8 μm thick.

2.5 TGA

Weight loss detected by thermal gravimetric analysis (TGA) confirmed the composition of the layered assembly determined by the Fox equation. To minimize moisture and oxygen exposure, the samples were rigorously dried in a vacuum overnight and stored in < 1ppm argon for days before testing, and the experiment was conducted under nitrogen.

For hydrogen bonded multilayers assembled at pH 2.25, two distinct weight loss regions were measured (Figure 2-4). Upon heating from room temperature, the sample first exhibited small losses (2 wt%) attributed to water. The first significant decomposition region, from 175 to 300 °C, was attributed to partial PAA decomposition.[31] The remainder of the sample, believed to be PEO and PAA, degraded above 375 °C; this is consistent with pure PAA, which rapidly decomposes at above 400 °C.[31] Data from TGA demonstrated that the multilayer assembly composition was 22 wt% PEO and 78 wt% PAA from analysis of the curve's first derivative. These values closely match results stated above from thermal analysis, where a single measured T_g of 52°C gave compositions of 20 wt% PEO and 80 wt% PAA (or 30 mol% PEO and 70 mol% PAA by monomer unit). While previous investigations[3, 5] indicated that precipitated H-bonded complexes form in equimolar ratios, it was found the PAA content was double that of PEO in both precipitated complexes and multilayer assemblies. This discrepancy is explained by the internal hydrogen bonding of polyacrylic acid in the form of acid dimerization[32] that takes place during adsorption. This mechanism, whether occurring by intra- or interchain means, may have prevented a significant quantity of carboxylic acid groups from participating in hydrogen bonding with PEO. The carboxylic acid structure is also confirmed by FTIR where the C=O peak at 1708 cm^{-1} is indicative of intra- or intermolecular dimers.[33, 34]

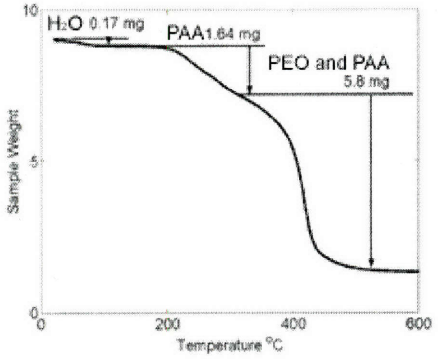

Figure 2-4. TGA of 100 layer pairs of PEO/PAA assembled at pH 2.5 conducted under a nitrogen purge. PAA has two decomposition events and PEO has one. Composition may be estimated from the mathematical addition of the pure component responses.

2.6 DMA

Besides thermally characterizing PEO/PAA LbL films with DSC and TGA, the isolation of these thin films allows us dynamic mechanical analysis experimentation. A thin, dry film of PEO/PAA was subjected to an oscillating tensile force in a nitrogen purge. Tan delta, the ratio of out-of-phase response to in-phase response, increases significantly at thermal relaxations like glass transitions or second order relaxations such as the rotation or vibrations of side-groups.

Figure 2-5 illustrates a typical PEO/PAA DMA curve. This experiment was performed in a dry nitrogen purge, and was allowed to equilibrate with the dry environment. At low temperatures, the glassy storage modulus plateaus at 3 GPa and drops to 2 GPa with increasing temperature before failure via necking around 70° C. The tan delta curve shows a peak at -37° C and the onset of failure at 47° C in the form of a much greater peak (off scale of plot). The former peak is attributed to the Beta relaxation of side chain movements of PAA in its hydrogen bonded state, and the latter event relates to the glass transition of the LbL nano-blend.

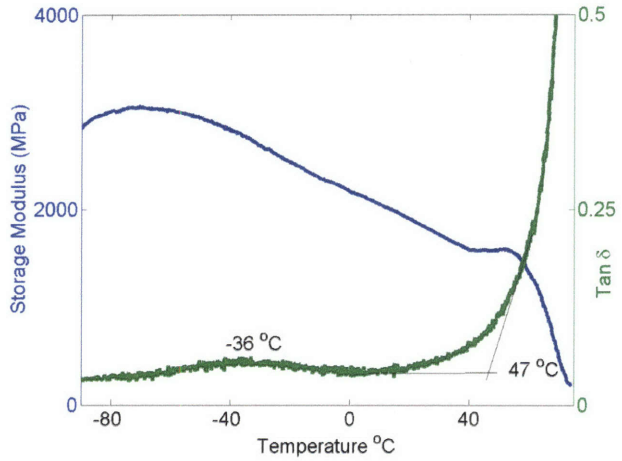

Figure 2-5. DMA at 0 % humidity of 100 layer pairs of PEO/PAA assembled at pH 2.25. The left-most tan δ peak, -36 °C, corresponds to a secondary transition while failure at 47 °C occurs near the glass transition of the film. The storage modulus is ~ 3 GPa until failure.

2.7 Tensile Testing

Because multilayer thin films have been generally inseparable from their assembly substrate, past measurements of mechanical properties were performed using indirect methods like nanoindentation[22, 35-37] and microcapsule swelling,[38, 39] which probe structures on a nanometer to micron scale, often when immersed in aqueous solutions. With sheets of multilayers now isolated in the solid state, bulk mechanical properties can be tested via standard tensile testing without exposing the samples to an aqueous environment. The behavior of the multilayers under typical ambient conditions is of particular interest for a number of applications. Tensile testing was conducted in ambient conditions (50 % humidity), where water absorbed from the air may plasticize the matrix. Plasticization may lower the glass transition temperature, enhance the rubbery character of the film and lower the observed modulus via plasticization. Thin sheets of multilayer film (8 μm) were isolated from a polypropylene substrate, trimmed with scissors (8 mm x 6 mm), and submitted to uniaxial tension in ambient conditions. A stress-strain curve typical for these films at ambient conditions is shown in Figure 2-6; the curve is similar to that of a standard rubbery material. The calculated tensile modulus, ultimate strain and ultimate stress were 6.7 MPa, 360%, and 2 MPa, respectively. At small strains(0-4%), the initial modulus is directly impacted by molecular entanglements and hydrogen bond cross-links. A rubbery plateau exists as the loops between cross-links unwind and stretch, from 4% strain until about 300%. Finally, strain hardening was observed at higher strains until break, which may indicate the formation of ordered domains at large extensions (i.e. strain induced crystallization) or the onset of the ultimate extensibility of the polymer chains. At break, the sample fractured, and the individual pieces retracted to their original dimensions in seconds. Differential scanning calorimetry and optical microscopy of the fractured sample confirmed the absence of any crystallites after tensile testing, similar to Flory's treatment of natural rubber.[40] The observed elastic, or rubbery, modulus fluctuated from 4 to 9 MPa depending on the humidity of the testing environment. It should be noted that this modulus is the rubbery modulus, corresponding to the rubbery plateau region that exists in the plasticized PEO/PAA matrix between the glass transition and effective hydrogen bond deconstruction or "melting point"; as expected, this modulus

is orders of magnitude lower than the modulus measured under dry conditions, which corresponds to the polymer in its glassy state.

Water's influence can be observed both in DMA and tensile testing. For example, DMA on a dried film gave a T_g of 47 °C and a glassy modulus of 2 GPa at room temperature, whereas DMA of a film at ambient humidity gave a T_g of 17 °C and a rubbery tensile modulus of 74 MPa at 20 °C (not shown). DMA of the humid film would exhibit a rubbery plateau at slightly higher temperatures, most likely at 4 to 9 MPa as reflected in tensile testing, but beyond 20 °C the material was too soft for accurate measurement. Similarly, the observed modulus from tensile testing is a direct result of plasticization from water absorption. Once water exists in the film, the T_g is lowered and the mechanical properties reflect those found in the rubbery regime as opposed to the glassy response observed in dry DMA.

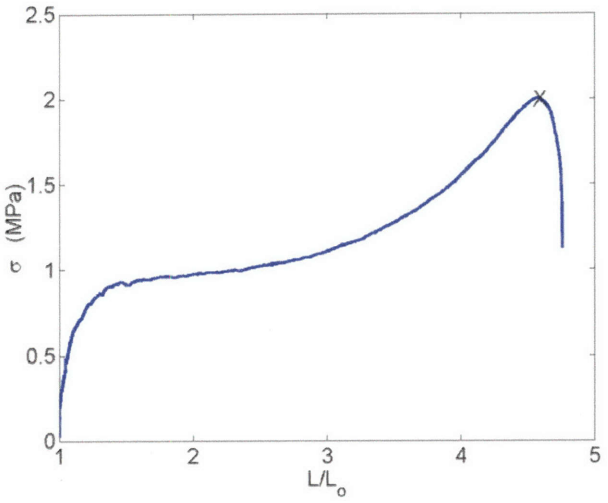

Figure 2-6. Tensile testing of 100 layer pairs PEO/PAA at pH 2.5 in ambient conditions. In ambient humidity, the film uptakes water and becomes plasticized. The shape of the curve mimics that of an elastomer, where extension at break was greater than 300%

Previous studies of the Young's Modulus in multilayer films focused upon electrostatically bound layers, giving modulus values ranging from 1 MPa to 10 GPa, depending on component materials and measurement method,[21, 22, 35-39] with fully hydrated materials often exhibiting a lower modulus. Our studies indicate that hydrogen bonded multilayer assemblies are generally less stiff than their electrostatically assembled multilayer counterparts, especially when both are compared under hydrated conditions.

This difference in modulus is explained in part by the comparative energies of hydrogen and electrostatic bonding and the differences in the effective "cross-link" density in these films. The density of ionic bonds found in the polyion complexed films is generally greater than the density of hydrogen bond complexed groups in PEO/PAA due to much lower driving forces between hydrogen bond functional groups. A third important difference is the relatively low glass transition temperature of PEO, which is expected to yield rubbery behavior in a chemical or physical network. A final, but significant, factor for the mechanical properties of the PEO/PAA assembly is the hygroscopic nature of PEO. Absorbed water, which acts as a plasticizer, enhances mobility in the thin film by lowering the glass transition, resulting in a higher extensibility and lower modulus at room temperature. Consequently, the mechanical properties of the PEO/PAA thin film as a function of humidity is a subject of future work. Conversely, in a dry argon glove box with < 1 ppm water, the PEO/PAA films still bend and flex, but they tear at much lower strains under uniaxial tension than their humid counterparts. Schlenoff et al. has extensively studied the effect of water content in electrostatic multilayers, finding that water comprises 10 to 20 percent of the film's mass, all of which can be removed with heat.[41]

Knowledge of the rubber tensile modulus (~ 4 to 9 MPa at 25 °C and 50% RH) and overall composition allows the crude estimation of the average effective molecular weight between cross-links, M_c, and the cross-link density of this hydrogen bonded network. Assuming constant volume, uniaxial tension, and Gaussian distribution, the hydrogen bonded multilayer was treated as an elastomer as discussed in Flory, with $\sigma_n = \rho RT/ M_c(\alpha - 1/\alpha^2)$, where σ_n and α represent the stress and strain, respectively.[40] At small extensions, the tensile modulus was modeled as the coefficient, $\rho RT/ M_c$. Stress-strain measurements indicated an average molecular weight between cross-links ranging from 300 to 600 g/mol. If each PAA loop had twice as many monomers as a PEO loop, as indicated from TGA-based compositional estimates, then roughly 16 to 31% of PEO monomers and 8 to 16% of PAA monomers participate in hydrogen bonding between the ether and carboxylic acid groups. Because of fluctuations from water content, humidity, and a breakdown of the Gaussian approximation, the cross-link density and molecular weight between cross-links are presented only as rough sketches of the true system.

2.8 Discussion of the Effect of Humidity upon Modulus

Mechanical tests yield data representing different regions of the ideal modulus-temperature curve depending on the water content or temperature; for instance the modulus of a dry PEO/PAA film at 25 °C is nearly 1000 times greater than the modulus of the same film allowed to equilibrate with ambient humidity. To clarify whether the sample in question is dry and glassy *or* plasticized and rubbery, the modulus is referred to as the glassy or rubbery modulus depending on the state of the testing conditions. In the simplest case let us examine the effect of temperature and later, the effect of humidity.

The *ideal* modulus-temperature curve of a high molecular weight polymer would appear sigmoidal. At a temperature below the T_g, a glassy modulus (10^9 Pa) was observed, where the modulus decreased only slightly with increasing temperature. Around the T_g, the modulus is expected to a secondary, or rubbery, plateau (10^6 Pa); however this second plateau was not observed owing to limitations of the instrument.

Figure 2-5 shows a glassy region and part of the precipitous drop leading towards a rubbery plateau. At this point, the material is so soft that the DMA is unable to accurately represent the mechanical properties of the system and is unable to record the rubbery plateau of a dry film. At 25 °C, when the dry LbL film is unplasticized, the film is below the glass transition (47 °C) and gives a glassy modulus of ~2 GPa.

If water is allowed to plasticize the LbL film, the resulting DMA curve would retain the same shape, but the glass transition would be depressed. DMA of a film equilibrated with ambient humidity, ~50%, was performed (not shown). Below the glass transition, the film exhibits a glassy modulus approaching 1 GPa, but beyond the T_g (17 °C) the modulus drops rapidly until the DMA can no longer record such a soft modulus. At 20 °C, the modulus, which lies between the glassy region and rubbery plateau, is 74 MPa.

The tensile tests performed at ambient conditions serve to elucidate the performance of the LbL thin film above the glass transition. At 25 °C and equilibrated with the humid environment, the film behaves as a soft elastomer with a tensile modulus of 4 to 9 MPa. In these conditions, the modulus observed represents the rubbery regime where there is adequate plasticization to depress the T_g (17 °C) below room temperature.

In summary, ambient humidity can lower the dry T_g from 47 °C to a plasticized T_g of 17 °C. The sensitive nature of the T_g can lead to dramatically differing mechanical properties under varying humidity.

2.9 Preliminary Assessment of pH-Dependency

To understand the role of assembly solution pH as a control parameter, hydrogen bonded LbL assemblies of pH 2.25, 2.5, 2.75 and 3.0 were investigated using DSC (Figure 2-7) and DMA (Figure 2-8). DSC indicated that increasing assembly pH results in a lower T_g. Accordingly, a lower glass transition indicates the enrichment of PEO within the film. The T_g-pH trend was confirmed using TGA and DMA, as summarized in Table 1. In DMA, the onset of the glass transition clearly decreases with increasing assembly pH, but the Beta relaxation near -36 °C remains invariant under different pH values.

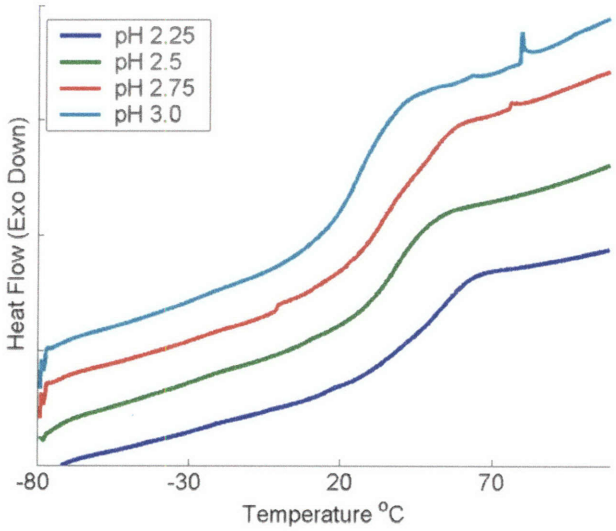

Figure 2-7. Second-scan DSC heating curves of 100 layer pairs of PEO/PAA assembled at different pHs (2.25 to 3.00). As assembly pH increases from 2.25 to 3.00, the glass transition of the constructed multilayer decreases from 52 to 25 °C.

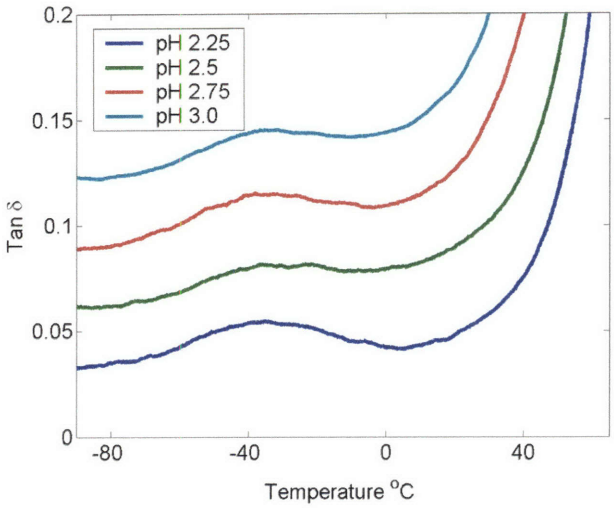

Figure 2-8. DMA of 100 layer pairs of PEO/PAA films constructed at varying pH. The onset of failure, associated with the glass transition, decreases with increasing pH. Also, the secondary relaxation (-36 °C) appears constant for all assembly pH

Table 2-1. A comparison of the glass transition temperatures measured under dry nitrogen conditions (in °C) of PEO/PAA films from DMA and DSC at varying assembly pH.

pH	DMA T_g	DSC T_g
2.25	49	52
2.5	45	38
2.75	34	34
3.0	28	25

Examining pH as a control parameter allows us to elucidate the underlying factors that determine composition and morphology. In more acidic conditions, like pH 2.25, PAA hydrogen bonds with itself as stated previously. As the solution pH increases, PAA is less likely to hydrogen bond with itself owing to small amounts of charge repulsion, so the polymer adsorbs in thinner layers with less relative amounts of PAA to PEO. As a limiting case, the film could approach a stoichiometric composition with a glass

transition of 20.4° C at higher pH values. However, to achieve this limiting composition, the pH approaches a "modulation window" (pH > 3) where the LbL construction is electrostatically hindered by the ionization of PAA and resulting electrostatic repulsion; ultimately, at pH 3.6 and above the LbL film is unable to assemble.[16, 26] At assembly pH 3.0, the limiting case is approached for which DSC demonstrates a glass transition of 25.3° C, giving a composition of 47 mol % PEO, while maintaining mechanically robust films.

2.10 pH-Stimulated Deconstruction

Hydrogen bonded layer-by-layer films are of interest as pH-responsive deconstructing thin films. A responsive film is desirable for applications like therapeutic patches, coatings, and drug delivery. Controlling the rate of deconstruction, which may be altered by inducing covalent cross-linkages via heat treatment, is key for tailoring this hydrogen bonded system.

Sukhishvili et al. demonstrated the release of dye from multilayer capsules via the pH induced deconstruction of PEO/PAA LbL films.[26] Above a critical pH, polyacrylic acid will ionize, thus eliminating its hydrogen bond with PEO. Depending on the pH, the deconstruction can take place in a matter of seconds to days. To mimic the deconstruction of PEO/PAA nanocomposites at physiological conditions, thin strips of PEO/PAA nanocomposites on Si were exposed to a PBS solution to observe the kinetics of deconstruction. One set of multilayers were heat treated to form anhydride cross-links, while another set was left untreated. While exposed to pH 7.4 buffer solution, the anhydride cross-linked film persisted for nearly four times as long as an untreated PEO/PAA assembly before delamination from the silicon substrate, Figure 2-9. Under these conditions, the cross-linked films swells and then persists for hours in its swollen state as opposed to the uncross-linked film which deconstructs in a matter of minutes. Potentially, films cross-linked under higher temperatures for longer durations might deconstruct over even longer periods of time.

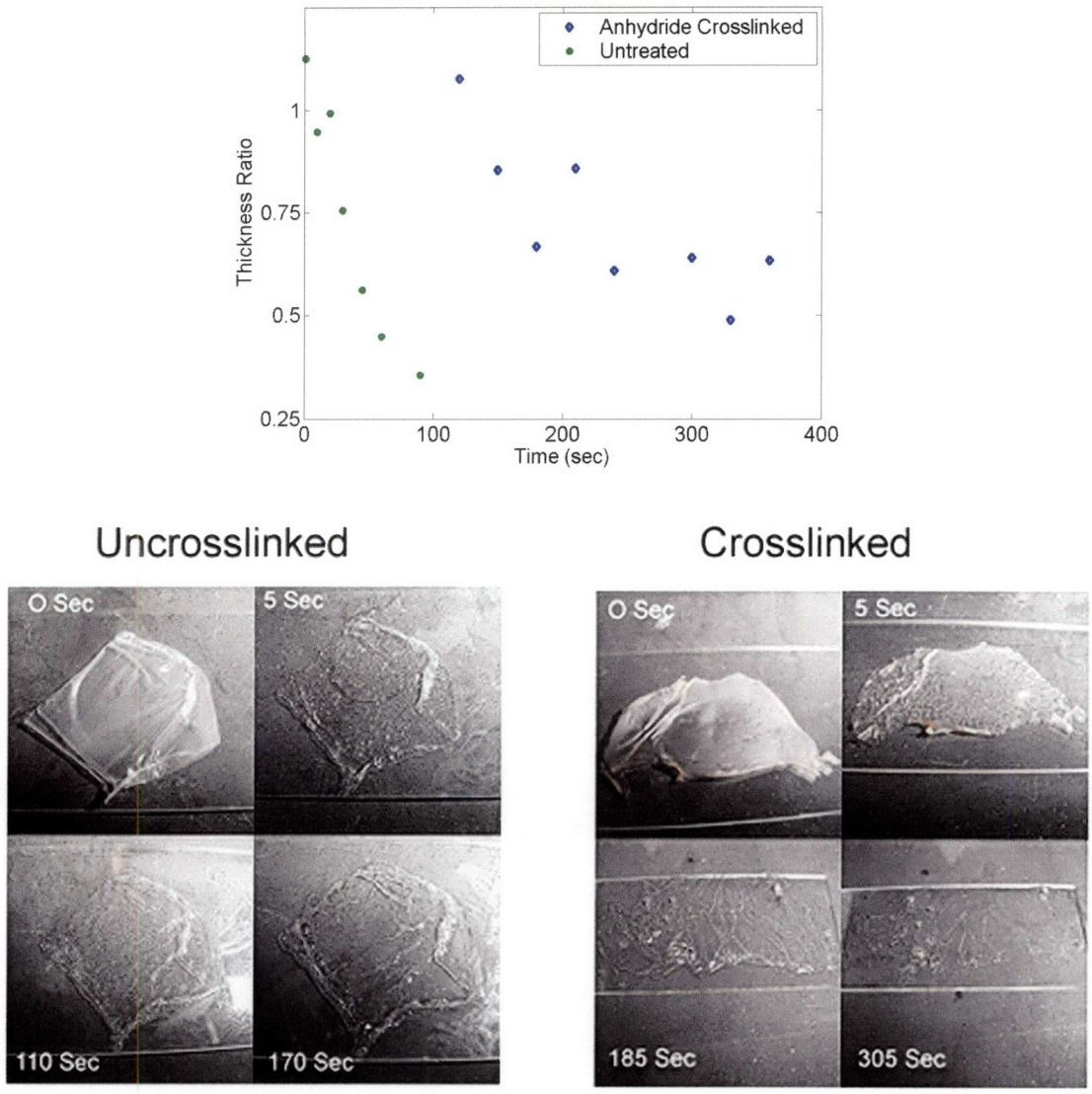

Figure 2-9. A representative uncross-linked and anhydride cross-linked (105 °C overnight) PEO/PAA film assembled at pH 2.5 deconstructs with time as they are exposed to phosphate buffer solution. (Top) In PBS, the anhydride cross-linked PEO/PAA assembly deconstructs slower than the untreated analog. (Bottom) While the uncross-linked film (left) eventually dissolves away, the cross-linked film (right) persists in a swollen gel-like state.

In addition to drug delivery, the isolation of LbL films allows for the design of asymmetric functionalized surfaces. One side of the assembly might promote wound healing while the other side protects the wound from the external environment. To

demonstrate the asymmetric properties of a LbL assembly, the water contact angle of each side was measured. The initial bilayer surface of PEO and the final surface of PAA showed receding water contact angles of 97° and 75°, respectively. In combination, we envision future hydrogen bonded layer by layer assemblies to comprise asymmetrically functionalized free-standing films that controllably deconstruct while delivering therapeutic agents or other molecules of interest to the surface of contact.

2.11 Conclusion

Hydrogen bonded LbL assemblies have also been shown to conduct ions including protons and lithium ions, but in past and ongoing work the multilayer films are usually constructed on active substrates such as ITO or porous membranes. For applications such as fuel cells or batteries, LbL films can now be peeled, lifted off and trimmed for specific dimensions. The untreated PEO/PAA assembly performs exceedingly well in its hydrated form as a fuel cell membrane, showing proton conductivities reaching 10^{-4} S cm^{-1}.[16] Another factor of note is that PEO crystallization, a significant obstacle to ion mobility, was completely suppressed as shown in DSC. Future work will entail tailoring the PEO composition through construction pH and measuring the subsequent ionic conductivity.

Novel solid state hydrogen bonded assemblies were created using a layer-by-layer method which allowed the incorporation of PAA and PEO on the nanometer length scale. Remarkably, these hydrogen bonded nano-assemblies could be isolated as substantive, tough elastomeric thin films using a simple peel-off procedure from a low energy surface. The new technique is applicable to not just hydrogen bonded LbL assemblies, but electrostatic assemblies and those containing smaller molecules like clay or dendrimers. By isolating these thin films as continuous sheets on the surface, it was possible to study the bulk structure and properties in PEO/PAA multilayer assemblies, and directly observe their properties as an elastomeric blend. The structures were transparent, exhibited no melting peaks, and revealed one glass transition temperature rather than two. Importantly, the result of assembling these semicrystalline polymers was a fully amorphous, true polymer blend. The amorphous nature induced by the nano-scale blending of PEO with PAA in a LbL assembly mimics the scrambled complex first proposed by Michaels[42] and Decher[8], behaving similarly to that of its analogous hydrogen bonded complex.

The low glass transition of these nanoassembly networks led to rubbery behavior at room temperature; these systems exhibited thermal stability up to the point of degradation of the polymer components at high temperature. In basic aqueous solutions, the rate of film deconstruction can be controlled with anhydride cross-linking. In ongoing work, the tunable qualities of layer-by-layer assembly will lead us to tailor new PEO/PAA films for improved ion conduction, biomaterials, pH-sensitive sensors, and drug delivery by controlling the degree of inter- and intramolecular hydrogen bonding while maintaining the amorphous, elastomeric quality of the structure. Additionally, the influence of humidity and water content upon the thermal and mechanical properties of LbL films will be investigated in future work. In the more general sense, the solid state isolation of these films from hydrophobic surfaces opens a new door for the direct incorporation and characterization of multilayer assemblies for fuel cells, micropower devices, gas separation membranes, biomaterials substrates, drug delivery devices and pH sensitive sensors.

2.12 References

1. Park, T. G.; Cohen, S.; Langer, R. *Macromolecules* **1992,** 25, (1), 116-122.
2. Gray, F. M.; Royal Society of Chemistry (Great Britain), *Polymer electrolytes*. Royal Society of Chemistry: Cambridge, 1997; p xii, 175 p.
3. Ikawa, T.; Abe, K.; Honda, K.; Tsuchida, E. *Journal of Polymer Science* **1975,** 13, (7), 1505-14.
4. Khutoryanskiy, V. V.; Dubolazov, A. V.; Nurkeeva, Z. S.; Mun, G. A. *Langmuir* **2004,** 20, (9), 3785-3790.
5. Bailey, F. E.; Lundberg, R. D.; Callard, R. W. *Journal of Polymer Science: Part A* **1964,** 2, (2), 845-51.
6. Jeon, S. H.; Ree, T. *Journal of Polymer Science: Part A* **1988,** 26, (5), 1419-28.
7. Decher, G.; Hong, J. *Thin Solid Films* **1992,** 210, (1-2), 831.
8. Decher, G. *Science* **1997,** 277, 1232.
9. Sukhishvili, S.; Granick, S. *Journal of American Chemical Society* **2000,** 122, (39), 9550-1.
10. Hammond, P. T. *Colloid and Interface Science* **2000,** 4, 430-442.
11. Delongchamp, D. M.; Hammond, P. T. *Chemistry of Materials* **2003,** 15, (5), 1165.
12. Wood, K.; Boedicker, J.; Lynn, D. M.; Hammond, P. T. *Langmuir* **2005,** 21, (4), 1603-1609.
13. Berg, M.; Yang, S. Y.; Hammond, P. T.; Rubner, M. F. *Langmuir* **2004,** 20, (4), 1362-1368.
14. Zhai, L.; Cebeci, F.; Cohen, R.; Rubner, M. F. *Nano Letters* **2004,** 4, (7), 1349-1353.
15. Lowman, G.; Tokuhisa, H.; Lutkenhaus, J. L.; Hammond, P. T. *Langmuir* **2004,** 20, 9791.
16. Delongchamp, D. M.; Hammond, P. T. *Langmuir* **2004,** 20, (13), 5403-11.
17. DeLongchamp, D. M.; Hammond, P. T. *Chemistry of Materials* **2003,** 15, (5), 1165-1173.
18. Hammond, P. T. *Advanced Materials* **2004,** 16, (15), 1271-1293.
19. Dubas, S.; Schlenoff, J. *Macromolecules* **1999,** 32, (24), 8153-8160.
20. Shiratori, S.; Rubner, M. F. *Macromolecules* **2000,** 33, (11), 4213.
21. Tang, Z.; Kotov, N. A.; Magonov, S.; Ozturk, B. *Nature Materials* **2003,** 2, 413.
22. Jiang, C.; Markutsya, S.; Pikus, Y.; Tsukruk, V. V. *Nature Materials* **2004,** 3, 721-728.
23. Mamedov, A. A.; Kotov, N. A.; Prato, M.; Guldi, D. M.; Wicksted, J. P.; Hirsch, A. *Nature Materials* **2002,** 1, 190-194.
24. Mamedov, A. A.; Kotov, N. A. *Langmuir* **2000,** 16, 5530.
25. Dubas, S. T.; Farhat, T. R.; Schlenoff, J. B. *Journal of American Chemical Society* **2001,** 123, (22), 5368.
26. Stockton, W.; Rubner, M. F. *Macromolecules* **1997,** 30, 2717.
27. Yang, S. Y.; Rubner, M. F. *Journal of American Chemical Society* **2002,** 124, (10), 2100-2101.

28. Sukhishvili, S.; Granick, S. *Macromolecules* **2002,** 35, (1), 301.
29. Kimura, N.; Umemura, J.; Hayashi, S. *Journal of Colloid and Interface Science* **1996,** 182, (2), 356-364.
30. Painter, P. C.; Coleman, M. M., *Fundamentals of polymer science : an introductory text*. 2nd ed.; Technomic Pub. Co.: Lancaster, Pa., 1997; p xv, 478 p.
31. *Polymers: A Property Database*. CRC Press, LLC: 2004; Vol. 2004.
32. Ege, S., *Organic Chemistry*. 3rd ed.; D.C. heath and Company: Lexington, 1994.
33. Lee, J. Y.; Painter, P. C.; Coleman, M. M. *Macromolecules* **1988,** 21, (2), 346-354.
34. Lu, X.; Weiss, R. A. *Macromolecules* **1995,** 28, (9), 3022-9.
35. Mermut, O.; Lefebvre, J.; Gray, D. G.; Barret, C. J. *Macromolecules* **2003**.
36. Pavoor, P.; Bellare, A.; Strom, A.; Yang, D.; Cohen, R. *Macromolecules* **2004,** 37, (13), 4865-4871.
37. Richert, L.; Engler, A.; Discher, D.; Picart, C. *Biomacromolecules* **2004,** 5, (5), 1908-1916.
38. Vinogradova, O. I.; Andrienko, D.; Lulevich, V. V.; Nordschild, S.; Sukhorukov, G. B. *Macromolecules* **2003,** 37, (3), 1113.
39. Gao, C.; Leporatti, S.; Moya, S.; Donath, E.; Mohwald, H. *Langmuir* **2001,** 17, (11), 3491-3495.
40. Flory, P. J., *Principles of Polymer Chemistry*. Cornell University Press: Ithaca, 1953.
41. Farhat, T.; Yassin, G.; Dubas, S.; Schlenoff, J. *Langmuir* **1999,** 15, (20), 6621.
42. Michaels, A. S. *Industrial and Engineering Chemistry* **1965,** 57, (10), 32.

Chapter 3 : Hydrogen-bonding Interactions, Thermal Properties and Ion Transport within Poly(ethylene oxide)/Poly(acrylic acid) Layer-by-Layer Assemblies

Portions of this chapter are reprinted from Lutkenhaus, J. L.; McEnnis, K.; Hammond, P. T. *In Preparation.*

3.1 Introduction.

Hydrogen bonding between two macromolecular species gives rise to a breadth of interesting super-structures observed in nature, interpolymer complexes,[1-3] and layer-by-layer assemblies.[4-6] While hydrogen bonding interactions between a proton-accepting and a proton-donating monomer may be small (~2-10 kcal/mol), the sum of these interactions, from the association of polymeric species, is sufficient to produce a stable complex.[7] A simple and easy means of creating stable hydrogen-bonded thin films is the layer-by-layer (LbL) assembly technique, where a substrate (e.g. silicon, Teflon®, ITO) is alternately exposed to aqueous solutions of proton –donating and –accepting polymers.[4-6] In general, these thin films appear to behave as miscible blends, where each "layer" of deposition produces an interdigitated morphology,[8-10] yielding properties similar to solution-cast complexes.

Hydrogen-bonded LbL multilayers of proton-donor poly(acrylic acid) (PAA) or poly(methyacrylic acid) (PMAA) and a complementary proton-acceptor poly(ethylene oxide) (PEO) have been recently explored as solid polymer electrolytes, drug delivery vehicles and responsive capsules.[11-14] To create stable hydrogen-bonded films (20-90 nm thickness per layer pair), an acidic assembly pH is required to suppress the ionization of the polycarboxylic acid, and above a critical pH, film assembly is unfavorable owing to electrostatic repulsion (pH = 3.6 for PEO/PAA and pH = 4.5 for PEO/PMAA).[11] Conversely, a stable LbL film may be "erased" when solution pH is greater than critical pH.[12, 15]

The marked stability of these films in the dry state led to the investigation of (PEO/PAA) multilayers as solid polymer electrolytes. DeLongchamp[11] proposed that

lithium-doped hydrogen-bonded LbL films containing PEO might possess room temperature conductivities approaching amorphous PEO-LiTriflate ($\sim 10^{-6}$ S cm^{-1}),[16, 17] given that hydrogen bonding interactions suppress PEO crystallization. A single assembly pH was investigated, and the reported dry conductivities of the LbL assemblies (7 % relative humidity (RH), 25 °C), even when doped with lithium triflate, were $\sim 10^{-10}$ S cm^{-1}.[11] The reason for the discrepancy was not well understood at that time, but some hypotheses[11] were suggested: (i) a high glass transition temperature, leading to a "glassy" matrix and low charge carrier mobility, (ii) a high cross-link density, decreasing segmental motion, and (iii) low PEO content, where PAA dilutes ion-conducting PEO. However at that time, little was known of the composition, structure, and materials properties of the adsorbed multilayers because film isolation proved challenging.

Recently, the authors reported a non-destructive "peel-away" technique,[9] for successfully isolating hydrogen-bonded LbL films of sufficient mass (> 20 mg) and area (> 4 in^2) to study the glass transition temperature, modulus, and dynamic mechanical response of "neat" (without lithium salt) (PEO/PAA) multilayers.[9] Of note, PEO crystallization was suppressed, and a single glass transition temperature (T_g) that varied with assembly pH was reported. The T_g-pH dependency was proposed to be related to the *intra-* and *inter-* molecular hydrogen bonding of PAA.[9] A more recent report,[18] investigates the effect of hydrophobic interactions within multilayers of hydrophobically modified PEO and PAA. In these previous studies, the influence of salt addition upon materials properties and pH-dependency of (PEO/PAA) films was not explored. This understanding is critical for the design of LbL electrolytes with sufficient charge carrier concentrations for electrochemical applications.

Here, we examine and estimate the degree of *intra-* and *inter-* molecular hydrogen bonding of PAA within hydrogen-bonded (PEO/PAA) multilayers assembled at varying pH. Films assembled in the presence of 0.1 M lithium triflate are compared to those assembled without, and the resulting properties (e.g. glass transition temperature, ionic conductivity) are found to be quite unique. The presence of added salt appears to encourage dimerization of PAA and weaken PEO-PAA interactions, yielding PAA-rich films with an elevated glass transition temperature. Additionally when assembly pH was varied, a maximum dry ionic conductivity of lithium triflate-doped films was observed,

$\sim 10^{-8}$ S cm^{-1} (0 % RH, 35 °C). These results support the previously proposed hypothesis regarding the pH-dependency of *intra-* and *inter-* molecular hydrogen bonding of PAA,[9] where the two interactions compete within neat (PEO/PAA) multilayers. Also, findings from FTIR spectroscopy, differential scanning calorimetry (DSC), and electrochemical impedance spectroscopy (EIS) are compared to reports of solution-cast PEO/PAA complexes.

3.2 Materials and Methods

Solution preparation. Poly(ethylene oxide) (PEO) of 4,000,000 molecular weight (MW) and poly(acrylic acid) (PAA) of 90,000 MW were purchased from Polysciences. Separate solutions of 0.02 M PEO and PAA (based upon monomer unit) were made by dissolving polymer in 18.2 MΩ MilliQ water and stirring overnight. Some polymer solutions also contained 0.1 M $LiCF_3SO_3$, or lithium triflate (Sigma Aldrich).

Layer-by-layer (LbL) assembly. Substrates used were patterned ITO on glass (Delta Technologies), silicon wafer (Silicon Quest), and polystyrene weigh-boats (VWR). ITO substrates were cleaned by sequential sonication in dichloromethane, acetone, methanol and MilliQ water for 15 minutes each. Silicon wafer was cleaned by immersion in piranha solution (70/30 v/v sulfuric acid and hydrogen peroxide) for two minutes. *Caution: Piranha solution is extremely corrosive.* Polystyrene substrates were cleaned by sonication in MilliQ water for 30 minutes. ITO and Si substrates were oxygen plasma treated for two minutes prior to assembly.

Layer-by-layer (LbL) assembly was performed at a specified pH, where each bath was pH adjusted using hydrochloric acid. An automated slide stainer (HMS Series by Zeiss) was used to perform LbL assembly. First, the substrate was immersed in 0.02 M PEO solution at specified pH for 15 minutes, followed by three rinse steps of two, one and one minutes each in MilliQ water. Then, the substrate was exposed to 0.02 M PAA solution at the same specified pH for 15 minutes, followed by three similar rinse steps. All rinse baths were pH adjusted to match PEO and PAA assembly pH. These steps comprise one cycle (or layer pair) of LbL assembly, which may be repeated *n* times. Following assembly, films were gently dried using high velocity air. Some films were assembled in

the presence of 0.1 M $LiCF_3SO_3$, where lithium salt was present in all assembly and rinse baths. Films assembled with lithium triflate in solution are termed $(PEO/PAA)_{LiTrif}$ and those assembled without added salt are termed "neat" (PEO/PAA). Following construction, films were dried in at 40 °C for at least one hour and kept in a desiccator until further use.

Dry film thickness was measured using a Tencor P-10 profilometer. Reported values represent the average and standard deviation of at least three thickness measurements.

Fourier-transform infrared (FTIR) spectroscopy. LbL films of 30 layer pairs assembled atop silicon wafer were probed using FTIR (Nicolet 550 Magna), where bare silicon wafer was taken as the background. Samples were nitrogen purged for at least 30 minutes prior to measurement. Scan resolution was 4 cm^{-1}, and a minimum of 1024 scans were signal averaged for each sample. Kaleidagraph software was used to model the summation of two Gaussian peaks.

Differential scanning calorimetry (DSC). LbL films, assembled atop polystyrene, were isolated by peeling the film away from the substrate, and three to five milligrams were studied using DSC (TA Instruments Q1000). Films were first cooled to -90 °C and then heated to 105 °C at a rate of 10 °C/min. The sample was held at 105 °C for five minutes and then cooled to -90 °C at the same rate. This temperature cycle was repeated three times, and data reported here was taken from the second scan. The glass transition temperature was estimated from the inflection point of the sigmoidal portion of the heating curve.

Thermal gravimetric analysis (TGA). LbL films were isolated from polystyrene, described above, and 10 to 20 milligrams of sample were studied using TGA (TA instruments Q50). Following a 30 minute purge, samples were heated from room temperature to 700 °C at a rate of 10 °C/minute under nitrogen. Water content was calculated from the first step in weight loss, ~50 to 70 °C. The degradation response of PEO and PAA overlapped and was not reproducible from batch to batch.

Elemental analysis. Isolated LbL films were analyzed for carbon, hydrogen, oxygen and sulfur using elemental analysis (Midwest Microlab, LLC). Measurement error was reported as +/- 0.3 wt%.[19]

Electrochemical impedance spectroscopy (EIS). A Solartron 1260 was used to study the impedance response of LbL films in an ITO|LbL|Au cell, previously described,[20] where ITO and Au are considered blocking electrodes. Briefly, 30 layer pairs were assembled atop patterned ITO substrates (Delta Technologies), and gold electrodes were thermally evaporated (100 nm thick, Edwards 306) atop the multilayers. The active area was 6 mm^2. Each ITO substrate was patterned to yield 8 cells, and data presented here constitutes the average and standard deviation of these cells.

Dry, 0 % relative humidity (RH), EIS measurements were performed in an argon-filled glove box (MBraun) with < 2 ppm water content. Humid, 53 % RH EIS measurements were performed in a sealed box containing hydrated magnesium hexahydrate salt. Samples were allowed to equilibrate for at least one week, or until successive impedance measurements remained stable. The voltage amplitude was 100 mV and each data point was integrated over 10 seconds for each frequency. A cyclic voltammogram from -100 to 100 mV of a (PEO/PAA) multilayer film gave a linear response, which suggests that this voltage range is suitable for EIS investigation. The frequency range investigated was 5 MHz to 0.1 Hz. Noisy data obtained at low frequencies ($|Z| > 10^7\ \Omega$) was discarded.

3.3 Multilayer Growth

The layer-pair, or cycle, thickness for LbL systems varies widely depending on the type of system chosen. For example, electrostatic LbL films using strong polyelectrolytes, poly(styrene sulfonate) and poly(diallydimethyl ammonium chloride),[21] have a cycle thickness of 0.7 - 4 nm (depending on ionic strength), whereas hydrogen-bonded LbL assemblies of PEO and PAA[11] exhibit a layer-pair thickness of 0.5 – 100 nm (depending on pH). Previous work by DeLongchamp,[11] indicated that modest addition of salt (< 0.5 M $LiCF_3SO_3$) enhances cycle thickness, an effect attributed to screening-enhanced adsorption;[11] however, this phenomena was only investigated at a single assembly pH, 2.5. To some degree, the layer-pair thickness is an indicator of the strength

of intermolecular interaction, where weaker interactions between polymers A and B result in thicker, lightly ionically cross-linked films.[11, 21, 22]

To understand the effect of added salt and assembly pH upon the layer-pair thickness in hydrogen-bonded LbL assemblies, two systems were investigated: neat (PEO/PAA) and $(PEO/PAA)_{LiTrif}$, where "neat" (PEO/PAA) refers to films assembled in the absence of added salt, and $(PEO/PAA)_{LiTrif}$ refers to films assembled in baths containing 0.1 M $LiCF_3SO_3$, lithium triflate. The thickness of the LbL films, 30 layer pairs each, assembled at varying pH was measured using profilometry, and the cycle thickness was calculated by simply dividing total dry film thickness by the number of cycles (Figure 3-1). Observed neat (PEO/PAA) layer-pair thicknesses coincided with those earlier reported,[11] where cycle thickness was 80 to 90 nm from pH 2 to 2.75 and decreased to 60 nm per cycle at assembly pH 3.25. This decrease results from the partial ionization of PAA at higher pH, yielding a "modulation window" where film formation is hindered by electrostatic repulsion.[11] In contrast, $(PEO/PAA)_{LiTrif}$ multilayers were generally thicker than their neat counterparts, and cycle thickness decreased from 126 to 50 nm at assembly pH 2.00 to 3.25, where a modulation window was also observed. The presence of this effect suggests that the ionization of PAA (pKa = 5.5-6.5),[2, 23] even in the present of 0.1 M salt, is sufficiently strong so as to suppress film formation at elevated pH > 3.

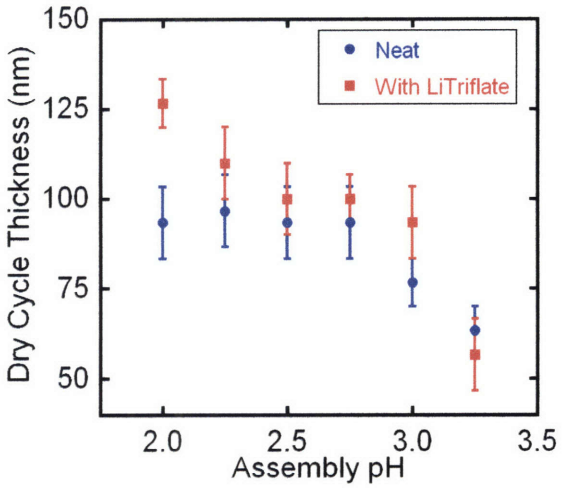

Figure 3-1. Dry cycle thickness of neat (PEO/PAA) and $(PEO/PAA)_{LiTrif}$ multilayers on silicon with varying assembly pH 2.00 to 3.25. Total thickness was measured using profilometry and averaged over a sample 30 layer-pairs thick.

The difference in cycle thickness between neat (PEO/PAA) and $(PEO/PAA)_{LiTrif}$ systems suggests that the nature of *inter*molecular hydrogen bonding between PEO and PAA changes in the presence of added salt. The presence of 0.1 M salt results in thicker films because *inter*molecular hydrogen bonding may be effectively shielded, or weakened, leading to loopier, thicker films. Also, the conformation of each polymer species may affect *inter*molecular hydrogen bonding interactions, and therefore cycle thickness.

3.4 FTIR Spectroscopy Analysis

To further understand the structural state of PAA and PEO within the LbL film, Fourier-transform infrared (FTIR) spectra of neat (PEO/PAA) and $(PEO/PAA)_{LiTrif}$ multilayers in dry nitrogen were collected for films assembled at pH ranging from 2 to 3. Sample spectra of films assembled at pH 3 are shown in Figure 3-2; here, the presence of PEO and PAA is clear in both systems. Peak positions at 850, 1060-1120 and 1120-1170 cm^{-1} are similar to C-O-C stretch and CH_2 rock peaks reported for PEO in its amorphous state (855, 1107 and 1140 cm^{-1}).[24] Also, strong absorption at 1700-1750 cm^{-1} is indicative of carbonyl C=O stretching[25-27] typical of polycarboxylic acids such as PAA, and evidence of hydroxyl-hydrogen bonding is demonstrated by the broad absorption peak, ~3100 cm^{-1}.[28, 29] Films assembled in the presence of $LiCF_3SO_3$ exhibited increased absorbance near 1040 cm^{-1} attributed to SO_3,[27, 30] suggesting that some amount of lithium triflate is incorporated within the $(PEO/PAA)_{LiTrif}$ film.

The carboxylic acid region, which is ~1700 to 1750 cm^{-1} for COOH and ~1550 cm^{-1} for COO^-,[12, 25-27] was of particular interest because it describes the state of PAA within the LbL film. Figure 3-3 presents a peak with two features (~1710 and ~1740 cm^{-1}) that was observed in neat (PEO/PAA) systems. Given the work of Coleman and Painter,[29, 31, 32] the lower-wavenumber peak (~1710 cm^{-1}) is attributed to the *intra*molecular hydrogen bonding of PAA, where two carboxylic acid groups form a dimer. The higher-wavenumber peak (~1740 cm^{-1}),[29, 32] associated with *inter*molecular hydrogen bonding, can be attributed to acid-ether interactions between PAA and PEO. The position of the two peaks remained constant with assembly pH at 1711-1713 and 1739-1740 cm^{-1}.

Qualitatively, the 1711 cm^{-1} peak intensity appears to decrease relative to 1740 cm^{-1} intensity as assembly pH increases. A weak, broad peak near 1600 cm^{-1} is present for samples prepared at pH 2.50, 2.25 and 2.00, but the meaning of this phenomena is unclear. Also of note, a Li^+ - COO^- peak (~1550 to 1570 cm^{-1}, broad and strong)[26, 33] was not observed in either of the investigated (PEO/PAA) systems.

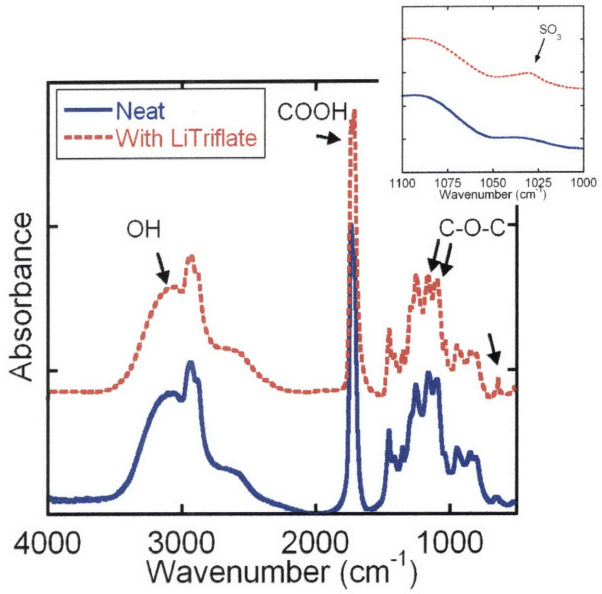

Figure 3-2. Sample FTIR spectra of neat (PEO/PAA) and $(PEO/PAA)_{LiTrif}$ multilayers assembled at pH 3 on IR-transparent silicon. Both spectra show evidence of PEO, PAA and hydrogen bonding interactions. Inset is of SO_3 region, ~1040 cm^{-1}.

Films of $(PEO/PAA)_{LiTrif}$ were characterized in a similar manner. Spectra in the COOH region (Figure 3-4) exhibit a similar shape to those observed in the neat (PEO/PAA) system (Figure 3-3). Here, too, a peak with two features positioned at 1714-1715 cm^{-1} and 1739-1741 cm^{-1} was observed. Qualitatively, the ~1715 cm^{-1} peak intensity decreased only slightly with respect to ~1739 cm^{-1} peak intensity as assembly pH increased.

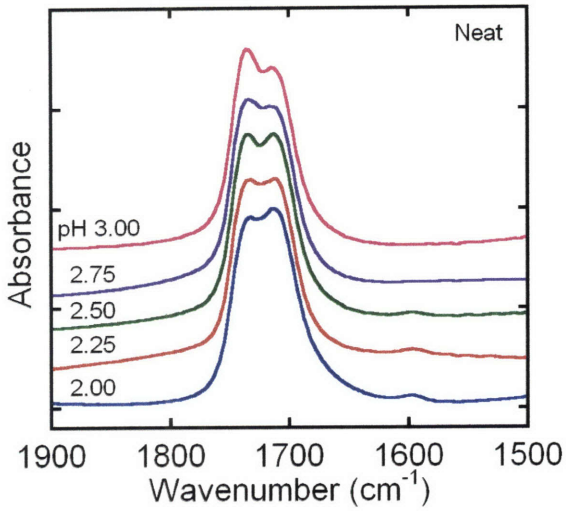

Figure 3-3. FTIR spectra of the carboxylic acid region of neat (PEO/PAA) multilayers assembled at pH 2.00 to 3.00 on IR-transparent silicon. The two peaks (~1710 and 1740 cm^{-1}) appear to decrease and increase in intensity, respectively, as assembly pH increases.

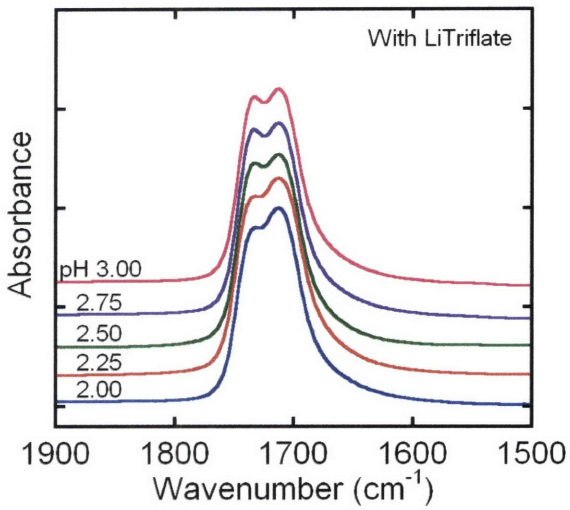

Figure 3-4. FTIR spectra of the carboxylic acid region of $(PEO/PAA)_{LiTrif}$ multilayers assembled at pH 2.00 to 3.00 on IR-transparent silicon. Peaks locations (~1714 and 1740 cm^{-1}) and intensity appear to be relatively invariant despite increasing assembly pH.

Assuming the observed peaks may be modeled as the summation of two Gaussian curves, each contribution may be separately estimated (Figure 3-5). From the calculated area of each Gaussian contribution, the percentage of COOH groups participating in *inter*molecular hydrogen bonding (or "free" COOH) (Figure 3-6) using the following relationship from Coleman, et al.[29] is calculated: *Inter*molecular H-bonding COOH = $Area_{1740}/(Area_{1711}/a_r+Area_{1740})$). In this case, the absorptivity ratio, a_r, was assumed to be similar to Coleman's value reported for methacrylic acid co-polymer (EMAA) / polyether blends (EPO) (a_r = 1.6).[29] For the neat (PEO/PAA) system, the percentage of COOH groups participating in *inter*molecular hydrogen bonding increases (27 to 51%) with increasing assembly pH (2 to 3, respectively); on the other hand for the $(PEO/PAA)_{LiTrif}$ system, 12 to 15 % of COOH groups participate in *inter*molecular hydrogen bonding, independent of assembly pH. For comparison in neat PMAA/PEO LbL films (assembled at pH 2), Sukhishvili and Granick[12] estimate that 10% of carboxylic acid groups are *inter*molecularly hydrogen-bonded, though it should be noted that PEO-PMAA interactions differ from PEO-PAA interactions. Possible error in the analysis may arise from the assumed absorptivity coefficient, which may not be identically a_r = 1.6 (EMAA/EPO blend)[29] for this particular system (PEO/PAA LbL film). The absorptivity coefficient of PEO/PAA is unknown.

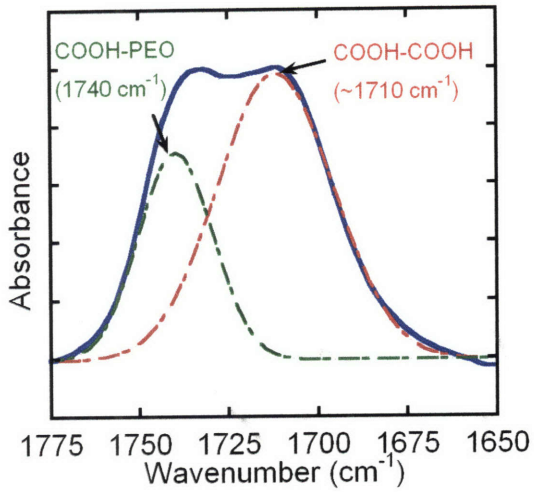

Figure 3-5. FTIR spectra of the carboxylic acid region of neat (PEO/PAA) multilayers assembled at pH 2.5 (blue solid curve). The contribution from *intra*molecular hydrogen bonding (red dashed curve, ~1710 cm^{-1}) and *inter*molecular hydrogen bonding (green dashed curve, ~1740 cm^{-1}) was calculated assuming the summation of two Gaussian peaks.

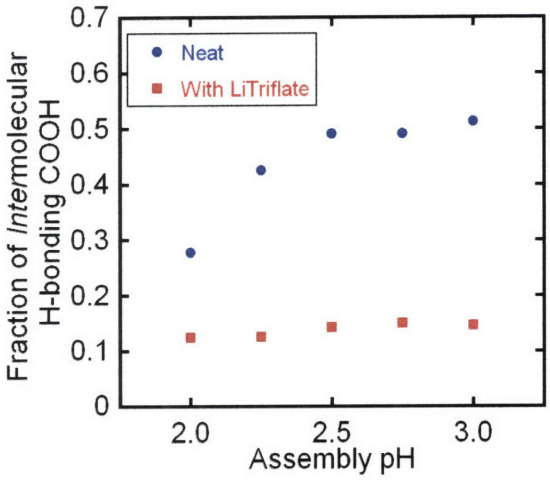

Figure 3-6. The fraction of *inter*molecular H-bonding PAA monomers, as calculated using ref. 29., for (PEO/PAA) and $(PEO/PAA)_{LiTrif}$ multilayers. *Inter*molecular H-bonding COOH = $Area_{1740}/(Area_{1711}/a_r+Area_{1740})$).[29] The areas were calculated assuming the summation of two Gaussian peaks, as described above.

This analysis suggests that the addition of lithium triflate to each dipping bath promotes *intra*molecular hydrogen bonding of PAA, which may explain the observed cycle thicknesses discussed previously. $(PEO/PAA)_{LiTrif}$ multilayers exhibited greater cycle thicknesses, which points to weaker *inter*molecular hydrogen bonding interactions relative to neat (PEO/PAA) systems. From FTIR, the degree of intermolecular interaction was estimated, where films with added salt have significantly less (12-15 % *inter*molecular H-bonding COOH) PEO-PAA hydrogen bonding as compared to neat (PEO/PAA) multilayers (27-51 % *inter*molecular H-bonding COOH, depending on pH). This hypothesis suggests that intermolecular and intramolecular interactions compete during film formation when added salt "screens" PEO-PAA hydrogen bonding, regardless of assembly pH. Though FTIR spectroscopy yields information concerning the extent of hydrogen bonding of PAA monomer units, the overall cross-link density of the multilayer systems are unknown because the fraction of PEO monomer units participating in hydrogen bonding could not be quantified using this analysis.

For comparison, solution-cast blends of PEG and PAA with no added salt both demonstrated *intra-* and *inter*-molecular hydrogen bonding via FTIR (1706 and 1732 cm^{-1}, respectively),[26] where the addition of PEG was shown to disrupt cyclic dimers and to favor the formation of acid-ether hydrogen bonding.

In comparison, PAA in electrostatically assembled LbL films is known to further ionize within the film, as PAA pKa decreases to accommodate electrostatic cross-linking;[22, 23] however in hydrogen bonding systems, the ionization of PAA within the film is unfavorable, as it may compromise film stability.[12, 15] From FTIR, the absence of the COO^- band (~1550 cm^{-1}) in both of the (PEO/PAA) systems indicates that PAA is present in its fully protonated form and is capable of hydrogen bonding with PEO. To disrupt (PEO/PAA) multilayer stability, exposing the as-made LbL film to water at pH > 3.6 results in complete deconstruction, where PAA is 2-3% ionized.[12] When ionic strength is increased, this critical pH of deconstruction increases (stability increases) where added salts appear to screen the ionized PAA.[12, 15] The onset of pH-stability for this system is similar to those reported for solution complexes of PEO and PAA.[24, 34]

3.5 Thermal Properties and Composition

Given varying degrees of acid-ether hydrogen bonding, as evidenced above, the glass transition temperature and composition of PEO/PAA multilayers is expected to reflect these interactions. The thermal properties of neat (PEO/PAA) and $(PEO/PAA)_{LiTrif}$ films assembled at pH 2 to pH 3.25 were investigated using DSC. LbL films (100 layer pairs ranging from six to ten micrometers thick) were assembled atop a polystyrene substrate, peeled away and used for analysis. Samples were cooled to -90 °C, heated to 105 °C at 10 °C/minute, held at 105 °C for five minutes, and cooled back to -90 °C at the same rate. This procedure was repeated for three thermal cycles. During the first heating cycle, a glass transition was observed followed by a broad endothermic peak attributed to the desorption or evaporation of water (2 – 3 wt% water from TGA); second and third scans both yielded identical scans with a single glass transition at a temperature above the first cycle's T_g, and the endothermic peak observed in the first heating scan was absent (Figure 3-7). Data and analysis presented here apply to behavior observed during the second heating cycle.

A typical thermal response from DSC for both neat (PEO/PAA) and $(PEO/PAA)_{LiTrif}$ LbL assemblies is shown in Figure 3-8. In the temperature range investigated, both LbL systems (assembled at pH 2.75) exhibit a single glass transition temperature (35 and 50 °C for neat (PEO/PAA) and $(PEO/PAA)_{LiTrif}$, respectively). A melting peak for PEO (65 °C) was not observed in either system.

Because the thermal trace of $(PEO/PAA)_{LiTrif}$ LbL assemblies appears similar to that of neat (PEO/PAA) multilayers, previous findings[9] may be extended to this new system. The absence of a melting peak suggests that PEO within the film is amorphous, rather than crystalline. Also, the presence of a single glass transition temperature (50 °C, $(PEO/PAA)_{LiTrif}$ assembled at pH 2.75) indicates that this LbL film, consisting of PEO, PAA and lithium triflate, behaves as a miscible blend. For comparison, the observed T_g of PEO (MW = $4 \cdot 10^6$) and PAA (MW = 90 000) is -56 °C and 99 °C, respectively.[9] Further evidence of miscibility was given by the clear, transparent appearance of the film.

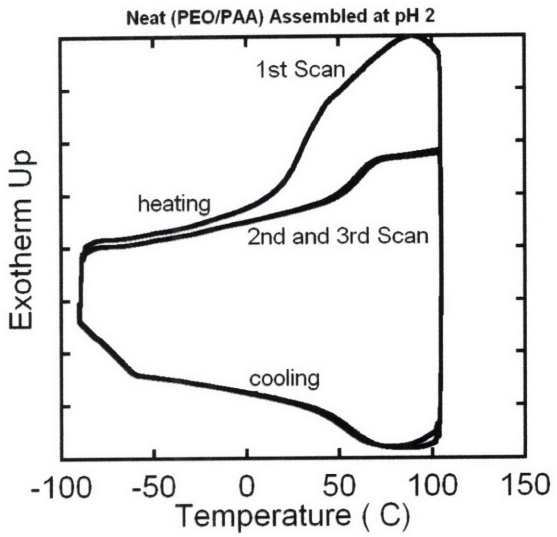

Figure 3-7. DSC thermogram for 100 layer pairs of neat (PEO/PAA) multilayers assembled at pH 2. The first scan shows a T_g (~20 °C) and an endothermic event (~ 95 °C) attributed to water desorption and evaporation. Second and third scans are close to identical, where T_g is ~60 °C. The discontinuity observed upon cooling from -50 to -90 °C is an experimental artifact.

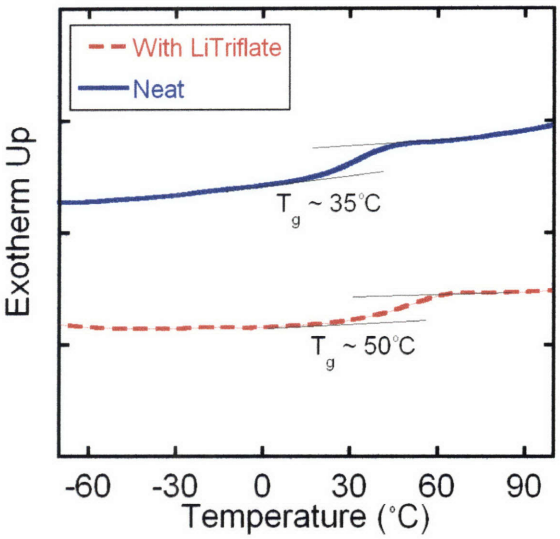

Figure 3-8. DSC trace (second heating scan) for 100 layer pairs (~8 micrometers thick) of neat (PEO/PAA) and $(PEO/PAA)_{LiTrif}$ multilayers assembled at pH 2.75. Both films exhibit a single glass transition, and the T_g is estimated from the inflection point of the sigmoidal region. The melting peak of neat PEO, ~65 °C, is absent in LbL films.

Similar results have also been observed for solution-cast blends of PEG (MW = 5000) and PAA (MW = 50 000), where these hydrogen-bonded blends, miscible over the entire composition range, exhibited a T_g that was composition-dependent and intermediate between those of the pure constituent polymers.[26] The reported T_g ranged from ~ -65 °C (pure PEG) to ~ 70 °C (pure PAA),[26] where we calculate that the reported solution-cast complex T_g was +/-10 °C within the T_g predicted by the Fox equation, discussed later. In an earlier and separate study,[35] the T_g of PEO/PAA associated complex was investigated (without pH adjustment); a minimum T_g of 5 °C was reported when complex composition was 50 wt% PEO.

When LbL assembly pH varies from pH 2 to pH 3.25, the glass transition temperature of the neat and the lithium triflate systems each vary in a different manner (Figure 3-9). Neat (PEO/PAA) multilayers exhibit a T_g that decreases with increasing pH (59 °C at assembly pH 2 and 26 °C at pH 3), as previously described;[9] however, $(PEO/PAA)_{LiTrif}$ multilayers exhibit a T_g (48 - 54 °C) that is relatively invariant of assembly pH. Of note, the T_g of neat (PEO/PAA) multilayers assembled at pH 3.25 varied widely, as shown by the breadth of the error bar in Figure 3-9, likely a result of the film's instability at this condition. In some samples, two glass transition temperatures where observed for neat (PEO/PAA) systems assembled at pH 3.25, which suggests some degree of phase separation at this condition. These films also exhibited an opaque appearance and optical microscopy demonstrated phase separation within the film on the micrometer scale.

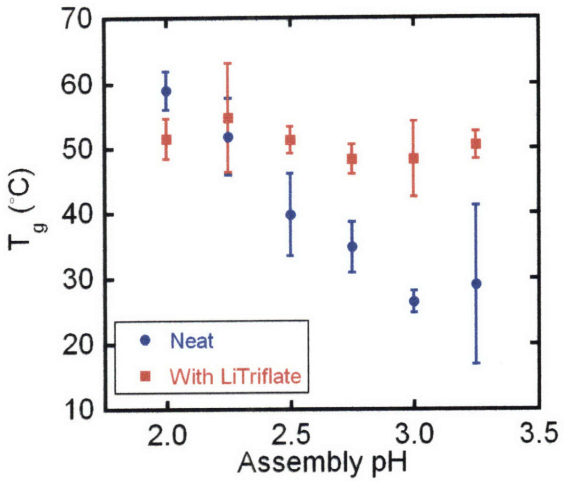

Figure 3-9. Variation of glass transition temperature with assembly pH. The $(PEO/PAA)_{LiTrif}$ system exhibits a T_g that is invariant with assembly pH, whereas the T_g of the neat (PEO/PAA) system decreases with increasing pH. The T_g is estimated from the second heating scan.

The behavior of the T_g of neat (PEO/PAA) multilayers is believed to be caused by the tendency of PAA to *intra*molecularly hydrogen bond.[9] For instance at pH 2, much of the carboxylic acid functional groups are occupied via *intra*molecular hydrogen bonding (or dimer formation), and few COOH groups are available for *inter*molecular hydrogen bonding with PEO. Recall that at assembly pH 2, FTIR results indicated that 27% of PAA units participate in hydrogen bonding with PEO. To compensate for the lack of "free" PAA acid groups (*i.e.* COOH groups H-bonding with PEO), the film will be enriched with PAA and the glass transition temperature will shift toward that of PAA (99 °C). As assembly pH increases from 2.00 to 3.25, *inter*molecular hydrogen bonding becomes more favorable relative to *intra*molecular hydrogen bonding: the amount of PEO within the film increases and T_g decreases. For example at assembly pH 3, the fraction of PAA units hydrogen bonding with PEO increases to 51 %, and T_g decreases to 26 °C. Though PEO was once thought to be the dominant component in PEO/PAA LbL films,[11] the observed glass transition temperature reflects a miscible blend that is rich in PAA.

In the presence of added salt in each assembly bath, the multilayers' glass transition temperature remains constant with respect to assembly pH (Figure 3-9), but the reason for

this behavior is not well understood. We believe that the conformation of each polymer in 0.1 M $LiCF_3SO_3$ solution may play a key role. PAA in a solution of moderate ionic strength may be sufficiently shielded such that *intra*molecular hydrogen bonding is promoted. At such high ionic strength, the solution structure of PAA is highly shielded (coiled sphere),[36] and may not change appreciably in the pH range investigated. In a similar solution environment, the hydrodynamic radius of PEO will decrease with increasing ionic strength, but will remain constant with changes in solution pH.[24] In short, the presence of 0.1 M $LiCF_3SO_3$ in the assembly solution decreases the effect of pH variation. A similar observation was noted in FTIR spectroscopy studies (Figure 3-6). $(PEO/PAA)_{LiTrif}$ assemblies exhibited COOH spectra and *inter*molecular hydrogen bonding (12-15 %) that remained relatively constant despite variation in assembly pH. Also recall that from FTIR spectroscopy, COOH is fully protonated and no ionization (COO^-) was observed.

From observed variations in T_g, one might expect a similar response in film composition. The Fox Equation may be used to roughly estimate film composition, assuming an ideal polymer blend with no interactions;[37] however, the presence of hydrogen bonding constitutes a molecular interaction that may cause deviation from ideality.[38] For this reason, the detection of composition via elemental analysis was attempted.

LbL films were analyzed for carbon, hydrogen and oxygen content, but results appear inconclusive. For changes in neat PEO/PAA multilayer composition, carbon, hydrogen and oxygen content is expected to vary from 50.0, 5.6 and 44.4 % (pure PAA), to 54.5, 9.1 and 36.4 % (pure PEO), respectively. From the Fox equation, it is estimated that the composition of neat (PEO/PAA) films assembled at pH 2.00 and pH 3.00 to be 25 and 46 mol% PEO, respectively. Also the carbon, hydrogen and oxygen content in this pH range is expected to vary from 50.8 to 51.5, 6.2 to 6.8, and 43.1 to 41.7 wt%, respectively. Unfortunately, analysis error (+/- 0.3 wt %) exceeded the projected variation in composition. For example, neat (PEO/PAA) multilayers assembled at pH 2.5 gave a composition of 51.2 % carbon, 6.7% hydrogen, and 42.2 % oxygen, which corresponds to a composition of 45 wt% PEO based upon hydrogen content. Accounting for 0.3 wt% error, the composition of neat (PEO/PAA) multilayers assembled at pH 2.5 was 45 +/- 10

wt%. Multilayer film composition for both systems is summarized in Figure 3-10. Compared to solution-blends of PEO and PAA, isolated precipitate was reported to be 52 wt% (64 mol%) PEO without pH adjustment[35] or 35 to 45 wt% (25 to 33 mol%) PEO when pH < 4.[34] Our findings resemble the latter, where PEO content within (PEO/PAA) LbL films detected using elemental analysis ranges from 28 to 50 wt % PEO. Recall that in Chapter 2, the PEO/PAA multilayer composition had been analyzed with thermal gravimetric analysis (TGA). TGA was attempted for these systems as well, but because PEO and PAA degrade near the same temperature (PAA in two steps, 235 and ~400 °C, and PEO in one step 400 °C), significant error is introduced into the analysis. For this reason, results from TGA have been excluded in this study. In general, composition calculated from TGA was +/- 10 wt% from composition calculated using the Fox equation and DSC.

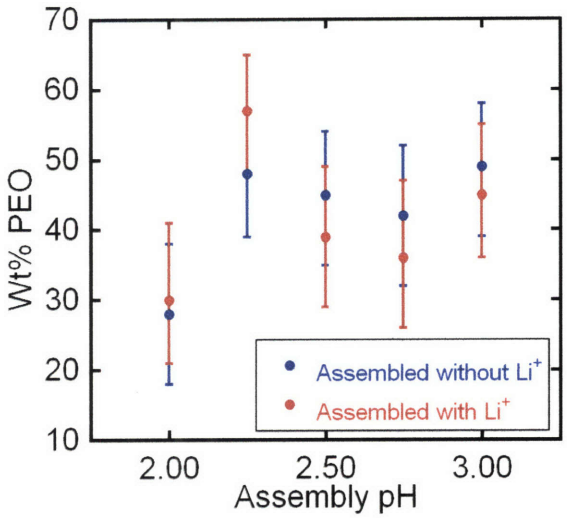

Figure 3-10. The PEO composition of each film was calculated from the hydrogen content detected in elemental analysis. Films containing $LiCF_3SO_3$ were corrected for the presence of the salt, based upon sulfur content. The size of the error bars exceeds the expected variation in composition (via Fox Equation and T_g from DSC analysis).

Films assembled in the presence of lithium triflate ($LiCF_3SO_3$) were also investigated for sulfur, from which the atomic lithium content was estimated. For example, $(PEO/PAA)_{LiTrif}$ multilayers assembled at pH 2.5 contained 0.78 wt% sulfur, yielding an

atomic lithium content of 0.17 +/- 0.06 wt%. For $(PEO/PAA)_{LiTrif}$ multilayers, it was estimated that LbL films assembled at pH 2 to 3 contain 0.1 to 0.3 wt% lithium (Figure 3-11), which roughly corresponds to an EO:Li ratio of 13:1 to 28:1. In comparison, solution-cast blends of PEO.

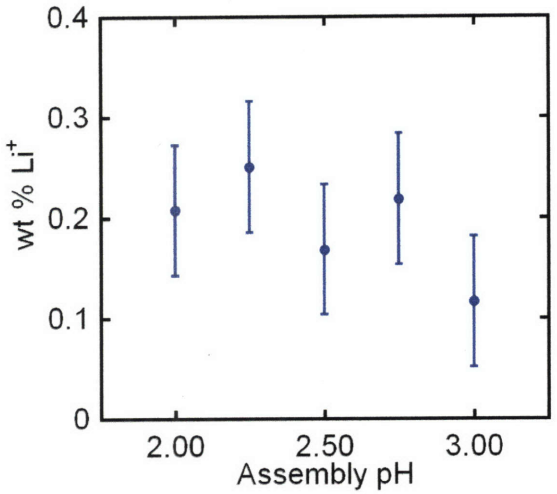

Figure 3-11. Lithium content in $(PEO/PAA)_{LiTrif}$ multilayers assembled at varying solution pH. Lithium content was estimated from the elemental analysis of sulfur, which is present in lithium triflate ($LiCF_3SO_3$). For every mole of sulfur detected, a mole of lithium is present.

3.6 Electrochemical Impedance Spectroscopy

In light of the previous assessment, the ionic conductivity of hydrogen bonding multilayers with and without added salt is expected to reflect changes in assembly pH and salt content. Previous work by DeLongchamp focused on films constructed at a single pH (2.5), where a maximum conductivity of 1.3×10^{-5} S cm^{-1} (52 % relative humidity, 25 °C, 1.0 M added salt) was reported.[11] Dry conductivities ranged from 10^{-12} to 10^{-10} S cm^{-1}, where the low conductivity was attributed to a high (but at that time unknown) glass transition temperature, hydrogen-bonded cross-links, and poor segmental motion.[11] Here, changes in composition, T_g, and *inter*molecular hydrogen bonding (observed via FTIR and DSC) are expected to influence ionic mobility and charge carrier concentration, ultimately affecting ionic conductivity.

Electrochemical impedance spectroscopy was performed on LbL films (30 layer pairs, 2 to 4 micrometers thick) assembled at pH 2 to 3 with or without lithium triflate in a dry, argon-filled glove box using an ITO|LbL|Au cell (see Experimental Section). PEO is known to conduct ions via a "rocking-chair" mechanism, where the alkali lithium cation is readily solvated by the ether oxygen and segmental motion and local relaxations aid in mobility.[39] Conductivity from PAA is attributed to protons via dissociation (though limited in dry air)[11] or cations via counter-ion hopping (though limited as PAA is fully protonated). In comparison, ionic conductivity is expected to be primarily a result of cation interaction with and mobility within PEO.

Both neat and lithium triflate systems exhibited a similar impedance response, or Nyquist plot (Figure 3-12, assembly pH 3.00). At high frequencies, a depressed semi-circle was observed; at low frequencies, a slanted near-vertical line was sometimes observed. Systems with higher impedance (less conductive) did not display the low-frequency vertical line because the impedance response of the system exceeded the limits of the analyzer. The observed response may be modeled by an equivalent circuit[20, 40] consisting of a resistor (R_1) and constant phase element (CPE_1) in series, followed by a resistor (R_2) and constant phase element (CPE_2) in parallel (Figure 3-12). Here, R_1 is considered the resistance of the blocking electrodes and wires, CPE_1 is a non-ideal double layer, R_2 is the resistance of the LbL film and CPE_2 describes bulk polarization of the LbL film. The conductivity of the system is calculated using $\sigma = L/(R_2A)$, where L is the thickness of the LbL film and A is the active area (6 mm^2).

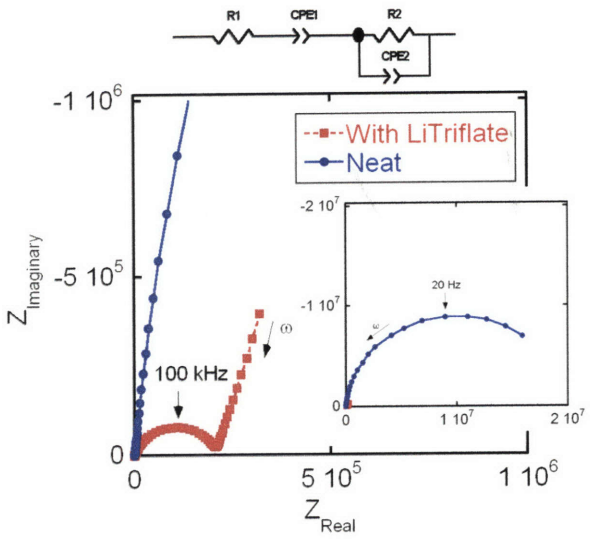

Figure 3-12. Nyquist plot (expanded axes are inset) of neat (PEO/PAA) and $(PEO/PAA)_{LiTrif}$ multilayers (both assembled at pH 3) in a dry, argon-filled glove box at 35 °C. The cell consisted of 30 layer pairs of LbL film sandwiched between blocking electrodes, ITO and Au. Voltage amplitude was 100 mV and frequency range was 5 MHz to 0.1 Hz.

The dry (0 % RH) conductivity of neat (PEO/PAA) multilayers assembled at pH 2 to 3 was 10^{-10} to almost 10^{-9} S cm^{-1} (Figure 3-13), and maximum conductivity detected was 9 +/- 3 · 10^{-10} S cm^{-1} for an LbL film of neat (PEO/PAA) assembled at pH 2.75. In this system, the charge carrier is believed to be residual ions (from assembly pH adjustment) or protons. The general increase in conductivity, when assembly pH varies from 2 to 2.75, may be attributed to the inclusion of more amorphous PEO within the LbL film. From DSC, T_g decreases with increasing assembly pH; thus, PEO content increases with increasing assembly pH. Also, conductivities reported here (measured at ~35 °C), were higher than DeLongchamp's neat film of (PEO/PAA) assembled at pH 2.5, (4 · 10^{-11} S cm^{-1} at 25 °C). This discrepancy may be explained by the measurement conditions, where elevated temperature increases conductivity either via an Arrhenius or Vogel-Tamman-Fulcher relationship.[39]

The dry conductivity of $(PEO/PAA)_{LiTrif}$ assemblies was also investigated, Figure 3-13. Conductivity ranged from below 10^{-9} to above 10^{-8} S cm^{-1} as pH ranged from 2.5 to 3.0.

Maximum conductivity was 1.6 +/-0.2 · 10^{-8} S cm^{-1} at pH 3, 35 °C. Here, conductivity increases with pH, even though the observed glass transition temperature (via DSC) remains relatively invariant. One explanation may be that the charge carrier (Li^+) concentration increases with assembly pH, though this hypothesis was not conclusively verified via elemental analysis.

In comparison, solution-cast blends of PEO and lithium triflate of ether to lithium ratios similar to $(PEO/PAA)_{LiTrif}$ films (13:1 to 28:1) demonstrate dry room temperature conductivities slightly above ~10^{-7} S cm^{-1},[40] which is ten times higher than the maximum conductivity of $(PEO/PAA)_{LiTrif}$ assemblies, ~10^{-8} S cm^{-1}. This difference suggests that the presence of PAA within the film may "dilute" the conductive media (PEO), thus lowering the conductivity.

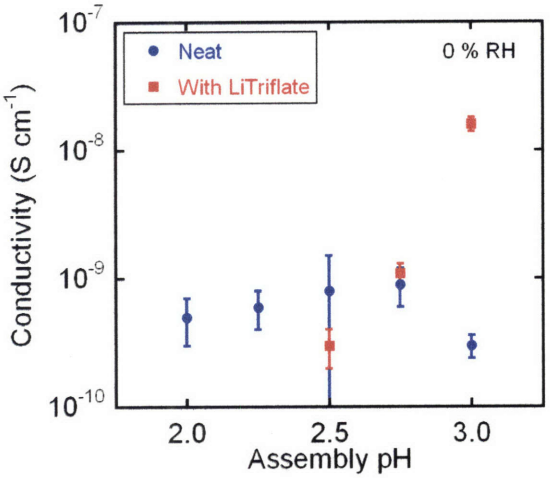

Figure 3-13. Ionic conductivity of neat (PEO/PAA) and $(PEO/PAA)_{LiTrif}$ multilayers of varying assembly pH measured at 0 % RH, 35 °C. The ionic conductivity was estimated from R_2 in the equivalent circuit described above. Measurements were performed in a dry, argon glove box.

The impedance response of both systems was also investigated in a humidity-controlled box maintained at 53 % RH, where LbL films absorb water, which acts as a plasticizer, from the humid environment.[41] In this case, the impedance response was similar to measurements performed in the dry state, and could be modeled using the same

equivalent circuit. The calculated conductivities (Figure 3-14) were measured with varying assembly pH for neat (PEO/PAA) and $(PEO/PAA)_{LiTrif}$ systems. Results demonstrate that at pH 3.0 assembly conditions, $(PEO/PAA)_{LiTrif}$ LbL films are 100 times more conductive than neat (PEO/PAA) LbL films (10^{-7} vs. 10^{-9} S cm^{-1}, respectively) at 53 % RH, and that conductivity appears to be independent of assembly pH.

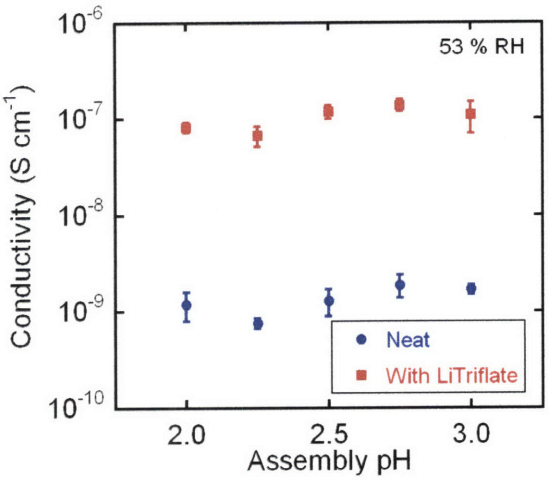

Figure 3-14. Ionic conductivity of neat (PEO/PAA) and $(PEO/PAA)_{LiTrif}$ multilayers of varying assembly pH measured at 53 % RH, 25 °C. Measurements were performed in a humidity controlled vessel using magnesium nitrate hexahydrate. The ionic conductivity was estimated from R_2 in the equivalent circuit described above.

The differences observed between the two systems at 0 % and 53 % RH are explained by the relationship $\sigma = nq\mu$,[39] where σ is ionic conductivity, n is the number of charge carriers, q is electronic charge and μ is the mobility of the charge carriers. For example, adding lithium triflate to each assembly solution increases n so ionic conductivity is expected to increase. Neat (PEO/PAA) LbL films contain few, if any, free ions (no ash left in elemental analysis), whereas $(PEO/PAA)_{LiTrif}$ LbL films contained ~0.17 wt% atomic lithium. At 53 %RH, the influence of charge carrier concentration is clearly evident, where $(PEO/PAA)_{LiTrif}$ multilayers are 100 times more conductive; at 0 %RH, the effect of charge carrier concentration on ionic conductivity is not observed until

assembly pH is above 2.75. The presence of water (humidity) increases μ and promotes local relaxations and segmental motion that are key to increasing ionic conductivity. Together, an LbL film that is both plasticized (via water) and doped (via $LiCF_3SO_3$) will yield a conductivity that is 100-1000 times higher (depending upon assembly pH) than its dry and un-doped counterpart. For example, the conductivity of neat (PEO/PAA) at 0 % RH was $3 \cdot 10^{-10}$ S cm^{-1} and that of $(PEO/PAA)_{LiTrif}$ at 53 %RH was 1.1 10^{-7} S cm^{-1}, each assembled at pH 3.00. Figure 3-15 and 3-16 describe the humidity response of neat (PEO/PAA) and $(PEO/PAA)_{LiTrif}$ multilayers.

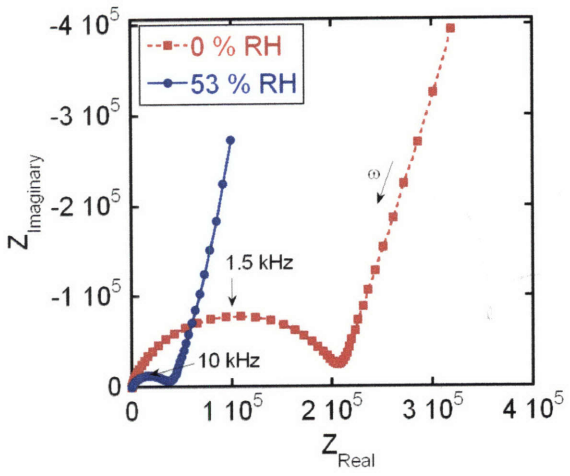

Figure 3-15. Nyquist plot of $(PEO/PAA)_{LiTrif}$ multilayers assembled at pH 3 investigated at 0 % and 53 % relative humidity (35 and 25 °C, respectively). Using the equivalent circuit, described above, the resulting conductivities are $1.6 \cdot 10^{-8}$ and $1.1 \cdot 10^{-7}$ S cm^{-1}, respectively.

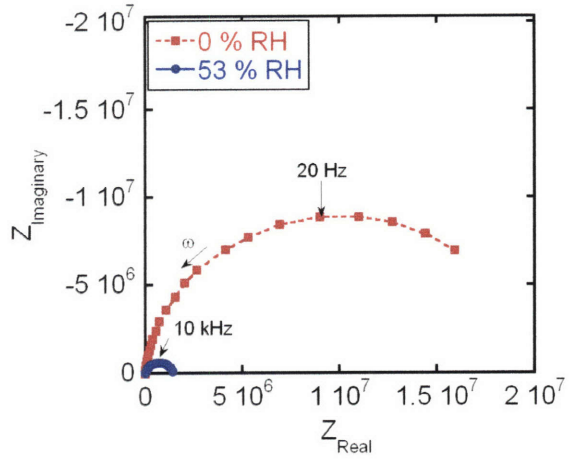

Figure 3-16. Nyquist plot of neat (PEO/PAA) multilayers assembled at pH 3 investigated at 0 % and 53 % relative humidity (35 and 25 °C, respectively). Using the equivalent circuit, described above, the resulting conductivities are $3.0 \cdot 10^{-10}$ and $1.7 \cdot 10^{-9}$ S cm^{-1}, respectively.

In general, conductivity did not vary appreciably with assembly pH, as had been expected. One possible explanation is that the extent of hydrogen bonding interactions, though high enough to yield a stable LbL film, causes the film to behave as a cross-linked matrix where polymer backbones are essentially "pinned down." Also, observed conductivity was below that of solution-cast PEO mixed with lithium triflate (10^{-6} S cm^{-1});[16, 17] this difference is probably caused by the presence of PAA (which essentially dilutes the conductive medium and acts as a charge trap), poor segmental motion of the LbL film (high T_g), and the low concentration of carrier ions. Suggested means of improving conductivity in dry LbL multilayers are (i) increasing the concentration of added salt within each bath or adding salt after assembly (increasing charge carrier concentration),[11] (ii) adding a liquid plasticizer (lowering T_g, increasing μ), and (iii) increasing PEO content.

3.7 Conclusion

In this work, the nature of hydrogen bonding interactions within neat (PEO/PAA) multilayers were compared to those of films assembled in the presence of 0.1 M lithium triflate at a range of assembly pH. $(PEO/PAA)_{LiTrif}$ multilayers were thicker than neat (PEO/PAA) films, an indication of suppressed acid-ether hydrogen bonding interactions in the presence of added salt. From FTIR spectroscopy, 12 to 15 % of PAA monomer units participated in *inter*molecular hydrogen bonding within $(PEO/PAA)_{LiTrif}$ multilayers, independent of assembly pH; in neat (PEO/PAA) multilayers, *inter*molecular hydrogen bonding increases with assembly pH, (27 % at pH 2 and 51 % at pH 3). This implied that for neat (PEO/PAA) multilayers, the PEO composition will increase with assembly pH; for $(PEO/PAA)_{LiTrif}$ systems, the PEO composition is expected to remain invariant. In terms of thermal properties, the glass transition temperature reflected the composition of the multilayer system. The T_g of neat (PEO/PAA) films decreased with increasing pH (59 °C at pH 2 and 26 °C at pH 3), where as the glass transition temperature of $(PEO/PAA)_{LiTrif}$ multilayers was relatively invariant with pH (48 to 54 °C). Together, these results suggest that *inter*molecular hydrogen bonding is suppressed during multilayer assembly in the presence of lithium triflate, whereas the dimerization of PAA is promoted. Because fewer carboxylic acid groups are available for hydrogen

bonding with PEO, the film becomes enriched with PAA and the glass transition temperature increases. The lack of pH-dependency (from pH 2 to 3) in $(PEO/PAA)_{LiTrif}$ multilayers indicates that the presence of 0.1 M salt screens the effect of assembly pH. Using electrochemical impedance spectroscopy, ionic conductivity was found to increase with increasing humidity (increasing mobility) and salt content (increasing charge carrier concentration). $(PEO/PAA)_{LiTrif}$ multilayers had an ionic conductivity of $\sim 10^{-7}$ S cm^{-1} at 53 % RH and dry, neat (PEO/PAA) multilayers were 10^{-10} to 10^{-9} S cm^{-1}. Increasing assembly pH appeared to increase the dry, 0% humidity, conductivity of both neat and lithium triflate (PEO/PAA) systems. In the case of neat (PEO/PAA) multilayers, the dry conductivity is thought to increase with assembly pH because of the decreased T_g (increasing PEO content); in the case of $(PEO/PAA)_{LiTrif}$ multilayers, the increase is possibly attributed to increasing charge carrier concentration.

3.8 References

1. Bekturov, E. A.; Bimendina, L. A. *Advances in Polymer Sciences* **1981,** 41, 100-147.
2. Tsuchida, E.; Abe, K. *Advances in Polymer Sciences* **1982,** 45, 1-125.
3. Tsuchida, E.; Takeoka, S., Interpolymer Complexes and their Ion-Conduction. In *Macromolecular Complexes in Chemistry and Biology*, Dubin, P.; Bock, J.; Davis, R.; Schulz, D. N.; Thies, C., Eds. Springer: Berlin, 1994; pp 183-213.
4. Stockton, W. B.; Rubner, M. F. *Macromolecules* **1997,** 30, (9), 2717-2725.
5. Wang, L.; Wang, Z.; Zhang, X.; Shen, J.; Chi, L.; Fuchs, H. *Macromolecular Rapid Communications* **1997,** 18, (6), 509-514.
6. Kharlampieva, E.; Sukhishvili, S. A. *Journal of Macromolecular Science, Part C: Polymer Reviews* **2006,** 46, 377-395.
7. Baranovsky, V. Y.; Litmanovich, A. A.; Papisov, I. M.; Kabanov, V. A. *European Polymer Journal* **1981,** 17, 969-979.
8. Decher, G. *Science* **1997,** 277, (5330), 1232-1237.
9. Lutkenhaus, J. L.; Hrabak, K. D.; McEnnis, K.; Hammond, P. T. *Journal of the American Chemical Society* **2005,** 127, (49), 17228-17234.
10. Sukhishvili, S. A.; Kharlampieva, E.; Izumrudov, V. *Macromolecules* **2006,** 39, (26), 8873-8881.
11. DeLongchamp, D. M.; Hammond, P. T. *Langmuir* **2004,** 20, (13), 5403-5411.
12. Sukhishvili, S. A.; Granick, S. *Macromolecules* **2002,** 35, (1), 301-310.
13. Kozlovskaya, V.; Sukhishvili, S. A. *Macromolecules* **2006,** 39, (16), 5569-5572.
14. Kozlovskaya, V.; Ok, S.; Sousa, A.; Libera, M.; Sukhishvili, S. A. *Macromolecules* **2003,** 36, (23), 8590-8592.
15. Sukhishvili, S. A.; Granick, S. *Journal of the American Chemical Society* **2000,** 122, (39), 9550-9551.
16. Wieczorek, W.; Raducha, D.; Zalewska, A.; Stevens, J. R. *Journal of Physical Chemistry B* **1998,** 102, (44), 8725-8731.
17. Tarascon, J.-M.; Armand, M. *Nature* **2001,** 414, 359-367.
18. Seo, J.; Lutkenhaus, J. L.; Kim, J.; Hammond, P. T.; Char, K. *Macromolecules* Submitted.
19. Fornefeld, J., Midwest Microlab, LLC. In Personal Communication, 2007.
20. DeLongchamp, D. M.; Hammond, P. T. *Chemistry of Materials* **2003,** 15, (5), 1165-1173.
21. Clark, S. L.; Montague, M. F.; Hammond, P. T. *Macromolecules* **1997,** 30, (23), 7237-7244.
22. Shiratori, S.; Rubner, M. F. *Macromolecules* **2000,** 33, (11), 4213.
23. Choi, J.; Rubner, M. F. *Macromolecules* **2005,** 38, (1), 116-124.
24. Bailey, F. E.; Koleske, J. V., *Poly(ethylene oxide)*. Academic Press, Inc.: New York, 1976; p 87-118.
25. Painter, P. C.; Brozoski, B. A.; Coleman, M. M. *Journal of Polymer Science: Polymer Physics Edition* **1982,** 20, 1069-1080.
26. Lu, X.; Weiss, R. A. *Macromolecules* **1995,** 28, (9), 3022-3029.

27. Bellamy, L. J., *The Infra-red Spectra of Complex Molecules*. Chapman and Hall: London, 1975; p 183-200.
28. Nishi, S.; Kotaka, T. *Macromolecules* **1985,** 18, (8), 1519-1525.
29. Lee, J. Y.; Painter, P. C.; Coleman, M. M. *Macromolecules* **1988,** 21, (2), 346-364.
30. Teeters, D.; Neuman, R. G.; Tate, B. D. *Solid State Ionics* **1996,** 85, (1-4), 239-245.
31. Lee, J. Y.; Painter, P. C.; Coleman, M. M. *Macromolecules* **1988,** 21, (4), 954-960.
32. Coleman, M. M.; Lee, J. Y.; Serman, C. J.; Wang, Z.; Painter, P. C. *Polymer* **1989,** 30, (7), 1298-1307.
33. Han, K.; Williams, L. *Journal of Applied Polymer Science* **1991,** 42, 1845-1859.
34. Bailey, F. E.; Lundberg, R. D.; Callard, R. W. *Journal of Polymer Science: Part A* **1964,** 2, 845-851.
35. Smith, K. L.; Winslow, A. E.; Petersen, D. E. *Industrial and Engineering Chemistry* **1959,** 51, (11), 1361-1364.
36. Hoffmann, H.; Liveri, M. L. T.; Cavasino, F. P. *Journal of the Chemical Society, Faraday Transactions* **1997,** 93, 3161-3165.
37. Fox, T. G. *Bulletin of the American Physical Society* **1956,** 1, 123.
38. Boileau, S.; Bouteiller, L.; Foucat, E.; Lacoudre, N. *Journal of Materials Chemistry* **2002,** 12, 195-199.
39. Gray, F. M.; Royal Society of Chemistry (Great Britain), *Polymer Electrolytes*. Royal Society of Chemistry: Cambridge, 1997; p 175.
40. Bruce, P. G., In *Polymer Electrolyte Reviews*, MacCallum, J. R.; Vincent, C. A., Eds. Elsevier Applied Science Publishers: London, 1996; pp 237-274.
41. Smith, A. L.; Ashcraft, J. N.; Hammond, P. T. *Thermochimica Acta* **2006,** 450, (1-2), 118-125.

Chapter 4 : Anisotropic Structure and Transport in Polymer-Clay Layer-by-Layer Assemblies

Portions of this chapter are reprinted from Lutkenhaus, J. L.; Olivetti, E. A.; Verploegen, E. A.; Cord, B. M.; Sadoway, D. R.; Hammond, P. T. *Submitted to Langmuir.*

4.1 Introduction

Synthetic clays are of interest for tuning bulk properties (rheological, mechanical, transport) at the nanoscale in the design of composite materials because of clay's unique materials properties (e.g. negative charge, silicate surface) and dimensions (e.g. nanoscale, platelet-shaped).[1] The high aspect ratio of the clay platelet is thought to yield superior transport barrier properties, particularly when oriented in layers.[2, 3] Clay composites or clay-modified materials are often produced using mechanical pressure,[4] controlled drying from dilute solution[5] or simple blending. Such systems may be of interest for diffusion blocking layers, mechanical modifiers, coatings, dielectrics, etc.

Montmorillonite and hectorite, both charged layer silicates (smectite clays), intercalated with polyethylene oxide (PEO) and its derivatives have received much attention[4, 6-20] as a single-ion conducting electrolyte owing to recent advances that demonstrate high conductivity and transference numbers near unity.[12-14] PEO complexes with and intercalates layered smectite clays through the competition of PEO and water binding to the clay platelet.[21, 22] A well-studied polymer electrolyte, PEO associates with alkali cations through ion-dipole interactions, and cation mobility is influenced by local relaxations and segmental motion of the polymer backbone.[23, 24] Early work with blended composites of PEO and montmorillonite demonstrated ionic conductivities (σ) of 10^{-9} to 10^{-7} S cm^{-1} at 425 K,[4, 6, 8] values much higher than montmorillonite alone. Adding a lithium salt such as lithium perchlorate can improve the room temperature conductivity ($\sigma \sim 10^{-5}$ S cm^{-1}).[18] Addition of a plasticizer or small molecule such as ethylene carbonate can also improve performance ($\sigma \sim 10^{-4}$ S cm^{-1}),[12-14] but mechanical properties may suffer.

The use of ultra thin electrolytes allows reduction in overall electrolyte resistance, R, which scales with film thickness, L, ($R = L/Area \cdot \sigma$); thus, a film with a low conductivity may provide a small resistance if made sufficiently thin. A simple and elegant way to construct ultra thin, mechanically cohesive polymer-clay nanocomposites is the layer-by-layer (LbL) technique.[25] Molecular species of opposite charge[26, 27] (or hydrogen bonding functionality)[28, 29] are alternately adsorbed on a substrate from aqueous solution to form thin films of tunable thickness, structure and properties.[26-29] Multilayers from positively charged polyelectrolytes and negatively charged clays have been studied as surface-modifiers, coatings, sensors, permeation barriers, and "artificial nacre".[3, 25, 30-41] In general, these layered organic-inorganic composites form a highly-stratified two-dimensional structure,[25] which may be capable of blocking the diffusion of ions[2] or the permeation of gas.[3, 35]

However, to explore applications in which the LbL polymer-clay composites may be part of an electrochemical device, the nature and origin of ionic conductivity must be understood. In this work, we create and characterize layered polymer-clay structures from LbL assembly using a unique combination of materials: PEO, linear polyethylene imine (PEI), and neat or lithium-exchanged Laponite clay (designated as Clay and Li-Clay, respectively). Here, hydrogen bonding is used to introduce PEO into the multilayer film while using a polycation, PEI, to stabilize the composite. The resulting structure, studied using atomic force microscopy (AFM), scanning electron microscopy (SEM), wide angle X-ray diffraction (WAXD) and grazing-incidence small angle X-ray scattering (GI-SAXS), suggests lateral orientation over large areas (> 4 cm^2). We demonstrate and characterize the degree of anisotropic ion transport using electrochemical impedance spectroscopy, and find that dry-state in-plane ionic conductivity ($7.2 \cdot 10^{-8}$ S cm^{-1} at 401 K) is 100 times higher than cross-plane conductivity ($6.8 \cdot 10^{-10}$ S cm^{-1} at 405 K), a result of the layered structure within the film. Thus, structural anisotropy within LbL polymer-clay composite films is correlated to anisotropic ion transport within the same film. To the best of the authors' knowledge, this study represents the first application of electrochemical impedance spectroscopy in determining anisotropic ion transport in LbL assemblies.

4.2 Materials and Methods

Solution preparation. Poly(ethylene oxide) of 4,000,000 molecular weight (MW) and linear poly(ethylene imine) of 25,000 MW were purchased from Polysciences. Polymer solutions of PEO and PEI were separately made using polymer and Milli-Q water. The concentration of polymer was 0.02 M based upon monomer unit. The pH of PEI solution was adjusted to 5.00 +/- 0.01 using hydrochloric acid and a Beckman Coulter 390 pH meter.

Laponite RD, a synthetic hectorite, was purchased from EECS Cosmetics, and the manufacturer-reported diameter and thickness was 50 nm and 1 nm, respectively. A solution of 0.5 wt% Laponite in Milli-Q water was made and stirred overnight. Laponite purchased from the manufacturer contained (exchange-able) sodium cations.[42]

Layer-by-layer film assembly. Films were constructed using a modified programmable Carl Zeiss HMS slide stainer. Substrates used were silicon wafer and ITO-coated glass. Si-wafers were cleaned using piranha solution of 70% sulfuric acid and 30% hydrogen peroxide. *CAUTION: Piranha solution is extremely corrosive.* ITO-coated glass substrates were cleaned by sequential sonication in dichloromethane, acetone, methanol and Milli-Q water for 15 minutes each. Immediately before LbL assembly, the substrate was oxygen plasma-treated for two minutes. After plasma treatment, the substrate was first dipped in PEI solution for 10 minutes, rinsed with agitation in Milli-Q water for two minutes, followed by an additional one-minute rinse. Second, the substrate was exposed to the Laponite solution for 10 minutes and rinsed as before. Finally, the substrate was exposed to PEO solution for 10 minutes and rinsed as before. These three exposures comprise one trilayer of PEI/Clay/PEO. The procedure can be repeated n times to give a film of n trilayers denoted by $(PEI/Clay/PEO)_n$.

The film thickness was measured with either ellipsometry or profilometry depending on film thickness. Film thicknesses less than 150 nm were measured using a Gaertner ellipsometer. Films thicknesses greater than 150 nm were measured using a Tencor P-10 profilometer. The thickness was recorded three times each on two different samples to give one data point.

X-ray photon spectroscopy. Surface characterization and elemental analysis was performed using a Kratos AXIS Ultra Imaging X-ray Photoelectron Spectrometer at 0.5 eV/step and 80 eV pass energy.

AFM. A Dimension 3100 AFM by DI Instruments with a Nanoscope 3A Controller in tapping mode was used to investigate surface morphology of LbL films assembled on silicon. NCH Pointprobe AFM Cantilevers were purchased from Pacific Nanotechnologies.

SEM. Images were captured using a Carl Zeiss LEO field-emission SEM system operating between 1 and 5 keV. 2 nm of Au-Pd was sputter-deposited on the samples prior to imaging to suppress charging. Cross-section images were taken from samples cleaved using a diamond scribe.

WAXD. A Rigaku RU300 X-Ray Diffractometer (CuKα, $\lambda = 1.541$ Å) was used for both powder diffraction and glancing angle WAXD. Powder diffraction of Laponite clay and thin film diffraction of the LbL assembly on silicon was conducted in ambient conditions (25 °C and relative humidity 30 %). Scans were conducted from $2\theta = 3^{\circ}$ to 50° at a rate of 0.01°/second.

GI-SAXS. Experiments were performed at the G1 beamline at the Cornell High Energy Synchrotron Source (CHESS). The wavelength of the incident beam was 1.239Å with a sample to detector distance of 1752 mm, and a 2-D area detector was used for data collection.[43]

Impedance spectroscopy. Cross-plane impedance measurements were conducted using a cell described by DeLongchamp and Hammond.[44] Briefly, patterned ITO-coated glass (Donnelly and DCI) was used as the substrate for LbL assembly. Following LbL assembly atop the ITO-coated glass, gold electrodes (100 nm thick and 2 mm wide) were then thermally evaporated using an Edwards Auto 306. Copper tape from 3M was applied to the gold to form a contact pad. The active area was 6 mm^2.

In-plane conductivity measurements were performed on LbL films deposited on independently addressable microband electrodes (IAMEs) from Abtech Scientific. Each ITO band was 3 mm long with 5 micrometer width and spacing. The active area was given by 3 mm times the thickness of the LbL film.

Impedance measurements were performed using a Solartron 1260. The A.C. amplitude was 100 mV to improve the signal to noise ratio at high impedance. A linear sweep of the cross-plane and in-plane cell from -100 to 100 mV gave a linear current response, confirming that impedance measurements at this amplitude are appropriate.

Samples probed at 53% humidity were enclosed in a sealed chamber with magnesium nitrate hexahydrate salts to maintain humidity. For dry measurements, an argon-filled glove box with ~2 ppm water was used. A home-built Faraday cage and hotplate system allowed control of cell temperature within the glove-box. In both cases, cells were allowed to equilibrate with the box-environment for 24 hours prior to electrochemical measurements.

Lithium-exchanged clay preparation. Lithium-exchanged clay (Li-Clay) was prepared according to Khan and Fedkiw.[12] Briefly, Laponite RD clay was dissolved in Milli-Q water. Excess lithium chloride was added to the solution to facilitate ion exchange. The clay suspension was centrifuged, and the opaque gel was retained. The dissolution and exchange process was repeated twice more. The final gel was heated at 100 °C and then washed with methanol until a drop of silver nitrate in the effluent remained clear to confirm the complete removal of chloride ions. The resulting white powder was dried at 80 °C to give the final product, lithium-exchanged clay, with a calculated yield of 60 wt%.

4.3 Multilayer Assembly Growth Profile

In a desire to produce an LbL film comprised of a polymer electrolyte and a single-ion conductor, negatively-charged Laponite clay was selected as a well-investigated and robust single-ion conductor.[12] In this study, neutral PEO and positively-charged linear PEI were both selected as candidate polymer electrolytes.[24] PEI[44] and PEO,[45] owing to their polar backbones, have demonstrated promising ionic conductivities when used as a

component in electrostatic[44] and hydrogen bonding[45] LbL electrolyte films. Attempts to create LbL structures from neutral PEO and negatively-charged Laponite clay were unsuccessful, owing to the formation of a thixotropic gel during deposition. Also, multilayer formation from positively charged PEI and neutral PEO was unsuccessful.

Film thickness as a function of cycle number *n* was investigated using profilometry and ellipsometry for three systems: (PEI/Clay), (PEI/Clay/PEO) and (PEI/Li-Clay/PEO). Figure 4-1 demonstrates a representative growth profile for these three systems, where each film thickness was measured after drying. In each case a linear slope was obtained, where the thickness per cycle was taken as the slope of the growth profile, Table 4-1.

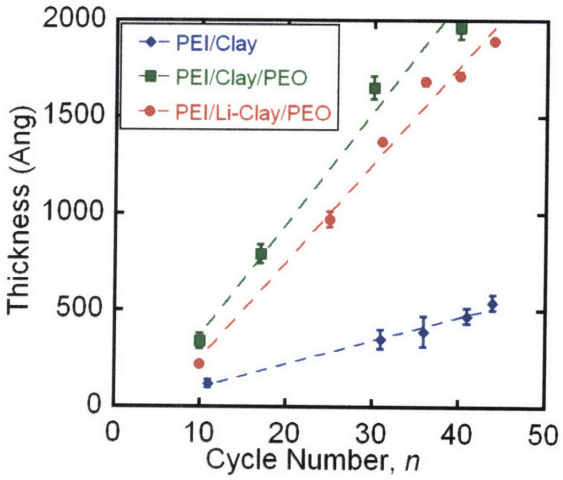

Figure 4-1. (a) Growth profiles of PEI/Clay, PEI/Clay/PEO and PEI/Li-Clay/PEO from ellipsometry and profilometry show that films grow linearly with 11, 55 and 47 Å of material per trilayer, respectively. Film thickness was measured in the dry state.

The shape of the growth profile of each composite resembled previously reported curves for polymer-clay layer-by-layer assemblies.[33, 41] At early deposition cycles, little growth was observed because initial layers of polymer and clay form nucleation islands until a uniform coating covers the substrate.[46] After ten trilayers, the substrate no longer affects polymer and clay adsorption, and film growth proceeds uniformly. The observed

linear growth profile suggests that each cycle results in the deposition of the same amount of material on the substrate.

The cycle-thickness for each of the three systems implies that the clay platelets adsorb in flat or slightly tilted layers. Given a cycle-thickness of 54, 47 or 11 Å (Table 1) and a manufacturer-reported platelet diameter of 50 nm, we calculate using Pythagorean theorem that a single clay platelet may tilt as much as 0.6, 0.5 or 0.1°, respectively, relative to the substrate (Figure 4-2). This behavior can be explained by the negative charge associated with the platelet face.[47] By aligning face-down, platelets can maximize interaction with the underlying positively charged PEI-layer. In contrast, the platelet edge has a positive polarity[47] that discourages edge-up adsorption.

Both neat and lithium-exchanged clay composites produced smooth films, as measured by profilometry. A film of $(PEI/Clay/PEO)_{40}$ exhibited a root-mean-square (RMS) roughness of 2.4 nm, and a film of $(PEI/Li\text{-}Clay/PEO)_{40}$ exhibited a RMS roughness of 3.0 nm by profilometry.

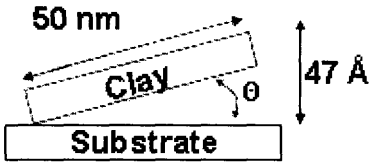

Figure 4-2. Given a clay platelet 50 nm in diameter and a multilayer cycle thickness of 47 Angstroms, a single clay platelet may tilt by theta, 0.5°. This calculation was performed using Pythagorean theorem where 50 nm is considered the hypotenuse of a right triangle.

Table 4-1. Thickness per LbL Cycle

LbL System	Å per cycle
PEI/Clay/PEO	54 +/- 4
PEI/Li-Clay/PEO	47 +/- 3
PEI/Clay	11 +/- 2
PEO/Clay	X
PEI/PEO	X

Because films of only PEO and Clay were gel-like and unprocessable, we sought to include a third component that would stabilize film formation via mutual interactions between PEO and Clay. PEI, partially charged at pH 5,[44] was chosen as the stabilizing component because of its ability to interact with Laponite via electrostatic interactions and PEO via ion-dipole interactions and hydrogen bonding. For comparison, cycle thickness increases from 11 Å for (PEI/Clay) to 54 Å for (PEI/Clay/PEO), which is indicative of incorporation of PEO in the stabilized LbL film.

We hypothesize the following mechanism for film formation in the PEI/Clay/PEO trilayer system. Positively charged PEI adsorbs from solution to a negatively-charged silicon substrate to yield a positive substrate surface charge. Negatively charged Laponite then adsorbs to the PEI-coated substrate, reversing the surface charge. Third, PEO adsorbs to the Laponite-coated surface from solution. It is believed that PEO and clay associate through hydrogen bonding and the desorption of water along the platelet surface.[21, 22] These three steps comprise a single deposition cycle, resulting in a single trilayer of PEI/Clay/PEO. Weak association between PEO (deposited during the nth deposition cycle) and PEI (deposited during the n+1th cycle) through ion-dipole interactions and hydrogen bonding ensures adhesion between successive trilayers. Thus, positively charged PEI is used to associate with both negatively charged Laponite and hydrogen bonding PEO to create stable and cohesive thin films.

4.4 Structure

4.4.1 XPS

X-ray photon spectroscopy (XPS) of $(PEI/Li\text{-}Clay/PEO)_{60}$ multilayers was used to quantify the composition of the LbL assembly. Based on the relative XPS signals of magnesium from the clay and carbon and nitrogen from the polymers, the LbL assembly contained 66, 30 and 4 wt % Li-clay, PEO and PEI, respectively, when clay was the top-most layer as well as when PEO was the top-most layer. Lithium atoms could not be detected owing to their low concentration and the weak XPS signal of the Li 1s orbital. Of note, sodium was present in low concentrations, 0.04 wt %, and chlorine was undetectable.

4.4.2 AFM and SEM

Tapping mode AFM characterized the surface features of an LbL film of $(PEI/Clay/PEO)_{60}$ in which clay was the top-most layer. Circular and oblong features were observed in both the height and phase images (Figure 4-3a and 4-3b, respectively). The diameters of these features (40 to 60 nm) roughly coincide with the manufacturer's reported diameter of the clay platelet (50 nm). RMS roughness from an 800 nm square height image was 3.5 nm, whereas profilometry gave a roughness of 2.4 nm.

Cross-sectional SEM (Figure 4-3c) of a $(PEI/Li\text{-}Clay/PEO)_{200}$ assembly further supports the proposed layered structure. Bright regions are associated with clay platelets, while dark regions are likely polymer. In the micrograph, the edges of individual clay platelets appear to lay parallel to the silicon substrate, while the top of the multilayer film appeared edge-on as a smooth surface. This micrograph is similar to images reported for layered montmorillonite/PDAC LbL structures.[40]

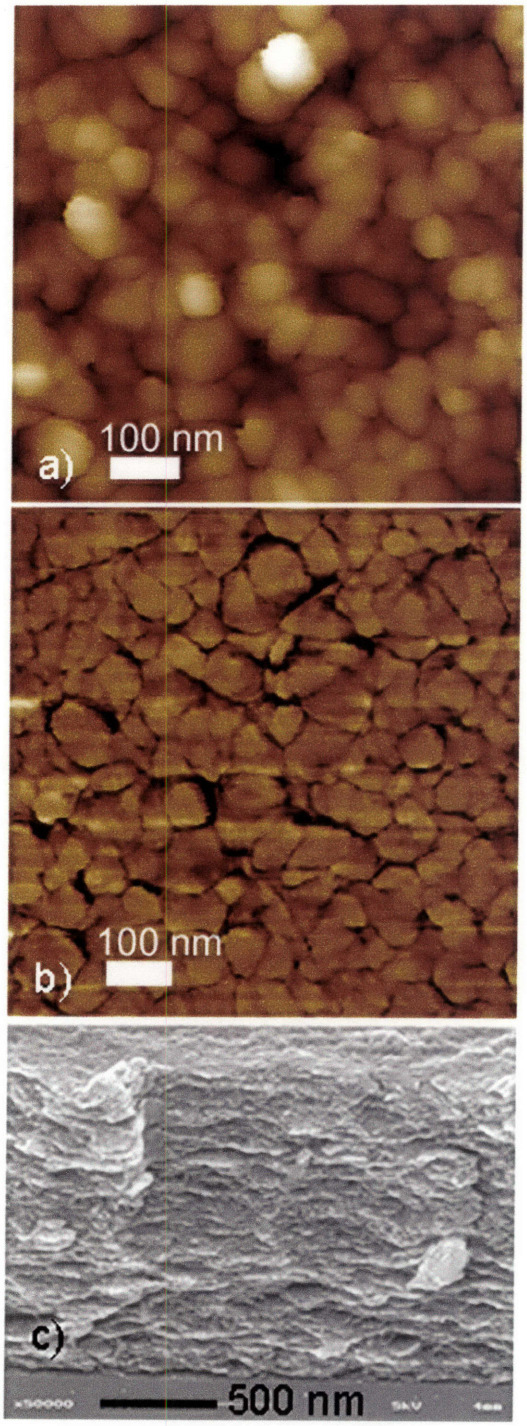

Figure 4-3. Tapping mode AFM height (a) and phase (b) images of a $(PEI/Clay/PEO)_{60}$ film where clay is the top most layer, 800 nm square with 30 nm and 30° scale. Circular/oblong objects are of the same length scale (40 to 60 nm) of clay platelets (50 nm). (c) Cross sectional SEM of $(PEI/Li\text{-}Clay/PEO)_{200}$ multilayers.

4.4.3 Structural Analysis using WAXD and GI-SAXS.

WAXD was performed on neat Laponite powder, an LbL film of $(PEI/Clay/PEO)_{60}$ and an LbL film of $(PEI/Li\text{-}Clay/PEO)_{60}$ in which clay was the top-most layer for both films. Figure 4-4a shows the theta – two theta plot of WAXD. Neat Laponite powder exhibited one shoulder and three distinct peaks in the scan range shown, consistent with previous reports of Laponite.[48] The low-angle shoulder at 6.8° corresponds to a basal (001) spacing of 13.0 Å, which is considered the periodic distance from platelet to platelet. For example, if the platelets are 1 nm thick, as reported by the manufacturer, the gallery spacing (or the distance between stacked platelets) is 3 Å. The Scherrer equation,[49] which estimates crystallite size or range of order, could not be used here because the shape of the basal reflections was not well-defined.

In the $(PEI/Clay/PEO)_{60}$ film, the low-angle peak shifted to 6.3° with a basal spacing of 14.0 Å, where the distance between platelets increased slightly to 4 Å. Two low-intensity higher angle peaks (19.3 and 26.2°) appear at angles similar to those observed in neat Laponite (20.0 and 28.0). Multilayers containing lithium-exchanged Laponite, (PEI/Li-Clay/PEO) exhibited peaks identical to multilayers containing un-lithiated clay, (PEI/Clay/PEO).

Further evidence of the (PEI/Li-Clay/PEO) structure was obtained using GI-SAXS (Figure 4-4b), which measures the orientation of periodic structure within a thin film. The off-specular scattering can be analyzed for incidence angles close to the critical angle of total external reflection of the composite, revealing both lateral structure within the film and structure normal to the substrate.[50] The peak scattering intensity was observed at q = 4.48 nm^{-1}, corresponding to a basal spacing of 14 Å, which is similar to observations from WAXD. Because the observed scattering was preferentially along the film normal, the results suggest that Laponite platelets are oriented parallel to the substrate. The Hermans orientation parameter (f)[43, 51] was used to quantify the degree of orientation within the LbL assembly. This parameter ranges from 1 to -½, in which a value of zero indicates a completely random distribution of orientations. When f is 1 or -½ the system is completely aligned parallel or perpendicular, respectively, to the chosen reference direction (in this case, normal to the substrate). The intensity of the scattering at the scattering vector q in question was analyzed and the Hermans orientation parameter was

found to be 0.7, indicating that the platelets within the LbL assembly have significant, but imperfect, orientation parallel to the silicon substrate.

The peaks from the LbL assemblies observed in WAXD and GI-SAXS suggest periodic structure within the film, i.e. the clay is not exfoliated. The small increase in gallery spacing from 3 to 4 Å (neat Laponite and PEI/Li-Clay/PEO, respectively) does not indicate complete intercalation of polymer between individual platelets; however, the presence of the low angle peaks indicates that for each clay-deposition step, clay platelets are adsorbed from solution in multiple layers – not a monolayer. Given an LbL assembly growth rate of 47 Å per trilayer (from ellipsometry and profilometry), a periodic length scale of 14 Å from clay platelet-to-platelet (from WAXD and GI-SAXS), lateral orientation (from GI-SAXS) and at least two layers of clay adsorbed per trilayer cycle (from WAXD and GI-SAXS), we propose that the multilayer structure of PEI/Li-Clay/PEO consists of alternate, stratified layers of polymer and clay (Figure 4-4c). From XPS, the majority of the polymer-content is thought to be PEO (as stated earlier, multilayers contained 66, 30 and 4 wt % Li-clay, PEO and PEI, respectively). We hypothesize that anisotropic structure of the LbL film, as confirmed by AFM, SEM, WAXD, GI-SAXS and growth profiles, influences ionic conductivity with respect to orientation. This was investigated using electrochemical impedance spectroscopy, detailed below.

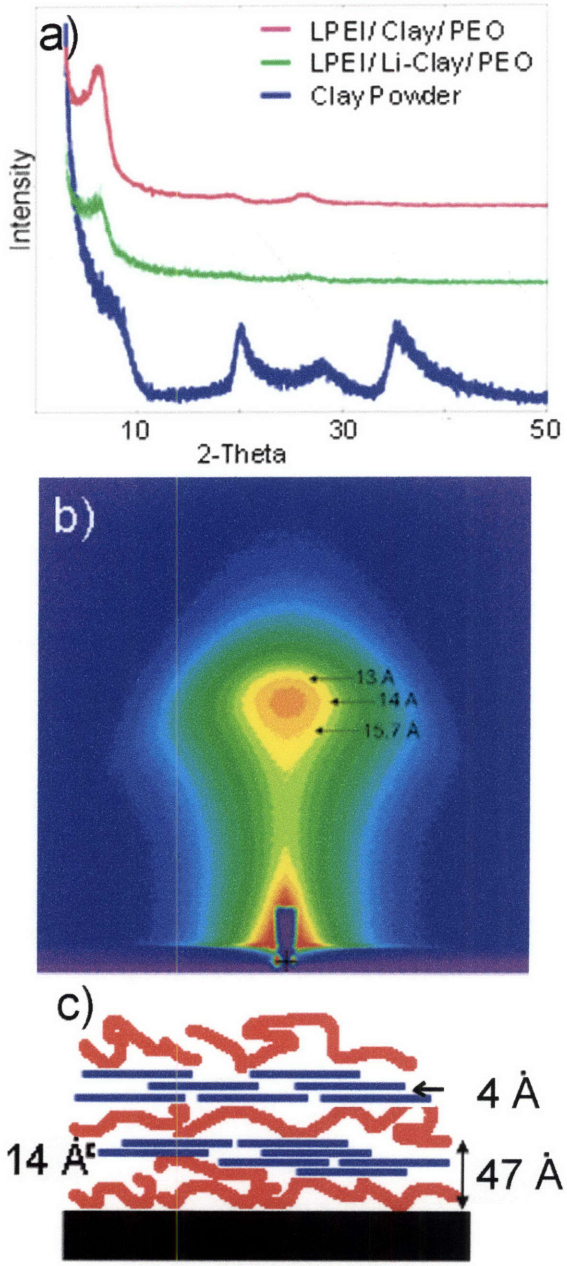

Figure 4-4. WAXD (a) of Laponite clay powder in blue (bottom), PEI/Li-Clay/PEO in green (middle), and PEI/Clay/PEO in pink (top). The shape of the GI-SAXS pattern (b) of PEI/Li-Clay/PEO indicates orientation parallel to the substrate surface. Proposed structure (c) of PEI/Li-Clay/PEO LbL assembly. The trilayer thickness is 47 Å (from growth profile), the basal spacing is 14 Å (from GI-SAXS and WAXD), and the gallery spacing is 4 Å (basal spacing minus clay platelet thickness, 14 Å -10 Å = 4 Å).

4.5 Ionic Conductivity and Anisotropy

Electrochemical impedance spectroscopy (EIS) is a useful tool for investigating the movement and transport of ions (e.g. conductivity) within an electrolyte. Multilayered composites of $(PEI/Li\text{-}Clay/PEO)_{60}$ were probed using EIS to measure ionic conductivity as a function of temperature, humidity and orientation. Both cross-plane and in-plane conductivities were investigated at 53% and 0% relative humidity (RH).

The impedance response of $(PEI/Li\text{-}Clay/PEO)_{60}$ multilayers was measured in two different cells to isolate the cross- and in-plane directions. Cross-plane (z direction) ion transport was measured in a cell consisting of multilayers deposited on patterned ITO glass and gold electrodes evaporated atop the multilayer film; in-plane (x-y direction) ion transport was measured using independently addressable ITO microband electrodes (IAMEs). A typical Nyquist plot for a cross-plane cell (Figure 4-5), gave a depressed semicircle at high frequency and a near-vertical line at lower frequency, which is similar to previous reports of PEO-clay composites;[7] in-plane measurements gave a similar response. This high frequency behavior, previously described,[4, 12] is best modeled using a resistor and constant-phase element (CPE) in parallel, preceded by a resistor and CPE in series to capture low frequency domains (Equivalent Circuit in Figure 4-5). R1 and R2 represent the electrode resistance and multilayer assembly resistance, respectively. CPE1 describes the non-ideal capacitive double layer, most likely caused by a rough electrode-electrolyte interface, and CPE2 corresponds to bulk polarization of the LbL film. To check cell design and self-consistency, samples of varying thickness (200 to 300 nm) were constructed; electrolyte resistance, R2, scaled linearly with thickness, as expected.

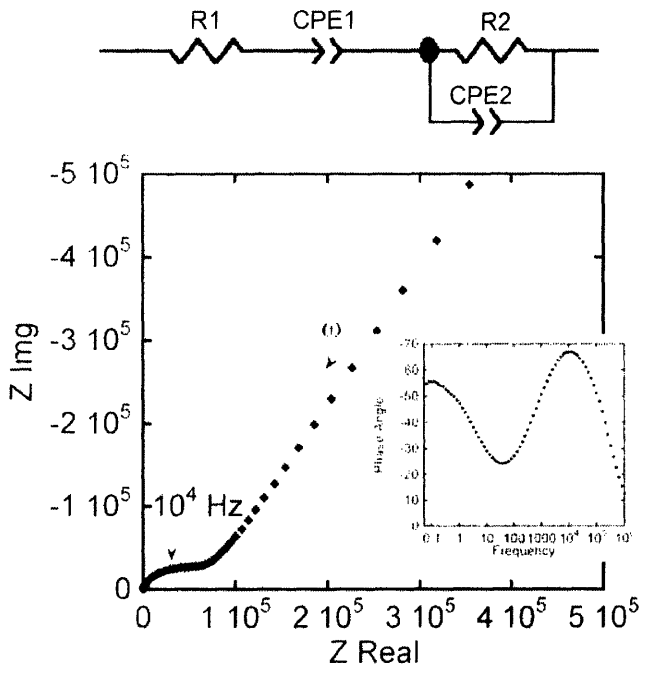

Figure 4-5. A representative Nyquist and Bode (inset) plot of $(PEI/Li\text{-}Clay/PEO)_{60}$ multilayers at 170 °C, cross-plane. Data fit to above model gives an electrolyte resistance (R2) of 62000 Ω. With a cell constant of (L/A) = 0.0045 cm^{-1}, the resulting conductivity is $7.3 \cdot 10^{-9}$ S cm^{-1}. Voltage amplitude was 100 mV, and measurements were performed in a dry, argon-filled glove box.

Given the equivalent circuit, described above, and the impedance response of multilayers at 53% and 0% RH and 25 °C, the in- and cross-plane conductivity (Table 2) was calculated using $\sigma = L/(R2 \cdot A)$, where L is the distance between electrodes and A is the area between electrodes. The ratio of the in- and cross-plane measurements gives the anisotropy factor; films at 53% RH exhibited an anisotropy factor of seven (from Table 4-2). The anisotropy factor for films at 0% RH and 25 °C could not be calculated because in-plane measurements at these conditions exhibited impedance that exceeded the limits of the analyzer. Of note, while electrode resistance (R1) remained constant with increasing humidity, the multilayer resistance (R2) dramatically decreased (i.e. LbL conductivity increased). This behavior can be explained by the presence of water within

the LbL assembly: at 53 % RH, the ionic conductivity is expected to be primarily protonic because water adsorbed along the platelet faces is predominately acidic;[52] however in dry conditions, the solvated cation, Li^+, is considered the mobile species.[6, 7]

Table 4-2. In-plane and cross-Plane Conductivity at 0% and 53% RH

Orientation	σ (S cm^{-1}) at 53% RH	σ (S cm^{-1}) at 0% RH
In-Plane (Z)	$2.6 +/- 0.2 \cdot 10^{-7}$	x
Cross-Plane (X-Y)	$4 +/- 1 \cdot 10^{-8}$	$7 +/- 1 \cdot 10^{-13}$

To further understand ion transport in $(PEI/Li\text{-}Clay/PEO)_{60}$ multilayers in the dry state (0% RH), in- and cross-plane conductivity was measured as a function of temperature (30 to 200 °C). The temperature response of both cross- and in-plane conductivities (Figure 4-5a) exhibited Arrhenius behavior. Results were reproducible from sample to sample with no hysteresis from thermal cycling. Below 115 °C, the impedance of the IAMEs for in-plane measurements exceeded the limits of the analyzer. The activation energy, which is related to the slope of log(σ) vs. 1/T, for in- and cross-plane conductivities was 0.37 and 0.35 eV (36 and 33 kJ/mol), respectively; these numbers compare well with the activation energy of Li^+ in PEO which ranges from 0.2 to 0.3 eV.[53, 54] Alternatively, the activation energy for ion transport in Li^+-Montmorillonite is ~1 eV.[7] Given an observed activation energy of 0.35-0.37 eV, and assuming Laponite behaves similarly to Montmorillonite, we propose that ion transport in (PEI/Li-Clay/PEO) mirrors that of Li^+ transport in PEO. Because both in- and cross-plane activation energies are similar to that of Li^+-PEO, chain segments of PEO may participate in both the cross-plane and in-plane ion transport process as PEO serves to bridge between clay platelets.

Despite the similar in- and cross-plane conduction activation energies, cross-plane conductivity was 100 times less than in-plane conductivity (Figure 4-6a). This is explained by the tortuous path the small lithium ion (r = 0.68 Å) must travel to migrate in the z-direction (Figure 4-6b), weaving around oriented clay platelets (r = 25 nm). Further evidence of a tortuous path is present in differences observed in alpha of the CPE2, Z_{CPE}

$= 1/(Q \cdot (j\omega)^{\alpha})$. The CPE represents a distribution of time constants for ion transport, and the resistive or capacitive character of the response is described by alpha, which ranges between 0 and 1.[55] In-plane measurements were nearly capacitive with alpha = 0.97, meaning there is one mode of ion transport. Cross-plane measurements, alpha = 0.7 to 0.8, were less capacitive in character and pointed to mixed time constants of ion transport. Indeed in the cross-plane, multiple time constants are possible as an ion has many tortuous paths to choose from, whereas with in-plane conduction, ion transport occurs relatively uninterrupted in one direction.

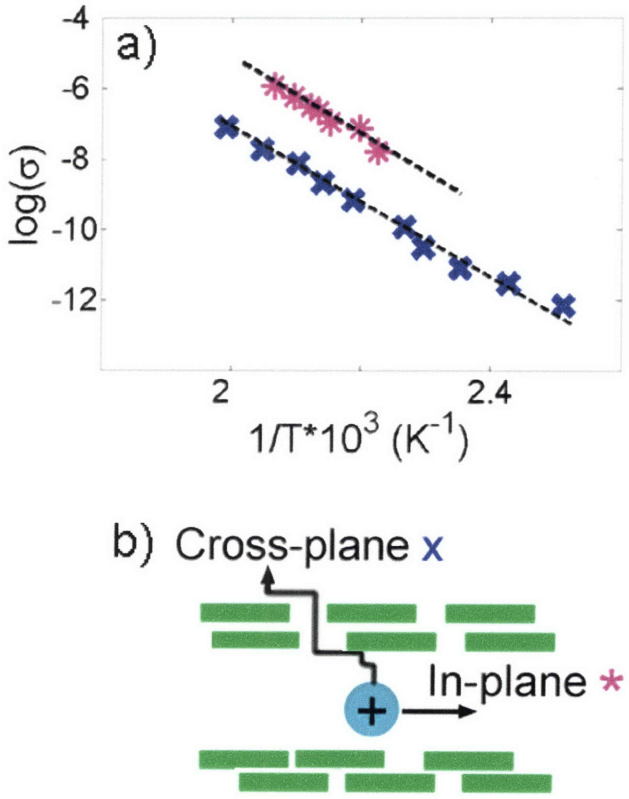

Figure 4-6. (a) Arrhenius plot of the variation of conductivity with temperature from 30 to 200 °C of (PEI/Li-Clay/PEO) assemblies in a dry argon glove box. In-plane conductivity (pink *) is consistently 100 times higher than cross-plane conductivity (blue x). The similar slopes (dashed lines) indicate comparable activation energies of 0.35 and 0.37 eV for cross- and in-plane conductivities, respectively. (b) Cross-plane ion conduction is hindered by the presence of ordered clay nanoplatelets, while in-plane ion conduction is unhindered.

As suggested by Ruiz-Hitsky and others,[6, 13-15] polymer-clay composites are single-ion conductors. The relatively large anionic clay nanoplatelets are virtually immobile compared to the facile lithium ion, yielding an ideal lithium transference number of unity. The LbL films discussed here are potential single-ion conductors, where the lithium cation is solvated by PEI and PEO[24] and charge balanced by negatively charged Laponite clay. However, the transference number of the LbL system could not be measured because a cell of Li|LbL-Film|Li, necessary for this measurement, could not be constructed owing to difficulties in isolating the LbL film. Future efforts aim at resolving the challenge of lifting-off or isolating the film to allow the measurement of the transference number as well the mechanical and transport properties.

4.6 Conclusion

In summary, polymer-clay nanocomposites of PEI, Laponite clay and PEO were constructed using LbL assembly technique; each trilayer was ~5 nm in thickness and clay platelets appeared to lay face-down relative to the substrate. Anisotropic structure of the films was confirmed using multiple techniques (GI-SAXS, WAXD, AFM, SEM). This system is thought to be built upon hydrogen bonding and electrostatic interactions among the three components. Anisotropic ion transport, resulting from anisotropic structure, was investigated using electrochemical impedance spectroscopy, which demonstrated in-plane ionic conductivities 100 times faster than cross-plane conductivities (at 0% RH). The activation energy associated with ion transport in (PEI/Li-Clay/PEO) (0.35 - 0.37 eV) at 0% RH was similar to that of lithium cations in PEO. When humidity was increased from 0% RH to 53% RH, observed cross-plane conductivity increased (from $7 \cdot 10^{-13}$ to $4 \cdot 10^{-8}$ S cm^{-1}, respectively) and the degree of anisotropic transport decreased (from 100 to 7, respectively). With regard to LbL assemblies, this study represents a first correlation of structural anisotropy to transport anisotropy using EIS.

Recommendations for refining the PEI/Clay/PEO system for practical use as an electrolyte include (i) adding a plasticizer such as ethylene carbonate (increasing charge mobility), (ii) adding a Li^+ salt to increase Li^+ concentration, and (iii) creating exfoliated or disorganized LbL films containing polymer electrolyte and Laponite clay (thus

removing the anisotropy). In light of the demonstrated influence on ionic conductivity, the anisotropic structure of this LbL film system may allow introduction of anisotropy in gas permeability or mechanical properties for additional applications.

4.7 References

1. Pinnavaia, T. J.; Beall, G. W., *Polymer-Clay Nanocomposites*. John Wiley & Sons: Chichester, 2000.
2. Struth, B.; Eckle, M.; Decher, G.; Oeser, R.; Simon, P.; Schubert, D. W.; Schmitt, J. *The European Physical Journal E* **2001,** 6, (5), 351-358.
3. Kim, D. W.; Choi, H.-S.; Lee, C.; Blumstein, A.; Kang, Y. *Electrochimica Acta* **2004,** 50, (2-3), 659-662.
4. Aranda, P.; Galvan, J. C.; Casal, B.; Ruiz-Hitsky, E. *Electrochimica Acta* **1992,** 37, (9), 1573-1577.
5. Ghosh, P. K.; Bard, A. J. *Journal of the American Chemical Society* **1983,** 105, (17), 5691-5693.
6. Ruiz-Hitsky, E.; Aranda, P. *Advanced Materials* **1990,** 2, (11), 545-547.
7. Aranda, P.; Ruiz-Hitsky, E. *Chemistry of Materials* **1992,** 4, (6), 1395-1403.
8. Wu, J.; Lerner, M. M. *Chemistry of Materials* **1993,** 5, (6), 835-838.
9. Aranda, P.; Ruiz-Hitsky, E. *Acta Polymerica* **1994,** 45, (2), 59-67.
10. Doeff, M. M.; Reed, J. S. *Solid State Ionics* **1998,** 113-115, 109-115.
11. Chen, H.-W.; Chang, F.-C. *Polymer* **2001,** 42, (24), 9763-9769.
12. Riley, M.; Fedkiw, P. S.; Khan, S. A. *Journal of the Electrochemical Society* **2002,** 149, (6), A667-A674.
13. Walls, H. J.; Riley, M. W.; Singhal, R. R.; Spontak, R. J.; Fedkiw, P. S.; Khan, S. A. *Advanced Functional Materials* **2003,** 13, (9), 710-717.
14. Singhal, R. G.; Capracotta, M. D.; Martin, J. D.; Khan, S. A.; Fedkiw, P. S. *Journal of Power Sources* **2004,** 128, (2), 247-255.
15. Kurian, M.; Galvin, M.; Trapa, P.; Sadoway, D. R.; Mayes, A. M. *Electrochemica Acta* **2005,** 50, 2125-2134.
16. Wong, S.; Vasudevan, S.; Vaia, R. A.; Giannelis, E. P.; Zax, D. B. *Journal of the American Chemical Society* **1995,** 117, (28), 7568-7569.
17. Vaia, R. A.; Vasudevan, S.; Krawiec, W.; Scanlon, L. G.; Giannelis, E. P. *Advanced Materials* **1995,** 7, (2), 154-156.
18. Chen, H.-W.; Chiu, C.-Y.; Chang, F.-C. *Journal of Polymer Science Part B: Polymer Physics* **2002,** 40, (13), 1342-1353.
19. Loyens, W.; Maurer, F. H. J.; Jannasch, P. *Polymer* **2005,** 46, (18), 7334-7335.
20. Manoratne, C. H.; Rajapakse, R. M. G.; Dissanayake, M. A. K. L. *International Journal of Electrochemical Science* **2006,** 1, (1), 32-46.
21. Parfitt, R. L.; Greenland, D. J. *Clay Minerals* **1970,** 8, 305-315.
22. Aray, Y.; Marquez, M.; Rodriguez, J.; Vega, D.; Simon-Manso, Y.; Coll, S.; Gonzalez, C.; Weita, D. A. *Journal of Physical Chemistry B* **2004,** 108, (7), 2418-2424.
23. Tarascon, J.; Armand, M. *Nature* **2001,** 414, 359-367.
24. Gray, F. M.; Royal Society of Chemistry (Great Britain), *Polymer Electrolytes*. Royal Society of Chemistry: Cambridge, 1997; p 175.
25. Kleinfeld, E. R.; Ferguson, G. S. *Science* **1994,** 265, (5170), 370-373.
26. Decher, G.; Hong, J. *Thin Solid Films* **1992,** 210, (1-2), 831.
27. Decher, G. *Science* **1997,** 277, 1232.

28. Stockton, W. B.; Rubner, M. F. *Macromolecules* **1997,** 30, (9), 2717-2725.
29. Wang, L.; Wang, Z.; Zhang, X.; Shen, J.; Chi, L.; Fuchs, H. *Macromolecular Rapid Communications* **1997,** 18, (6), 509-514.
30. Ferguson, G. S.; Kleinfeld, E. R. *Advanced Materials* **1995,** 7, (4), 414-416.
31. Kleinfeld, E. R.; Ferguson, G. S. *Chemistry of Materials* **1995,** 7, (12), 2327-2331.
32. Kleinfeld, E. R.; Ferguson, G. S. *Chemistry of Materials* **1996,** 8, (8), 1575-1578.
33. Lvov, Y.; Ariga, K.; Ichinose, I.; Kunitake, T. *Langmuir* **1996,** 12, (12), 3038-3044.
34. Kotov, N. A.; Haraszti, T.; Turi, L.; Zavala, G.; Geer, R. E.; Dekany, I.; Fendler, J. H. *Journal of the American Chemical Society* **1997,** 119, (29), 6821-6832.
35. Kotov, N. A.; Magonov, S.; Tropsha, E. *Chemistry of Materials* **1998,** 10, (3), 886-895.
36. MacNeill, B. A.; Simmons, G. W.; Ferguson, G. S. *Materials Research Bulletin* **1999,** 34, (3), 455-461.
37. van Duffel, B.; Schoonheydt. *Langmuir* **1999,** 15, (22), 7520-7529.
38. Glinel, K.; Laschewsky, A.; Jonas, A. M. *Macromolecules* **2001,** 34, (15), 5267-5274.
39. Glinel, K.; Laschewsky, A.; Jonas, A. M. *Journal of Physical Chemistry B* **2001,** 106, (43), 11246-11252.
40. Tang, Z.; Kotov, N. A.; Magonov, S.; Ozturk, B. *Nature Materials* **2003,** 2, (6), 413-418.
41. Vuillaume, P. Y.; Glinel, K.; Jonas, A. M.; Laschewsky, A. *Chemistry of Materials* **2003,** 15, (19), 3625-3631.
42. Southern Clay Products Laponite RD Product Bulletin.
43. Roe, R. J., *Methods of X-ray and Neutron Scattering in Polymer Science*. Oxford University Press: New York, 2000.
44. Delongchamp, D. M.; Hammond, P. T. *Chemistry of Materials* **2003,** 15, (5), 1165-1173.
45. DeLongchamp, D. M.; Hammond, P. T. *Langmuir* **2004,** 20, (13), 5403-5411.
46. Jeon, J.; Panchagnula, V.; Pan, J.; Dobrynin, A. V. *Langmuir* **2006,** 22, (10), 4629-4637.
47. Baghdadi, H. A.; Sardinha, H.; Bhatia, S. R. *Journal of Polymer Science Part B: Polymer Physics* **2005,** 43, (2), 233-240.
48. Le Luyer, C.; Lou, L.; Bovier, C.; Plenet, J. C.; Dumas, J. G.; Mugnier, J. *Optical Materials* **2001,** 18, (2), 211-217.
49. Warren, B. E., *X-Ray Diffraction*. Addison-Wesley: Reading, 1969.
50. Busch, P.; Rauscher, M.; Smilgies, D.-M.; Posselt, D.; Papadakis, C. M. *Journal of Applied Crystallography* **2006,** 39, (3), 433-442.
51. Finnigan, B.; Jack, K.; Campbell, K.; Halley, P.; Truss, R.; Casey, P.; Cookson, D.; King, S.; Martin, D. *Macromolecules* **2005,** 38, (17), 7386-7396.
52. Slade, R. C. T.; Barker, J.; Hirst, P. R.; Halstead, T. K. *Solid State Ionics* **1987,** 24, (4), 289-295.
53. Robitaille, C. D.; Fauteux, D. *Journal of the Electrochemical Society* **1986,** 133, (2), 315-325.
54. Chung, S. H.; Jeffrey, K. R.; Stevens, J. R. *Journal of Chemical Physics* **1991,** 94, (3), 1803-1811.

55. Orazem, M. E. In *Impedance Spectroscopy Short Course*, 209th Meeting of the Electrochemical Society, Denver, 2006; The Electrochemical Society: Denver, 2006; p 3:9.

Chapter 5 : Nano- and Micro-Porous LbL Assemblies: Formation, Structure and Transport

Portions of this chapter are reprinted from Lutkenhaus, J. L.; McEnnis, K.; Hammond, P. T. *In Preparation.*

5.1 Introduction

Porous materials and coatings possess excellent qualities (e.g. high surface area, tortuosity) for applications such as separations, drug delivery, catalysis, optics, and tissue scaffolding.[1-4] In a desire to design functional ultra thin porous coatings, key factors such as pore size, porosity, surface roughness and film thickness must be precisely manipulated. A potential means of controlling these factors is based upon the layer-by-layer (LbL) assembly technique, where polyelectrolytes of opposite charge are alternately directed to a surface.[5, 6] The advantages of this methodology are numerous: (1) conformal coatings of challenging geometries are possible, (2) ultra thin films are achievable because the thickness of each film is controlled by the number of LbL cycles (0.5 to 30 nm/cycle), and (3) the properties of each film are finely controlled and tuned by assembly conditions such as pH and ionic strength. Reported applications of porous LbL assemblies include Bragg reflectors,[7] drug delivery,[8] super hydrophobic coatings[9] which may be patterned,[10] anti-reflection coatings,[11] and sacrificial templating.[12, 13] Nano- and micro-porous layer-by-layer assemblies are created using a simple procedure developed by Rubner and coworkers.[14] First, LbL assembly of weak polyelectrolytes (often polyallylamine hydrochloride and polyacrylic acid) is performed under conditions where both polyelectrolytes are partially charged, resulting in smooth and continuous coatings. Following assembly, the LbL film is immersed in a bath of acidic water, and in some cases, the formation of a porous architecture is observed. The porous transition, marked by a significant increase in film thickness and roughness, is thought to be caused by the change in charge density along constituent polyelectrolyte backbones.

In recent work,[15, 16] porous multilayers consisting of linear polyethylene imine (LPEI) and polyacrylic acid (PAA) were described, where these films were used as a porous

support for oligoethylene glycol dicarboxylic acid (OEGDA) electrolyte in a dye-sensitized solar cell. These early reports used partially charged weak polyelectrolytes, both at pH 5.0, which are known to give thick and loopy multilayers (30 nm/cycle).[17] When the LbL films were immersed in water of pH less than 3.0, the thickness nearly tripled and a nano- and micro-porous morphology was observed. At ambient conditions, the reported conductivity of the OEGDA-filled porous LbL assembly was 10^{-6} to 10^{-5} S cm^{-1},[15, 16] which was 10^6 times higher than its *non*-porous counterpart.[17] Using a porous LbL film as a separator has a distinct advantage in that it can be made quite thin (< 1 μm), whereas conventional separators or supports for liquid electrolyte are 25 μm thick.[18] Because conductance is inversely proportional to thickness, thinner materials are desired so as to minimize the internal resistance of the electrolyte layer. Despite the enhancement in conductivity of porous vs. *non*-porous LbL films, the effect of varying assembly and treatment pH upon the pore size, porosity, and surface roughness for LPEI/PAA systems was largely unexplored.

Here, it was desired to understand and control the formation and structure of porous LPEI/PAA multilayers for their potential use as a porous support for non-aqueous electrolyte. In this work, we investigate a range of assembly pH (3 to 6) and post-assembly treatment pH (1.75 to 3.00) to elucidate the pore volume, pore size and surface roughness of LPEI/PAA multilayers. Pore volumes reaching 80 % and pore sizes ranging from tens of nanometers to microns can be achieved by modulating assembly and treatment pH. We propose that the porous transition is attributed to the neutralization of PAA and the ionization of LPEI within the LbL assembly, as suggested by FTIR spectroscopy, where changes in polyelectrolyte charge density ultimately control the extent of electrostatic cross-linkage and the charge build-up within the film. AFM and SEM imaging reveal a variety of structures including nano-porous films, asymmetric membranes, and isolated crater-like micron-scale pores as treatment pH increases from 1.75 to 3.00. To the best of the authors' knowledge, this is the first observation of asymmetric membrane structure in porous LbL assemblies. We also examine the impedance response of *non*-porous and porous LPEI/PAA multilayers, both soaked in a non-aqueous electrolyte. Porous multilayers exhibited two semicircles and two time constants, where as *non*-porous multilayers yielded one. The two time constants were

linked to the presence of two phases (liquid-filled pores and LbL matrix), and two dry state conductivities were calculated (10^{-6} S cm^{-1} and 10^{-9} S cm^{-1}). Structures observed here may be implemented as functional coatings for a variety of future applications.

5.2 Materials and Methods

Solution preparation. 0.02 M poly(ethylene imine) (LPEI) of molecular weight (MW) 25,000 g/mol and 0.02 M linear poly(acrylic acid) (PAA) of MW 90,000 g/mol were made using polymer as received from Polysciences and MilliQ 18 MΩ water. Prior to use, solutions were vacuum-filtered. Polymer solution pH was adjusted to pH 3, 4, 5 or 6 using hydrochloric acid. Solution pH was monitored using Beckman Coulter electrodes that were calibrated within minutes of use and cleaned within one week of use in order to minimize error (+/- 0.01 pH units).

Layer-by-layer film assembly. Films were constructed using a modified programmable Carl Zeiss HMS slide stainer. Immediately before assembly, substrates (silicon, ITO-coated glass) were oxygen plasma treated for two minutes. Silicon substrates were cleaned with piranha solution for five minute (30:70 v/v H_2O_2:H_2SO_4) and rinsed with MilliQ water (*CAUTION: Piranha solution is corrosive and proper personal protective equipment must be worn*). ITO-coated glass substrates were cleaned with 15 minute intervals of sonication in dichloromethane, acetone, methanol and MilliQ water. Immediately after plasma treatment, the substrate was first dipped in pH-adjusted LPEI solution for 15 minutes, rinsed with agitation in MilliQ water for two minutes, followed by two-one minute rinses. Then, the substrate was exposed to pH-adjusted PAA solution for 15 minutes and rinsed as before. Both polyelectrolyte solutions were held at the same pH. Keeping with the convention of Rubner et al.,[14] films assembled at pH *x* will be referred to as *x/x*, where *x* was varied from pH 3 to 6. The procedure was repeated thirty times to give a film of thirty layer pairs. Films were dried with an air-gun and stored in a desiccator filled with phosphorous pentoxide until further treatment. Film thickness was measured using a Tencor P-10 profilometer where the thickness was recorded three times at different locations to yield one data point.

Post-assembly treatment of layer-by-layer films. An as-made film of ($LPEI_x/PAA_x$) was exposed to pH-adjusted MilliQ water of pH 1.75, 2.00, 2.50, 2.75 or 3.00 for twenty minutes, unless otherwise stated. pH adjustment was performed using hydrochloric acid. Immediately following treatment, the film was dipped in MilliQ water for 15 seconds or less. As before, pH electrodes were carefully cleaned and calibrated prior to the treatment step. The resulting film was thermally cross-linked via amidation in a 120 °C convection oven for one hour and stored in a desiccator until further characterization.

AFM. A Dimension 3100 AFM by DI Instruments with a Nanoscope 3A Controller in tapping mode was used to investigate surface morphology of the LbL films on silicon. NCH Pointprobe AFM Cantilevers were purchased from Pacific Nanotechnologies. All films were thirty layer pairs thick. The tip radius of curvature was 10 nm, as indicated by the manufacturer.

SEM. Images were captured using a JEOL-5910 SEM system operating at 2 to 5 keV. 100 Å of Au-Pd was sputter-deposited on the samples prior to imaging to suppress charging. Cross-section images were taken from samples immersed in liquid nitrogen and cleaved with a diamond scribe (i.e. freeze-fractured). Some cross-sectional images were imaged while tilted to improve clarity.

Impedance spectroscopy. Impedance spectroscopy using a Solartron 1260 was performed on a solid state LbL cell for cross-plane (z-direction) measurements. The construction of the cell is described elsewhere by DeLongchamp and Hammond.[17] Briefly, an LbL film was constructed on a substrate of ITO-coated glass, and then the post-assembly treatment step was applied. Patterned gold electrodes, 100 nm thick and 2 mm wide, were then thermally evaporated using an Edwards Auto 306 at 0.08 nm per second. Copper tape from 3M was applied to the gold to form a contact pad. The active area was 6 mm^2, and the LbL film consisted of 30 layer pairs. Following gold evaporation, the edge of the LbL-coated ITO slide was immersed in a dish of electrolyte (1 M $LiPF_6$ in 1:1 v/v ethylene carbonate : dimethyl carbonate), and the electrolyte was allowed to wick into the film, similar to a technique reported by Berg.[8] The conductivity

of the liquid electrolyte was 8.2 mS cm^{-1}, as measured by a liquid conductivity meter calibrated using potassium chloride. An argon-filled glove box with ~2 ppm water was used for impedance measurements in the dry state. A.C. amplitude was 100 mV to improve the signal to noise ratio at high impedance. A linear sweep of the LbL assembly from -100 to 100 mV gave a linear current response, confirming that impedance measurements at this amplitude are appropriate.

5.3 Porosity and Surface Roughness

To explore conditions under which the porous morphology is formed from multilayers of LPEI and PAA, two parameters are investigated: assembly pH (3 to 6) and post-assembly treatment pH (1.75 to 3). Keeping with the convention of Rubner et al.,[14] Films assembled at pH *x* will be referred to as "*x/x*" LbL films; for example a film assembled at pH 4 will be called "*4.0/4.0*". Following assembly, LbL films of (LPEI/PAA) were immersed in acidic water for twenty minutes; as a control, a separate set of untreated films were reserved. This immersion in acidic water will be referred to as the "post-assembly treatment" step. Treated samples were thermally cross-linked following the post-assembly treatment step, where partial amidation of LPEI and PAA occurs above 115 °C.[19] Figure 5-1 describes the materials used and the pore-formation procedure. The film thickness of each system was recorded using profilometry before and after the acidic treatment step and subsequent amidation. Given previous work with LbL films of PAH and PAA,[14] film thickness is expected to increase when transitioning from a continuous to a microporous LbL film. Films assembled at pH 6 were so thin (< 10 nm) that profilometry could not be used; additionally, ellipsometry yielded thicknesses with large sample-to-sample deviation. For this reason, films assembled between pH 3 and 5 are presented. The thickness of each system was measured before (t_{before}) and after (t_{after}) the post-assembly treatment step. Following the acidic treatment step, an increase in film thickness (t) was often observed; this increase may be used to calculate the pore (or void) volume as $100*(t_{after} - t_{before})/t_{after}$, assuming no change in mass.[14] Figure 5-2a describes the pH-dependency of pore volume within various (LPEI/PAA) LbL systems. Films assembled at pH 3 did not exhibit any significant change in thickness regardless of post-assembly treatment pH (i.e. Pore Volume ~ 0 %), but for those assembled at pH 4 or 5,

film thickness doubled or tripled in increasingly extreme treatment conditions. Maximum pore volumes of 57 % and 77 % occurred when LPEI/PAA was assembled at pH 4 and 5, respectively, and was treated at pH 2.25. Pore volume decreases below treatment pH 2, and below pH 1.75, the film delaminates from its silicon substrate. Above treatment pH 3, the pore volume is negligible (~ 0 %). Visually, films treated at pH 2.5 and below were opaque while those above 2.75 were optically clear.

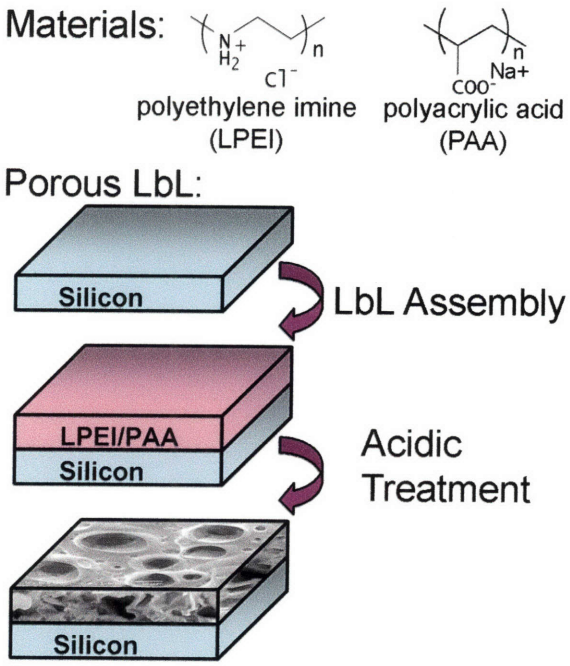

Figure 5-1. Porous LbL assemblies are created in a two-step procedure. First, LbL assembly is performed on a silicon (or ITO-coated glass) substrate, and then the LbL thin film is immersed in acidic water. Polyelectrolytes used in this study, LPEI and PAA, are capable of being partially or fully charged depending on assembly or treatment pH.

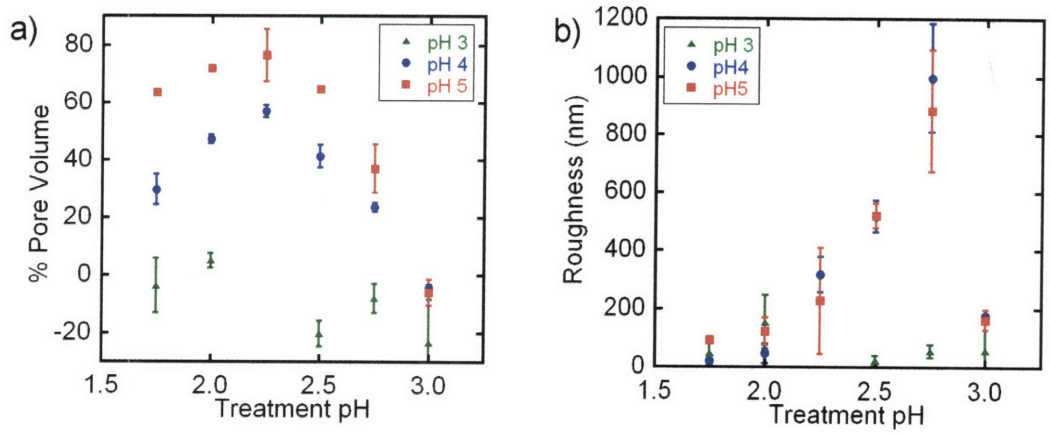

Figure 5-2. Pore volume (a) and surface roughness (b) of (LPEI/PAA) multilayers assembled at pH 3-5 and post-assembly treated at pH 1.75-3.00. Thickness and roughness were measured using profilometry of dry LbL films. Pore volume was calculated using $100*(t_{after} - t_{before})/t_{after}$,[14] described above.

In a similar study,[14] multilayers of PAH and PAA were immersed in acidic solution, and an increase in thickness or porosity was also observed. The maximum reported pore volume for PAH/PAA systems was 66 %,[14] when PAA and PAH assembly pH was 3.5 and 7.5, respectively, and immersion pH was 2.4. At these assembly conditions, assembled PAH/PAA multilayers produced the thickest layer pairs.[14] Similarly, the most porous LPEI/PAA multilayer systems were produced from conditions (assembly pH = 4 or 5) which yielded the thickest layers (30 nm per layer pair).[17] Also at these conditions, LPEI is known to be mobile within the layer-by-layer film, as it is capable of exchange and internal diffusion.[20, 21]

The root-mean square (RMS) surface roughness of each (LPEI/PAA) film was measured after the post-assembly treatment step (Figure 5-2b). Though untreated control samples were uniformly smooth (4 nm +/- 2 nm), the surface roughness of films treated with acidic solution was 5 to 250 times higher. Films assembled at pH 3 were 50 to 150 nm rough, though response appeared independent of treatment pH; in contrast, the roughness of films assembled at pH 4 and 5 increased with increasing treatment pH, reaching nearly 1 micrometer RMS roughness at assembly pH 2.75. All films treated at pH 3 exhibited roughness less than 200 nm.

Given the porosity and roughness responses observed after twenty minutes of acidic treatment (Figure 5-2), the effect of time is considered an important parameter. Using optical microscopy and profilometry, surface morphology, porosity and roughness were monitored as a function of treatment time (Figure 5-3). Untreated *5.0/5.0* films appear smooth and featureless (0 min.), whereas after five minutes of exposure to pH 2.75 water, isolated micron-scale pores appear and surface roughness and pore volume increase. As exposure time further increases, the number of pores increases until they merge together after 20 minutes. Pore volume and roughness climbs to 29 % and 900 nm, respectively. In this particular system, the effect of longer exposure times is unexplored, though volume and roughness data indicates that further structural change is possible. This is in contrast to Tokuhisa and Lowman's findings,[15, 16] where twenty minutes of treatment at pH 3 was sufficient for a complete porous transition; however in that study the transition was monitored by the inclusion of OEGDA via FTIR (not thickness or pore volume as was measured here). Also in these previous studies,[15, 16] OEGDA was added to the pH-adjusted treatment bath, whereas experiments performed here do not use OEGDA.

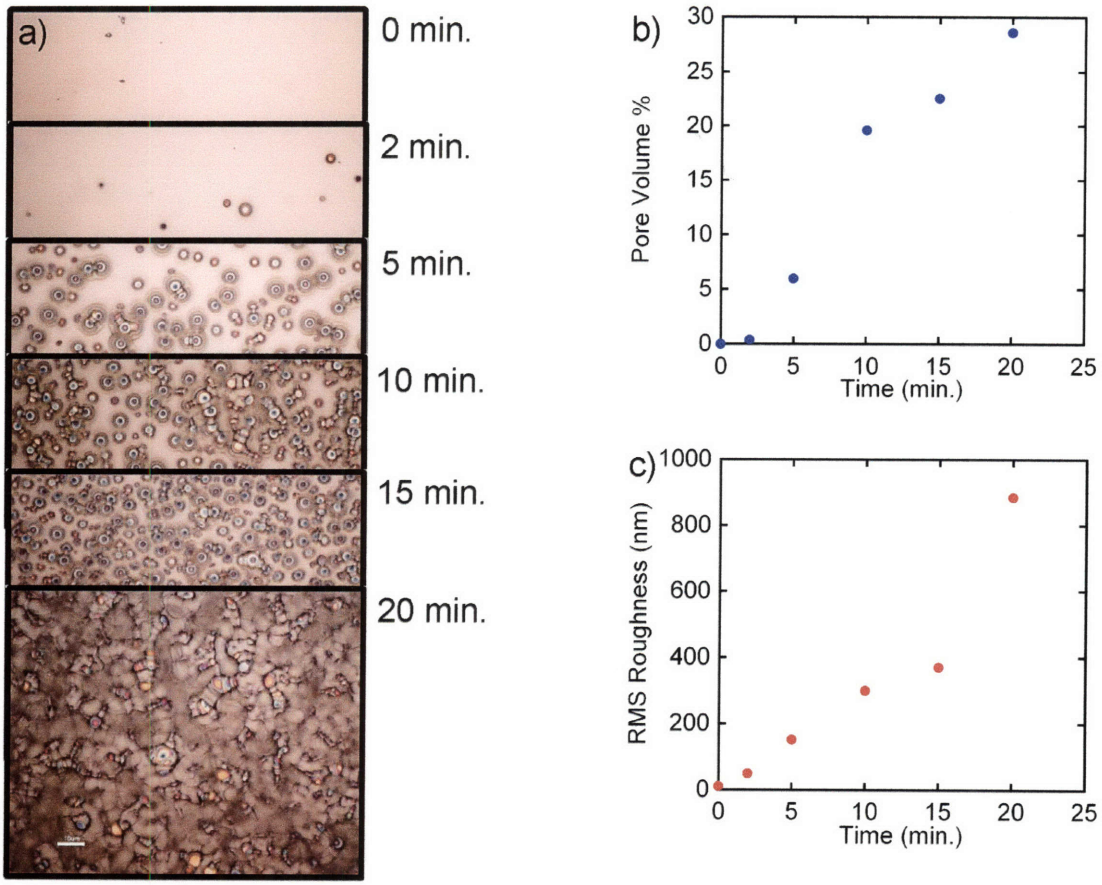

Figure 5-3. Optical microscopy (a) of dried *5.0/5.0* multilayers that had been treated in pH 2.75 water for various exposure times. The porosity (b) and surface roughness (c) also changes with time, as measured using profilometry.

A similar experiment was performed for *5.0/5.0* LbL films treated at pH 2, where the pore volume was tracked for six hours of exposure. Here, the bulk of the porous transition occurs in the first two minutes of exposure. Pore volume jumps to ~72 % after two minutes of treatment and remains constant even after six hours. From optical microscopy (not shown) the surface remains smooth for all exposure times. The difference in time response between pH 2 and pH 2.75 treatments (Figure 5-3b and Figure 5-4, respectively) suggests that the formation of porous structure may occur via different means with respect to treatment pH, and is a subject of further study.

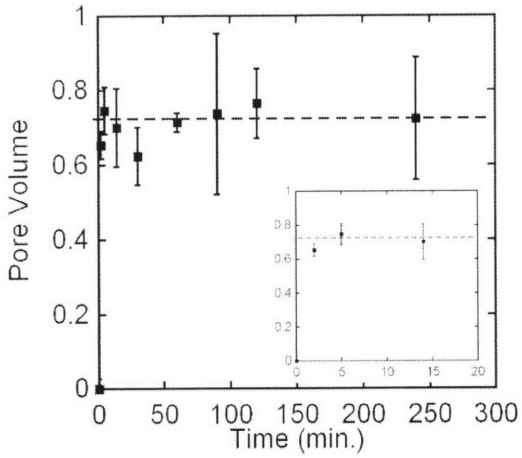

Figure 5-4. Pore volume of dried *5.0/5.0* LbL films that had been treated at pH 2 for zero to six hours. The porous transition appears to occur during the first two to five minutes of treatment (inset); after which, pore volume remains constant at 72 %.

5.4 FTIR Spectroscopy

To further understand the role of electrostatic interactions and the ionization of polyelectrolytes within the LbL film, FTIR spectroscopy of (LPEI/PAA) LbL films atop an IR-transparent silicon substrate in a nitrogen-purged environment was performed. LbL multilayers assembled at pH 4 and 5 were both investigated, but for brevity, only assembly pH 5 is shown, Figure 5-5a. For all systems, three peaks (1715, 1603 and 1560 cm^{-1}) were observed in the region investigated (1500 to 1900 cm^{-1}). The peak at 1603 cm^{-1} corresponds to a secondary amine,[20, 22] the broad peak at 1715 cm^{-1} is attributed to neutral PAA (COOH) which may be present in its "dimerized" or "free" state, (1710 or 1740 cm^{-1}, respectively),[22, 23] and the peak observed at 1560 cm^{-1} suggests that some amount of PAA is ionized (COO^-).[22, 24] Qualitatively, COO^- (COOH) peak absorbance increases (decreases) as post-assembly treatment pH increases from 1.75 to 3.00. Also, the FTIR spectra of an untreated film of *5.0/5.0* appeared similar to that of a film treated at pH 3.00. Assuming that COO^- and COOH peaks have similar extinction coefficients,[25] the fraction of ionized PAA monomer units was calculated using $Abs_{1560}/(Abs_{1715}+Abs_{1560})$.[26] Performing the calculation for systems assembled at pH 4 or 5 (Figure 5-5b), PAA ionization within LbL films ranges from 30 to 54 % or 33 to 55 %,

respectively, for post-assembly pH 1.75 to 3.00. For comparison, PAA within an untreated film assembled at pH 4 or 5 is 54 or 55 % ionized, respectively. In brief, when the acidity of the immersion step increases (pH decreases), PAA becomes more neutralized (ionization decreases).

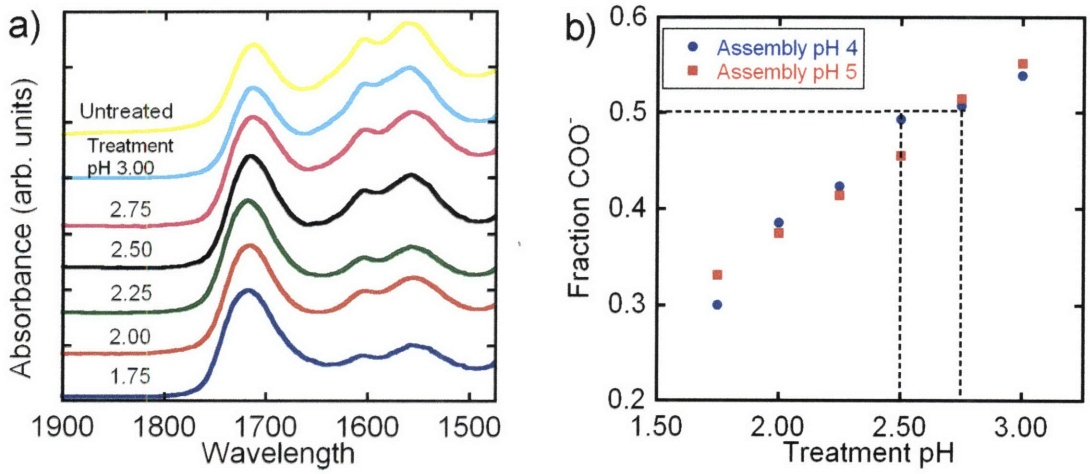

Figure 5-5. FTIR spectra (a) of *5.0/5.0* multilayers treated at varying pH. The fraction of COO^- (b) was calculated from the absorbance bands at 1560 and 1715 cm^{-1} of LbL films assembled at pH 4 or 5 and treated at varying pH. The tie-lines emphasize the $pK_{1/2}$ of PAA, where 50 % of PAA monomer units are charged near post-assembly treatment pH 2.5 or 2.75.

Of note, as determined by Choi and coworkers,[26] the $pK_{1/2}$ of PAA in solution (pH = 5.5 - 6.5) and in an LbL film (pH = 2.2 - 3.0) are known to differ depending on the choice of complementary polycation, where $pK_{1/2}$ is the point at which 50 % of the polymer is ionized. The depression of the pK_a or $pK_{1/2}$ of PAA within multilayer films has also been reported elsewhere.[27, 28] This behavior is attributed to favorable electrostatic interactions, where PAA further ionizes in the presence of basic polycations, depressing the $pK_{1/2}$. In this work, the estimated $pK_{1/2}$ of PAA within LPEI/PAA multilayers is 2.5 to 2.75, as emphasized by the tie-lines in Figure 5-5b.

Seeking to implement a similar analysis to that of PAA, the ionization and neutralization of neat solution-cast LPEI from pH 2 to 6 was investigated (Figure 5-6). With increasing pH, two peaks emerge (1605 and 1450 cm^{-1}), which may be attributed to

NH deformation.[22] Unfortunately within the LPEI/PAA multilayer film, quantifying the role of LPEI proved difficult, because the peaks of interest overlap with that of PAA. However, the second peak observed in Figure 5-5a (1603 cm^{-1}) coincides with that of LPEI alone, confirming its presence within the multilayer film.

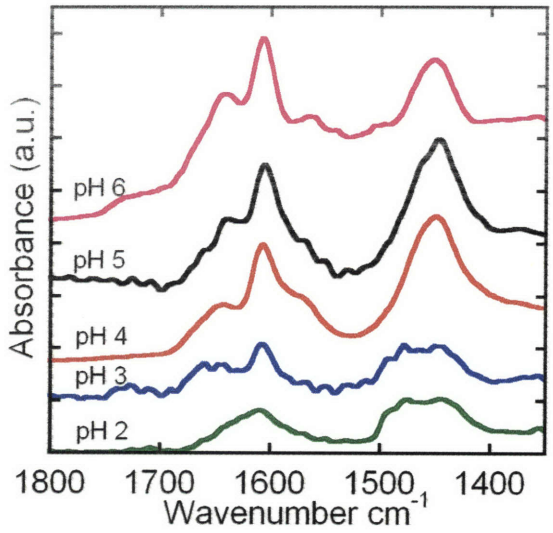

Figure 5-6. FTIR spectra of solution-cast LPEI at various pH on IR-transparent silicon in a nitrogen-purged environment. As pH increases, two distinct features emerge at 1605 and 1450 cm^{-1}.

Given the pH-stimulated response of LPEI/PAA LbL multilayers, we hypothesize that the change in thickness, or the degree of pore formation, is linked to changes in charge density of LPEI and PAA: both being weak polyelectrolytes, LPEI and PAA will ionize and deionize readily in response to localized pH. At pH 4 and 5, pure-component solutions of LPEI and PAA are known to be partially charged (solution $pK_{1/2}$ = 6 and 5.5 – 6.5, respectively)[26, 29, 30] and LbL assemblies of LPEI and PAA constructed under these conditions yield loopy, lightly cross-linked films.[17] When the LbL film is immersed in acidic solution (i.e. treated at pH < 3), the protonic environment neutralizes PAA and ionizes LPEI. The stability of this electrostatically cross-linked film becomes compromised, as cross-links are disrupted (via the neutralization of PAA) and excess positive charge accumulates (via the ionization of LPEI). To accommodate these changes, morphological rearrangement results in a porous and void-filled structure.[14] In

more extreme cases, when treatment pH < 2, excess rearrangement leads to the deconstruction or delamination of the LbL film. A similar mechanism is proposed for microporous PAH/PAA systems.[14] Of note, the deconstruction of films at pH < 2 conflicts with the assumption of constant mass in calculating pore volume. Under these conditions, the real pore volume is expected to be greater than values estimated from the equation described in the previous section, % pore volume = $100*(t_{after} - t_{before})/t_{after}$. If mass is lost, the thickness before the transition (t_{before}) is superficially high, as it also represents mass of film that is not present post-assembly treatment. If t_{before} is too high, then the pore volume estimated using the previously described equation may be lower than the "real" value.

We also investigated whether the porous transition in LPEI/PAA films was reversible, as had been reported for PAH/PAA LbL systems.[11] (LPEI/PAA) multilayers, assembled at pH 4, were immersed in water of pH 2 and dried with high velocity air; then, the porous film was immersed in MilliQ water (~ pH 5.5) for varying amounts of time (2 minutes to 1 hour). These alternating immersion steps were repeated three times, and the thickness and surface morphology of the film following each step was studied using profilometry and AFM (not shown). We would expect the thickness to increase or decrease with the creation or deconstruction, respectively, of the porous architecture; however, results indicate that the transition is not reversible, where no significant change in film thickness (+/- 5 %) or surface morphology was observed. Of note, the thermal cross-linking step was omitted in this particular segment of the study.

5.5 Microscopy

Tapping mode AFM was performed upon (LPEI/PAA) films to characterize the surface structure before and after post-assembly treatment (Figure 5-7). Height images of untreated LbL films assembled at pH 4 and 5 appear smooth (4 +/- 2 nm), while treatment with acidic solution changes the surface of the film dramatically. Observed features include isolated pores less than 100 nm in diameter (pH 2), rough and mottled bumps (pH 2.5 and 2.75), and isolated crater-like micron-scale pores (pH 3). Images obtained for treatment pH 1.75 were difficult to analyze for pore size owing to the radius of curvature of the probe tip (~10 nm). In general, feature size increases with increasing

treatment pH. Recall from roughness measurements (Figure 5-2b), films assembled at pH 2.5 and 2.75 were the roughest (~1 micrometer) among the sample set; the observed surface morphology and roughness at these conditions suggests possible competition or transition between nano- and micro- scale features. Also of note, in two cases (assembly pH 3 and 6, not shown), no evidence of pore formation was observed upon acidic treatment: the surface remained smooth and featureless, identical to control samples.

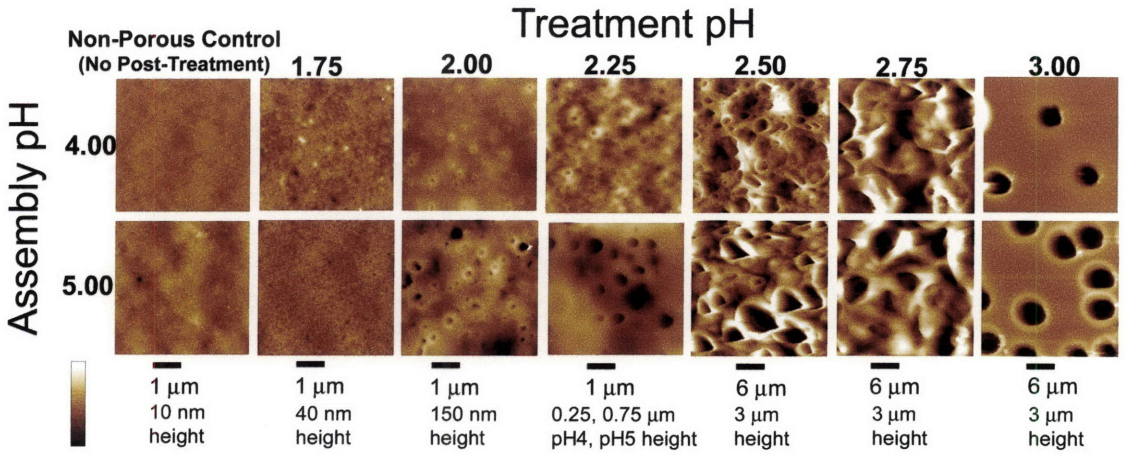

Figure 5-7. Tapping mode atomic force microscopy height images of (LPEI/PAA) multilayers assembled at pH 4 or 5 and treated at varying pH. Non-porous control samples were left untreated. Pore sizes range from tens of nanometers to ~5 micrometers.

To complement findings from AFM, optical microscopy was used to observe the surface features of (LPEI/PAA) multilayers (Figure 5-8). Only micron-scale features are visible using this technique, but features for films assembled at pH 4 and 5 are visible when treatment pH is greater than 2.5. Also, no features were observed for systems assembled at pH 3 or 6.

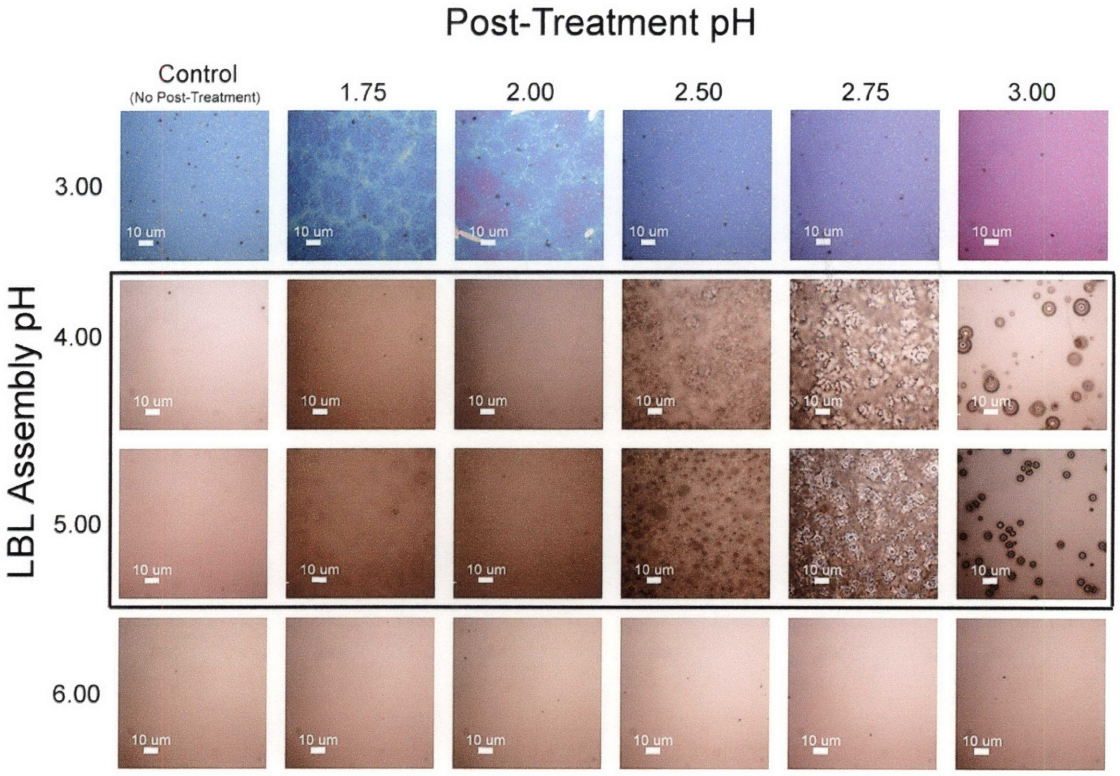

Figure 5-8. Optical microscopy of (LPEI/PAA) multilayers assembled at pH 3-6 and treated at pH 1.75 to 3.00. Control samples have not been exposed to acidic solution. Samples investigated using AFM (Figure 5-7) are included in the black box.

The structure of the microporous LbL films was further investigated using top-down and cross-section SEM of LPEI/PAA assembled at pH 5 and treated at various pH (Figure 5-9). As before, a range of architectures is observed. Films treated at pH 1.75 yield nanoporous morphology, though images gathered here are not sufficient to determine pore size, and surface images suggest stress-related wrinkling: recall that at this condition, the film tends to delaminate from its substrate. Films treated at pH 2 give an interesting heterogeneous structure, comprised of two distinct regions with different pore length scales. Treatment pH 2.25 gives a highly porous structure (77 %, from Figure 5-2a), treatment pH 2.50 and 2.75 appear to possess a collapsed structure, and those treated at pH 3 have isolated, crater-like pores about 5 micrometers in diameter.

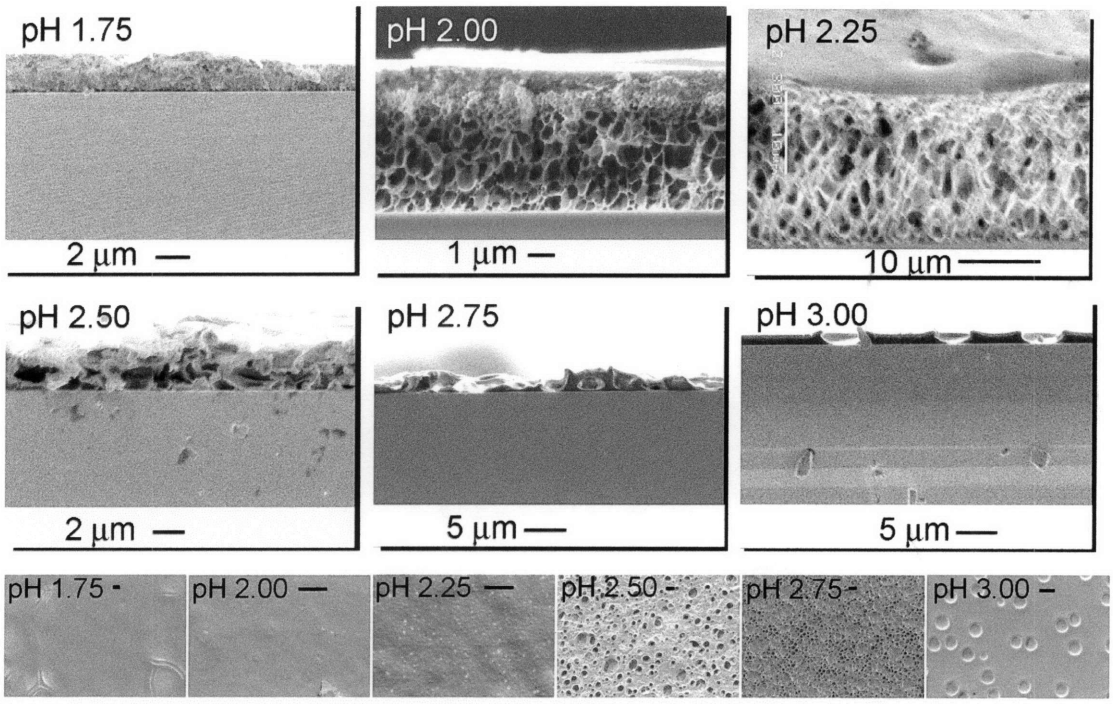

Figure 5-9. SEM cross-section (upper two rows) and top-down images (bottom row) of *5.0/5.0* multilayers treated at varying pH. Conditions are 2 to 5 keV. Top-down image scale bars are 5 micrometers. Samples were coated with 100 Å of AU-Pd.

The structure created and observed from treatment at pH 2 and 2.25 is of particular interest, and appears similar to a phase inversion or asymmetric membrane, a structure that is useful for filtration and drug delivery applications.[31, 32] To the best of the authors' knowledge, this structure has yet to be reported for LbL films. At pH 2 the dense, nanoporous region (top layer) appears to have a relatively smooth skin (120 nm RMS roughness) with pin-holes ~100 nm in size (from AFM, Figure 5-7); the bottom region, at the substrate-LbL interface, is microporous. Also, recall that this combination of treatment and assembly conditions also yielded a high pore volume (72 %).

5.6 Ionic Conductivity and Impedance Spectroscopy

It was desired to use the observed structures as porous supports for a non-aqueous liquid electrolyte. Using impedance spectroscopy, we expect to observe different modes of ion transport and to determine the conductivity of the porous, liquid-filled LbL structure. The *5.0/5.0* LbL films were assembled atop patterned ITO-coated glass

substrates and treated at varying assembly pH as described before. Following thermal cross-linking, gold electrodes were evaporated atop the LbL film to yield an ITO|LbL|Au cell. The edge of the cell was placed in a shallow dish of electrolyte comprised of 1:1 v/v ethylene carbonate:dimethyl carbonate and 0.3 M lithium hexafluorophosphate ($LiPF_6$), where the measured electrolyte conductivity was 8.2 mS cm^{-1}. Nano- and microporous LbL films will readily uptake solution, where progress may be monitored visually.[8] The electrolyte was able to wick up to 1 cm in height into the film, and the film changed in optical clarity (from opaque to clear).

Impedance spectroscopy in a dry, argon-filled glove box was performed on each system, as well as a *non*-porous control. Typical responses for both electrolyte-treated systems are described by the Nyquist and Bode plots (Figure 5-10a and 5-10b, respectively). In the Nyquist plot, the *non*-porous LbL film yields a single semi-circle whereas the porous film gives two. Similarly in the Bode plot, the *non*-porous LbL film exhibits a single time constant, or peak frequency (10^4 Hz), while the porous film gives two ($8 \cdot 10^4$ and 8 Hz). These impedance responses may be modeled by two different equivalent circuits. The *non*-porous LbL response is akin to that of a polymer electrolyte,[17, 33] where the equivalent circuit for the LbL system consists of a resistor (R_1) and constant-phase element (CPE_1) in series and then a resistor (R_2) and constant-phase element (CPE_2) in parallel (Figure 5-10c). R_1 stands for the resistance of the wires and electrodes; CPE_1, an imperfect electrode-electrolyte double layer; R_2, the resistance of the electrolyte; and CPE_2, bulk polarization of the LbL film. The conductivity (σ) of the *non*-porous LbL film is given by $\sigma = L/R_2 \cdot A$, where L is the thickness of the film and A is the area between active electrodes. For a porous, liquid-filled LbL film, the impedance response is slightly different, suggesting that the equivalent circuit be modified (Figure 5-10d). To capture the second observed semi-circle, or time constant, a second parallel circuit containing a resistor (R_3) and constant-phase element (CPE_3) was added to the originally proposed equivalent circuit. We propose that both R_2 and R_3 represent the resistance of the composite electrolyte, though each resistance may be attributed to a different mode (or phase) of ion transport. Given two observed electrolyte resistances, two conductivities were calculated: $\sigma_1 = L/R_2 \cdot A$ and $\sigma_2 = L/R_3 \cdot A$. Considering the pore volume, v, the conductivities of porous LbL multilayers may be also be represented as

$\sigma_1 = L/R_2 \cdot Av$ and $\sigma_2 = L/R_3 \cdot A(1-v)$,[34] but this relationship may be inaccurate because of limiting assumptions in calculating pore volume. For this reason, the former equations are used in calculations.

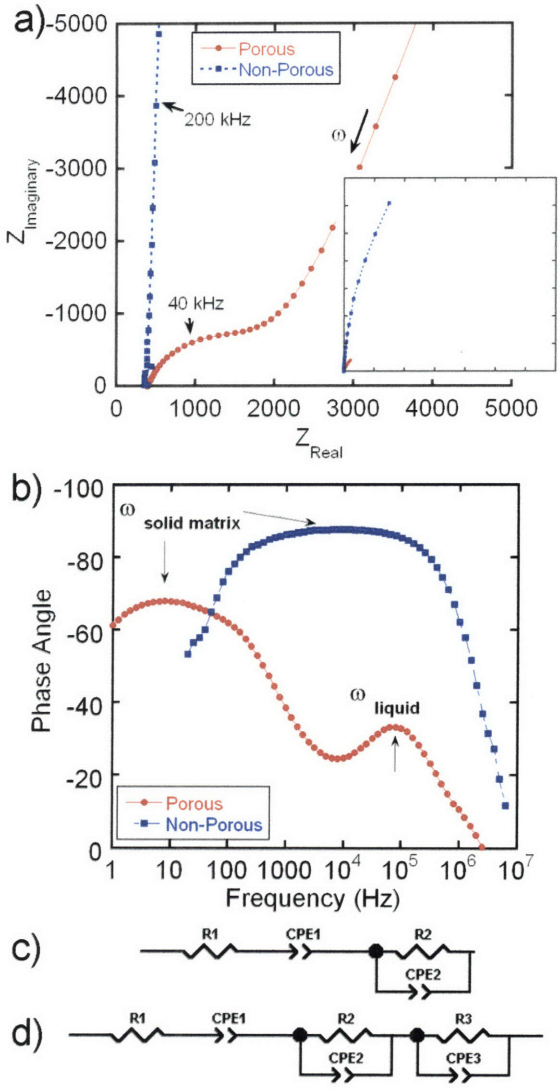

Figure 5-10. Nyquist (a) and Bode (b) plots of porous and *non*-porous *5.0/5.0* multilayers, both exposed to electrolyte. Porous films exhibit two time constants, whereas non-porous film yield one. Equivalent circuits (c) and (d) describe the impedance response of the *non*-porous and porous films, respectively.

The conductivities of *non*-porous and various porous *5.0/5.0* LbL systems are summarized in Figure 5-11. The *non*-porous system soaked in electrolyte, or the control, yielded a single conductivity of 2.3 +/- 0.2 · 10^{-9} S cm^{-1}; in contrast, porous electrolyte-treated systems demonstrated two conductivities, ~10^{-6} and 10^{-9} to 10^{-10} S cm^{-1}. The highest observed conductivity, 1.5 +/- 0.8 10^{-6} S cm^{-1}, occurred at post-assembly treatment pH 2, which was 72 % porous.

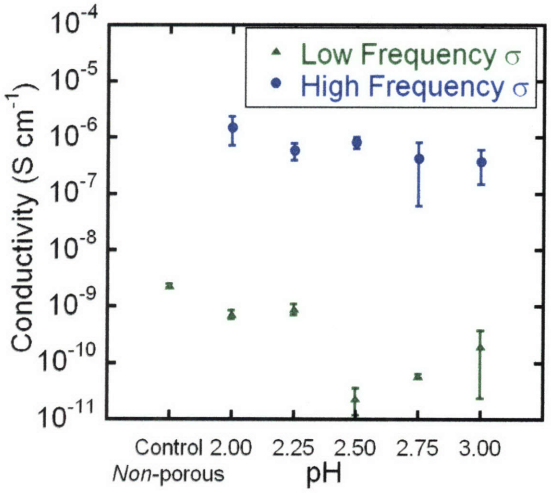

Figure 5-11. Conductivity of electrolyte-filled porous *5.0/5.0* multilayers treated at varying pH. The control is a *non*-porous *5.0/5.0* film exposed to electrolyte. Here, conductivity was calculated from R_2 and R_3, which was estimated using the equivalent circuits described above.

We hypothesize that the two conductivities observed in porous, liquid-filled multilayers are each attributed to transport in separate phases: the higher conductivity (10^{-6} S cm^{-1}) is linked to ion transport within the liquid-filled pores (i.e. "liquid-like"), and the lower conductivity (~10^{-9} S cm^{-1}) is attributed to transport through the solid matrix (i.e. "solid like"). The latter hypothesis is further supported by considering that the lower conductivity in porous multilayers is comparable to that observed in the *non*-porous electrolyte-soaked control. A similar impedance spectra and equivalent circuit was reported for porous sulfonated polysulfone membranes, where two semicircles were separately attributed to the conductivity of the electrolyte and the membrane.[35] Also in membranes with a skin layer, others have attributed the two relaxations to ion transport in

the skin layer and the microporous sublayer.[36] And finally in the case of poor wetting, electrolyte-filled conventional porous separators such as Celgard® will exhibit two semicircles, i.e. "one at higher frequencies corresponding to the bulk electrolyte impedance and the other at lower frequencies related to the interfacial impedance".[37]

The observed behavior and conductivity of *non*-porous *5.0/5.0* multilayers is similar to results described by DeLongchamp.[17] In this work, a dry (0 % RH) conductivity of 2.3 +/- 0.2 · 10^{-9} S cm^{-1} was observed for *5.0/5.0* multilayers soaked in electrolyte, which is an 80-fold improvement over reported neat *5.0/5.0* multilayers without electrolyte, σ = 2.8 +/- 0.2 · 10^{-11} S cm^{-1}, (17 % RH).[17] We attribute this increase to the addition of liquid electrolyte which is thought to plasticize the *non*-porous LbL film (improving the mobility of the charge carrier) and to dope the matrix with lithium cations (increasing the number of charge carriers).

As for the porous, liquid-filled multilayers, the value of the high-frequency conductivity presents an interesting paradox: the conductivity of the liquid electrolyte alone is 8.2 mS/cm, but the high-frequency conductivity observed in porous multilayers is 1000 times lower. A few possible explanations may address this discrepancy. Recall that conductivity was calculated using a cell constant derived from the distance between the electrodes, L, and the area of the electrodes, A. However, this assumption may fail if the real path length, L_{Real}, is tortuous[38] or if the effective area, A_{Real}, is limited by the presence of a nanoporous "skin." If $L_{real} > L$ and if $A_{real} < A$, then the real, high-frequency conductivity may be considerably higher than values presented in Figure 5-11; for example, if the path is ten times longer than L and the area of pore-electrode contact is ten times smaller than A, then the real conductivity is 100 times higher. Another explanation is that the non-aqueous liquid electrolyte may not fully wet the LbL matrix, which may prevent the porous support from being fully filled. Also of note, the observed high-frequency conductivity (10^{-6} S cm^{-1}, 0 % humidity) is lower than Lowman and Tokuhisa's OEGDA-filled porous multilayers (10^{-5} S cm^{-1}, 22 % humidity), though their measurements were performed in ambient conditions where absorbed atmospheric water improves conductivity.

5.7 Conclusion

In summary, the origin and modulation of the porous transition of polyethylene imine/polyacrylic acid multilayers was investigated. Films assembled at pH 4 or 5 were capable of creating a porous structure, whereas pore formation was hindered at assembly pH 3. This observation suggested that the conformation or structure of the multilayer played a key role in the porous transition. At assembly pH 4 or 5, LPEI and PAA in solution are both partially charged, yielding lightly cross-linked, loopy multilayers (before acidic treatment); at assembly pH 3, the charge density of LPEI in solution increases, and heavily cross-linked multilayers result. Porous structure results from acidic treatment in pH range 1.75 to 3.00, where maximum pore volume was 77 % at treatment pH 2.25 and assembly pH 5. Below post-assembly treatment pH 1.75, LbL films were deconstructed as they delaminated from the substrate, and above pH 3.00, pore formation was not observed. In short, the "window" for creating porous structure is assembly pH 4 to 5 and post-assembly treatment pH 1.75 to 3.00. Using FTIR, the porous transition was linked to neutralization of PAA and ionization of LPEI, which disrupts electrostatic cross-links and causes electrostatic repulsion. Also, the $pK_{1/2}$ of PAA (~2.5) was found to be significantly suppressed within the LbL film. From AFM and SEM, pore size varied from tens of nanometers to microns as treatment pH increased from 1.75 to 3.00. Of interest, an asymmetric membrane structure was reproducibly observed with treatment pH 2.00. The origin or formation mechanism for this particular membrane is not well understood and is a subject of future research. Regardless, the observed asymmetry may be of use in filtration, drug delivery or catalysis applications.

To demonstrate its potential use as an ultra thin separator or support, porous *5.0/5.0* multilayers where immersed in a non-aqueous electrolyte cocktail to yield a liquid-filled porous matrix (3 to 10 μm thick). Conventional separator are 25 μm in thickness,[18] and preliminary results indicate that porous (LPEI/PAA) LbL films may be produced as thin as 1 μm. Impedance spectroscopy revealed two time constants, indicative of two modes (or two phases) of ion transport. The high-frequency conductivity, 10^{-6} S cm^{-1}, was attributed to ion transport in the liquid-filled pores, and the low frequency conductivity, 10^{-9} S cm^{-1}, was linked to the LbL matrix. Potential means of improving conductance include using different electrolytes or creating thinner LbL films. Structures described in

this work provide a guide to modulating and controlling pore size, surface area, roughness and transport in porous LbL thin films from weak polyelectrolytes.

5.8 References

1. Stein, A.; Melde, B. J.; Schroden, R. C. *Advanced Materials* **2000,** 12, (19), 1403-1419.
2. Gelb, L. D.; Gubbins, K. E.; Radhakrishnan, R.; Sliwinska-Bartkowiak. *Report on Progress in Physics* **1999,** 62, (12), 1573-1659.
3. Barton, T. J.; Bull, L. M.; Klemperer, W. G.; Loy, D. A.; McEnany, B.; Misono, M.; Monson, P. A.; Pez, G.; Scherer, G. W.; Vartuli, J. C.; Yaghi, O. M. *Chemistry of Materials* **1999,** 11, (10), 2633-2656.
4. Freyman, T. M.; Yannas, I. V.; Gibson, L. J. *Progress in Materials Science* **2001,** 46, (3-4), 273-282.
5. Decher, G.; Hong, J. D.; Schmitt, J. *Thin Solid Films* **1992,** 210-211, (2), 831-835.
6. Decher, G. *Science* **1997,** 277, (5330), 1232-1237.
7. Zhai, L.; Nolte, A. J.; Cohen, R. E.; Rubner, M. F. *Macromolecules* **2004,** 37, (16), 6113-6123.
8. Berg, M. C.; Zhai, L.; Cohen, R. E.; Rubner, M. F. *Biomacromolecules* **2006,** 7, (1), 357-364.
9. Zhai, L.; Cebeci, F. C.; Cohen, R. E.; Rubner, M. F. *Nano Letters* **2004,** 4, (7), 1349-1353.
10. Zhai, L.; Berg, M. C.; Cebeci, F. C.; Kim, Y.; Milwid, J. M.; Rubner, M. F.; Cohen, R. E. *Nano Letters* **2006,** 6, (6), 1213-1217.
11. Hiller, J. A.; Mendelsohn, J. D.; Rubner, M. F. *Nature Materials* **2002,** 1, 59 - 63.
12. Lowman, G. M.; Hammond, P. T. *Small* **2005,** 1, (11), 1070-1073.
13. Takenaka, S.; Maehara, Y.; Imai, H.; Yoshikawa, M.; Shiratori, S. *Thin Solid Films* **2003,** 438-439, 346-351.
14. Mendelsohn, J. D.; Barret, C. J.; Chan, A. J. P.; Mayes, A. M.; Rubner, M. F. *Langmuir* **2000,** 16, (11), 5017-5023.
15. Tokuhisa, H.; Hammond, P. T. *Advanced Functional Materials* **2003,** 13, (11), 831-839.
16. Lowman, G. M.; Tokuhisa, H.; Lutkenhaus, J. L.; Hammond, P. T. *Langmuir* **2004,** 20, (22), 9791-9795.
17. DeLongchamp, D. M.; Hammond, P. T. *Chemistry of Materials* **2003,** 15, (5), 1165-1173.
18. Zhang, S. S. *Journal of Power Sources* **2007,** 164, (1), 351-364.
19. Stair, J. L.; Harris, J. J.; Bruening, M. L. *Chemistry of Materials* **2001,** 13, (8), 2641-2648.
20. Zacharia, N. S.; DeLongchamp, D. M.; Modestino, M.; Hammond, P. T. *Macromolecules* **2007,** 40, (5), 1598-1603.
21. Yoo, P. J.; Nam, K. T.; Qi, J.; Lee, S.-K.; Park, J.; Belcher, A. M.; Hammond, P. T. *Nature Materials* **2006,** 5, 234-240.
22. Bellamy, L. J., *The Infra-red Spectra of Complex Molecules*. Chapman and Hall: London, 1975; p 183-200.
23. Lee, J. Y.; Painter, P. C.; Coleman, M. M. *Macromolecules* **1988,** 21, (2), 346-364.
24. Lu, X.; Weiss, R. A. *Macromolecules* **1995,** 28, (9), 3022-3029.

25. Xie, A. F.; Granick, S. *Macromolecules* **2002,** 35, (5), 1805-1813.
26. Choi, J.; Rubner, M. F. *Macromolecules* **2005,** 38, (1), 116-124.
27. Petrov, A. I.; Antipov, A. A.; Sukhorukov, G. B. *Macromolecules* **2003,** 36, (26), 10079-10086.
28. Burke, S. E.; Barrett, C. J. *Langmuir* **2003,** 19, (8), 3297-3303.
29. Clark, S. L. Engineering the Microfabrication of Layer-by-Layer Polyelectrolyte Assembly. PhD, Massachusetts Institute of Technology, Cambridge, MA, 1999.
30. Weyts, K. F.; Goethals, E. J. *Die Makromolekulare Chemie, Rapid Communications* **1989,** 10, (6), 299-302.
31. Feng, X.; Huang, R. Y. M. *Industrial Engineering and Chemistry Research* **1997,** 36, (4), 1048-1066.
32. Herbig, S. M.; Cardinal, J. R.; Korsmeyer, R. W.; Smith, K. L. *Journal of Controlled Release* **1995,** 35, (2-3), 127-136.
33. Bruce, P. G., In *Polymer Electrolyte Reviews*, MacCallum, J. R.; Vincent, C. A., Eds. Elsevier Applied Science Publishers: London, 1987; pp 237-274.
34. Fabregat-Santiago, F.; Garcia-Belmonte, G.; Bisquert, J.; Zaban, A.; Salvador, P. *106* **2002,** 2, (334-339).
35. Benavente, J.; Garcia, J. M.; Riley, R.; Lozano, A. E.; de Abajo, J. *Journal of Membrane Science* **2000,** 175, 43-52.
36. Coster, H. G. L. *Bioelectrochemistry and Bioenergetics* **1996,** 40, (2), 79-98.
37. Song, J. Y.; Wang, Y. Y.; Wan, C. C. *Journal of the Electrochemical Society* **2000,** 147, (9), 3219-3225.
38. Abraham, K. M.; Alamgir, M. *Journal of the Electrochemical Society* **1995,** 142, (3), 683-687.

Chapter 6 : Conclusion

In summary, this thesis investigated how the architecture and composition of various layer-by-layer (LbL) systems affects the way ions move within the film, and how those LbL film morphologies and structures can be manipulated via processing conditions such as pH and ionic strength. Ultra thin LbL coatings and films can be powerful solid polymer electrolyte candidates for electrochemical systems if the structure and materials properties are understood and can be carefully controlled and tuned. Three LbL systems were investigated: hydrogen-bonded polyethylene oxide (PEO) and polyacrylic acid (PAA); polymer-clay nanocomposites of linear polyethylene imine (LPEI), Laponite clay and PEO; and nano- and microporous LPEI and PAA. Here, the means of controlling these properties via materials selection, use of electrostatic and hydrogen bonding interactions, and assembly conditions has been used to gain a fundamental understanding of ion transport, leading toward the optimization of ion transport in such systems.

Hydrogen bonding PEO and PAA were used to create ion conducting films as a strategy to disrupt the crystallinity of neat PEO. Materials characterization was facilitated by the development of a new methodology to isolate substantial mass and area of LbL film. Here, LbL assembly was performed on a low-energy surface such as Teflon®, and films were simply peeled away. Thermal and materials characterization indicated that PEO/PAA LbL films behaved as amorphous, miscible blends with elastomeric qualities at ambient conditions. For the first time, the glass transition temperature (T_g) of an LbL film was measured; the single observed T_g was found to be highly sensitive to assembly pH, where assembly pH ultimately controlled the extent of *intra-* and *inter*molecular hydrogen bonding of PAA. As assembly pH was increased (pH 2 to 3), the T_g decreased (59 to 26 °C) and the PEO content increased (~25 to 46 mol%), respectively. When the film was doped with lithium via the addition of salt to each assembly bath, the T_g (~50 °C) and the extent of hydrogen bonding remained constant. This behavior suggests that the addition of salt screens hydrogen bonding and the effect of assembly pH becomes insignificant. The maximum conductivity of neat (PEO/PAA) LbL films at 0 % humidity was 9 +/- 3 · 10^{-10} S cm^{-1}, occurring at assembly pH 2.75 (T_g = 35 °C); likewise,

maximum conductivity of $(PEO/PAA)_{LiTrif}$ LbL films was 1.6 +/-0.2 · 10^{-8} S cm^{-1}, at pH 3 (T_g ~ 50 °C). Conductivity further increased for both systems when relative humidity was increased to 53 %.

For the design of solid polymer PEO/PAA LbL electrolyte that conducts lithium ions, the following qualities are recommended. (1) The PEO content must be increased because it is the ion-conducting medium; PAA acts as a passive diluent. (2) The hydrogen-bond cross-link density must be small enough to maintain local relaxations key for ionic conductivity, but large enough to produce cohesive, stable films. (3) The number of mobile charge carriers (lithium ions) must be increased. In the dry state, room temperature conductivity still suffers as a consequence of the LbL film's high T_g, which is above 25 °C. However in humid conditions, sufficient water uptake appears to lower the T_g so as to promote ion conduction.

The second research area investigated the anisotropic structure and transport of polymer-clay LbL assemblies. A layered structure may be capable of blocking the crossover of fuel in a fuel cell, but ionic conductivity may suffer as well. LbL films of LPEI/Clay/PEO yielded a brick-and-mortar structure where *in*-plane ionic conductivity (between clay layers) was 100 times faster than *cross*-plane (across clay layers). Dry *in*-plane ionic conductivity was 7.2 · 10^{-8} S cm^{-1} at 401 K, and *cross*-plane conductivity was 6.8 · 10^{-10} S cm^{-1} at 405 K. From the observed activation energy, it appeared that PEO was the main contributor to the conductivity of lithium cations. The hybrid composite contained 66 wt% clay and 34 wt % PEO and LPEI. In humid conditions (53 % humidity), the conductivity was 10^5 times higher than dry conditions (0 % humidity), indicating that these films may still be applicable in humid conditions such as a fuel cell.

For the performance of this polymer-clay LbL system to be improved, the anisotropy must be disrupted and the polymer content must be increased. One route to accomplish this might be to pre-complex the clay with a polymer such as PEO in solution, and then perform LbL assembly with LPEI, but preliminary attempts show inconclusive results. Another route to increase the polymer content is to include more polymer layers during LbL assembly, and adding less clay adsorption steps.

The third research area studied was an approach to create porous supports for a non-aqueous liquid electrolyte. The structure and formation of nano- and microporous LbL

assemblies consisting of LPEI and PAA was investigated. Pore size and porosity was found to be highly dependent on processing parameters such as assembly pH and post-assembly treatment pH. Maximum porosity of 80 % was possible at optimum conditions of assembly pH 5 and treatment pH 2.25. Porous films exhibited multiple structures ranging from asymmetric membranes to isolated crater-like pores. From capillary forces, liquid electrolyte was wicked into the porous films and the ionic conductivity was measured. Two conductivities, or two time constants, were observed (10^{-6} and 10^{-9} S cm^{-1}), and these were attributed to the presence of two phases (liquid and solid, respectively). Of note, the maximum observed conductivity (10^{-6} S cm^{-1}) was 1000 times less than the liquid electrolyte alone (8.2 mS cm^{-1}). Possible reasons for this discrepancy are that the real path length is tortuous, the effective area for transport is diminished, or that the electrolyte does not fully wet the porous matrix.

A few strategies are recommended to improve the performance of porous LbL systems as electrolyte supports. The connectivity of the porous network must be increased, and the tortuosity must be decreased. Also, using alternate electrolytes that are capable of thoroughly wetting the porous matrix might enhance conductivity. Structures observed in this study are also potential candidates for filtration, catalysis and drug delivery applications because of the high surface area and porosity. In particular, this study represents a first observation of asymmetric membrane structure within LbL assemblies.

In conclusion, LbL assemblies are promising candidates for solid polymer electrolytes. Ultra thin (< 10 μm) films and coatings of tunable conductivity and mobility have been demonstrated in this thesis. Ultimately, by controlling T_g, cross-link density, composition and architecture, made-to-order electrolytes of tunable thickness and properties are possible for electrochemical systems.

Appendix 1 : Characterization and Analysis Techniques

The projects described above require a variety of instrumentation and analysis, described in this section. Thermal analysis allows for the determination of the glass transition temperature, melting temperature, composition and decomposition temperature. Mechanical analysis measures modulus and thermal relaxations such as the glass transition temperature. Impedance analysis is used extensively to measure the ionic conductivity of the LbL film. Techniques essential to this thesis are detailed below.

A1.1 Thermal Analysis

Two instruments were used in the investigation of the thermal properties of LbL thin films: differential scanning calorimetry (DSC) and thermal gravimetric analysis (TGA).

Differential Scanning Calorimetry. This technique is capable of measuring endo- and exothermic events as well as second order phase transitions such as the glass transition.[1, 2] A sample-filled pan is heated or cooled to a set temperature at a set rate. The heat required to achieve the set temperature, relative to an empty reference pan, is plotted with time or temperature. Melting, an endothermic process, will require greater amounts of heat to maintain the set temperature, and a peak will result. For a glass transition, the heat capacity of the material changes, and a sigmoidal shape results, where the inflection point is taken as the glass transition temperature.

Thermal Gravimetric Analysis. TGA is simply a heated balance in an inert gas environment. Sample mass is recorded as temperature is ramped. As solvent evaporates or as the sample decomposes, the mass decreases with increasing heat. Each material has a unique decomposition temperature with a unique loss of mass. In a composite of two materials, one may simply sum the signal of the neat components to predict the composite's TGA response, assuming no stabilizing interactions. Comparing the actual response of the sample with the prediction allows for the estimation of composition of a composite. Of note, if decomposition events of materials A and B overlap with one another, significant error is introduced during composition analysis.

A1.2 Mechanical Analysis

Dynamic mechanical analysis and tensile testing were both used to elucidate the modulus and relaxations within an LbL film, and are detailed below.

Dynamic Mechanical Analysis. This technique studies the viscoelastic response of a thin film to an oscillating tensile stress.[1, 2] The in-phase and out-of-phase responses are termed the storage and loss modulus, respectively. The loss:storage ratio is termed "tan δ." Temperature is ramped at a set rate and the viscoelastic response is recorded. Small relaxations and phase transitions appear as peaks in a plot of tan δ vs. temperature.

Tensile Testing. This method is a simple means to measure the modulus and stress-strain response of a material.[1, 2] A thin film is clamped at both ends and pulled at a predetermined strain rate. The force per area or stress required to maintain the strain rate is recorded and plotted as stress vs. strain. At small extensions, a linear response is common, where the slope is Young's modulus.

A1.3 Impedance Spectroscopy

Electrochemical impedance spectroscopy (EIS) is a powerful technique used to understand transport and kinetic processes (ionic conductivity, diffusion constants) within a material. General approaches and model equivalent circuits are described.

Methodology. EIS is based upon the electrical response of a given material to a sinusoidal voltage or current.[3-5] For example, a voltage wave of small amplitude (~ 10 mV) and known frequency is applied, and the response is a current wave of amplitude I_o and phase shifted by θ, Figure A-1. The ratio of these two, $V(\omega)/I(\omega)$, is the impedance, $Z(\omega)$. Frequency is swept and the impedance response is recorded. Knowing the phase angle, the impedance response may be separated into real (Z_{Real}) and imaginary parts (Z_{Img}), and plotted for all frequencies studied. A plot of Z_{Img} vs. Z_{Real} is called a Nyquist (or Cole-Cole) plot, and a plot of θ vs. ω is called a Bode plot. To extract physical information from the data and plots, a model is needed.

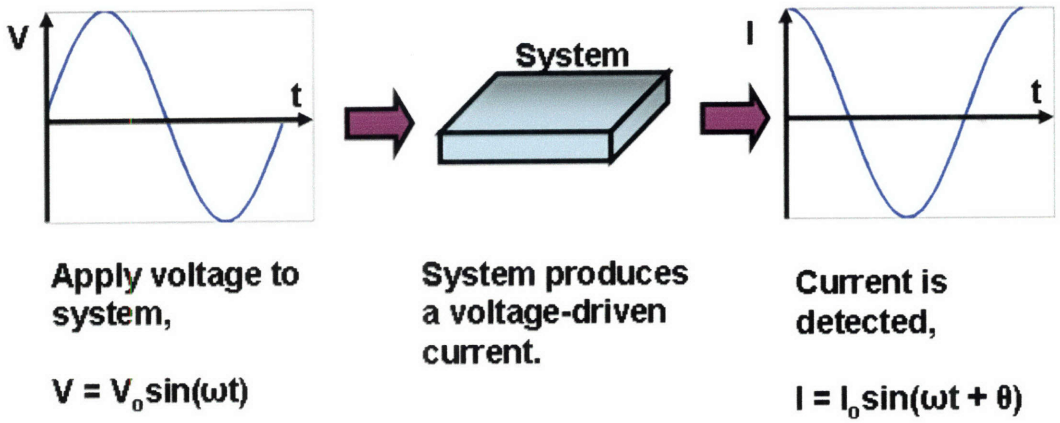

Figure A-1. Impedance spectroscopy explanation. A sinusoidal voltage is applied to a system, and the system produces a current of amplitude I_o that is out of phase by θ. The experiment is performed as frequency is swept.

Equivalent Circuit. As described by Bruce,[6] the impedance response of a polymer electrolyte may be modeled by the equivalent circuit described in Figure A-2. To better visualize the relation between the model circuit and the physical system, imagine the flow of electrons, ions and dipoles. Within the electrodes, electrons will move in response to the applied potential. Resistance losses arising from the transport of electrons with the electrodes is given by R_1. At the electrode-electrolyte interface ions from the electrolyte build up so as to balance the electrons at the electrode. This interface gives rise to a capacitive behavior termed the "double layer", described by C_{DL}. Within the electrolyte, two processes occur, hence the parallel circuit. First, ions may migrate in the presence of an electric field. Resistance to ion transport within the bulk electrolyte is given by R_b. In tandem, the electric field induces dielectric relaxations of the polymer itself. This capacitive behavior, related to the dielectric constant of the polymer electrolyte, is described by C_b. As there are two electrodes and two electrolyte interfaces, there exists a second set of R_1 and C_{DL}.

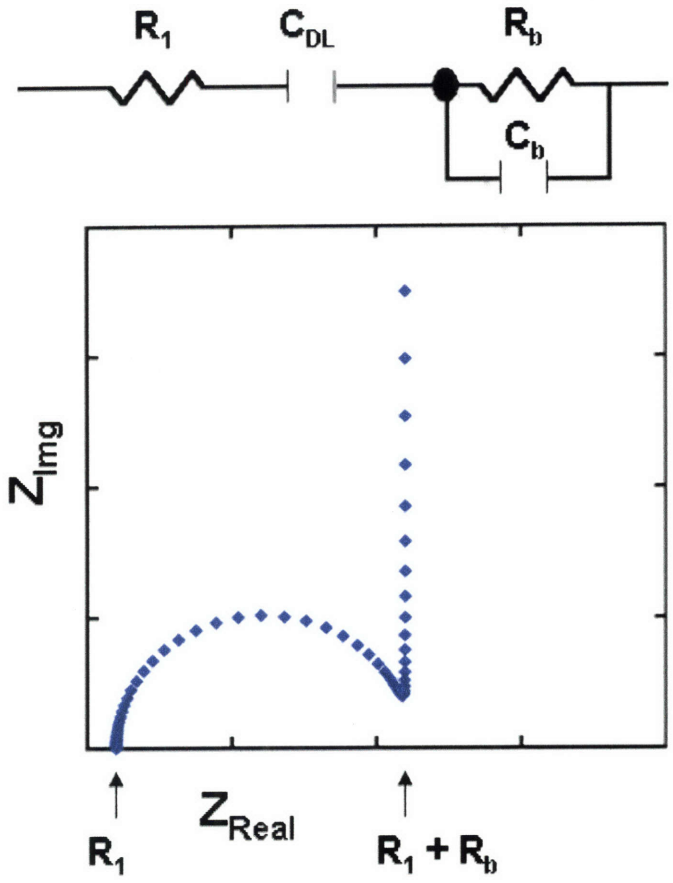

Figure A-2. Model equivalent circuit and Nyquist plot for a polymer electrolyte at blocking electrodes. R_1 is the resistance of the electrodes, C_{DL} is the double-layer capacitance, R_b is the resistance of the electrolyte and C_b is the capacitance of the electrolyte. For measuring ionic conductivity, the parameter of interest is R_b, which is the diameter of the semi-circle.

This model equivalent circuit yields a distinctive Nyquist plot, Figure A-2, where a high-frequency semicircle with a low-frequency vertical spike is present. The location of the semicircle will shift to the right as R_1 increases, and the diameter of the semicircle will increase as R_b increases. The peak of the semicircle, occurring at frequency ω, is given by $1 = (\omega RC)^{-1}$. At low frequencies, the real impedance approaches R_1+R_b, and the imaginary impedance increases because of C_{DL}. The conductivity of the electrolyte is

given by $\sigma = L/R_bA$, where L is the thickness between electrodes and A is the electrode area.

Mathematically, resistance and capacitance may be represented as real and imaginary responses. The impedance and capacitance of a resistor and capacitor is given by:

$$Z_R = R \qquad \text{Equation 1}$$

$$Z_C = -j/\omega C \qquad \text{Equation 2}$$

respectively. When two elements are in series, the total impedance is given by:

$$Z_{series} = \sum Z_i \qquad \text{Equation 3}$$

For a resistor and capacitor in series, the total capacitance becomes:

$$Z_{series} = R - j/\omega C \qquad \text{Equation 4}$$

where j is sqrt(-1). When two elements are in parallel, the total impedance becomes:

$$\frac{1}{Z_{Parallel}} = \sum \frac{1}{Z_i} \qquad \text{Equation 5}$$

Applying this rationale to the equivalent circuit in Figure A-2, the mathematical impedance response of a polymer electrolyte is derived. Using Equation 5, the total impedance of the circuit is:

$$Z = Z_{R1} + Z_{CDL} + Z_{ParallelRbCb} \qquad \text{Equation 6}$$

where the impedance of the parallel R_bC_b circuit is given by:

$$\frac{1}{Z_{ParallelRbCb}} = \frac{1}{Z_{Rb}} + \frac{1}{Z_{Cb}} \qquad \text{Equation 7}$$

Substituting in impedances expressions for resistance and capacitances gives:

$$\frac{1}{Z_{ParallelRbCb}} = \frac{1}{R_b} + j\omega C_b \qquad \text{Equation 8}$$

This reduces to:

$$Z_{ParallelRbCb} = R_b\left[\frac{1}{1+(\omega C_b R_b)^2}\right] - jR_b\left[\frac{\omega R_b C_b}{1+(\omega C_b R_b)^2}\right] \qquad \text{Equation 9}$$

Combining Equations 1, 2, 6 and 9 gives an expression for the total impedance response of the equivalent circuit:

$$Z = \left\{R_1 + R_b\left[\frac{1}{1+(\omega C_b R_b)^2}\right]\right\} - j\left\{R_b\left[\frac{\omega R_b C_b}{1+(\omega C_b R_b)^2}\right] + \frac{1}{\omega C_{DL}}\right\} \qquad \text{Equation 10}$$

$$Z_{real} = R_1 + R_b\left[\frac{1}{1+(\omega C_b R_b)^2}\right] \qquad \text{Equation 11}$$

$$Z_{img} = R_b\left[\frac{\omega R_b C_b}{1+(\omega C_b R_b)^2}\right] + \frac{1}{\omega C_{DL}} \qquad \text{Equation 12}$$

The left hand term in Equation 10 is the real impedance, and the right hand term is the imaginary impedance. Plotting $-Z_{img}$ vs. Z_{real} gives a Nyquist plot, as described before. At high frequencies, lim $\omega \rightarrow \infty$, $-Z_{img} \rightarrow 0$ and $Z_{real} \rightarrow R_1$. At d.c.-like conditions, lim $\omega \rightarrow 0$, $-Z_{img} \rightarrow \infty$ and $Z_{real} \rightarrow R_1+R_b$.

In real systems, departure from ideal conditions is commonly observed. Oftentimes, a depressed semi-circle or a tilted vertical spike is viewed in real Nyquist plots. These non-idealities may be captured using a constant phase element (CPE) instead of a capacitor, where $1/Z_{cpe}=Q(j\omega)^n$, where n is a constant ranging from 0 to 1 and $Q = C$ when $n = 1$. Potential sources of non-ideal behavior may originate from a rough electrode-electrolyte interface and a distribution of dielectric constant (inhomogeneous materials).

A1.4 References

1. Young, R. J.; Lovell, P., *Introduction to polymers*. Chapman and Hall: New York, 1991.
2. Painter, P. C.; Coleman, M. M., *Fundamentals of Polymer Science: An Introductory Text*. CRC: New York, 1998.
3. Bard, A.; Faulkner, L., *Electrochemical Methods: Fundamentals and Applications*. Second ed.; John Wiley and Sons, Inc.: Hoboken, 2001.
4. Bruce, P. G., *Solid State Electrochemistry*. Cambridge Univeristy Press: New York, 1995.
5. Newman, J.; Thomas-Alyea, K. E., *Electrochemical systems*. Wiley: Hoboken, 2004.
6. MacCallum, J. R.; Vincent, C. A., *Polymer Electrolyte Reviews*. Elsevier Applied Science: New York, 1987; Vol. 1.